University of Alberta

FLUID INTRUSIONS AND INTERNAL GRAVITY WAVE GENERATION IN STRATIFIED MEDIA

by

Morris R. Flynn

A thesis submitted to the Faculty of Graduate Studies and Research
in partial fulfillment of the requirements for the degree of
Master of Science

in

Applied Mathematics

Department of Mathematical and Statistical Sciences
Edmonton, Alberta
Fall, 2003

National Library
of Canada

Acquisitions and
Bibliographic Services

395 Wellington Street
Ottawa ON K1A 0N4
Canada

Bibliothèque nationale
du Canada

Acquisisitons et
services bibliographiques

395, rue Wellington
Ottawa ON K1A 0N4
Canada

Your file Votre référence
ISBN: 0-612-87761-2
Our file Notre référence
ISBN: 0-612-87761-2

The author has granted a non-exclusive licence allowing the National Library of Canada to reproduce, loan, distribute or sell copies of this thesis in microform, paper or electronic formats.

The author retains ownership of the copyright in this thesis. Neither the thesis nor substantial extracts from it may be printed or otherwise reproduced without the author's permission.

L'auteur a accordé une licence non exclusive permettant à la Bibliothèque nationale du Canada de reproduire, prêter, distribuer ou vendre des copies de cette thèse sous la forme de microfiche/film, de reproduction sur papier ou sur format électronique.

L'auteur conserve la propriété du droit d'auteur qui protège cette thèse. Ni la thèse ni des extraits substantiels de celle-ci ne doivent être imprimés ou aturement reproduits sans son autorisation.

Canada

University of Alberta

Library Release Form

Name of Author: Morris R. Flynn

Title of Thesis: Fluid Intrusions and Internal Gravity Wave Generation in Stratified Media

Degree: Master of Science

Year This Degree Granted: 2003

Permission is hereby granted to the University of Alberta Library to reproduce single copies of this thesis and to lend or sell such copies for private, scholarly, or scientific research purposes only.

The author reserves all other publication and other rights in association with the copyright in the thesis, and except as herein before provided, neither the thesis nor any substantial portion thereof may be printed or otherwise reproduced in any material form whatever without the author's prior written permission.

Date: 03/07/30

UNIVERSITY OF ALBERTA

Faculty of Graduate Studies and Research

The undersigned certify that they have read, and recommend to the Faculty of Graduate Studies and Research for acceptance, a thesis entitled **Fluid Intrusions and Internal Gravity Wave Generation in Stratified Media** submitted by **Morris Robert Flynn** in partial fulfillment of the requirements for the degree of Master of Science in Applied Mathematics.

July 17, 2003

Abstract

The excitation of internal gravity waves by fluid intrusions that propagate along the interface between a uniform upper layer and a uniformly stratified lower layer is examined by way of laboratory experiments. Over the domain of interest, the fluid intrusions traveled at a constant speed. For a limited range of density parameters, good agreement was obtained between the experimental data and the two-layer analytical theory of Holyer & Huppert [36] which provides estimates for the intrusion speed and depths of penetration into the upper and lower layers.

Internal gravity wave excitation is due to the initial collapse of the lock fluid and the forcing imparted by the head of the intrusion. Waves are visualized and their amplitudes measured using "synthetic schlieren." Wave amplitudes are small in the sense that they extract only a small portion of the intrusion's total kinetic energy.

Rudimentary geophysical applications of these results are discussed.

[Life] looks just a little more mathematical and regular than it is; its exactitude is obvious, but its inexactitude is hidden; its wildness lies in wait.

- G.K. Chesterton

Laboring always at the same oar, with some wave ever ahead threatening to overwhelm us and yet passing harmless under our bark, we knew not how we rode through the storm with heart and hand, and made a happy port.

- Thomas Jefferson

Dedicated to the memory of
FRANCIS J. PINGOR

Acknowledgements

First and foremost, I would like to acknowledge the exceptional contribution of my supervisor, Dr. Bruce R. Sutherland whose insights are reflected throughout the present study. Bruce's encouragement and assistance have been invaluable in my developement as a scientist and I owe him an enormous debt of gratitude for his efforts on my behalf. Furthermore, I would like to thank my parents, Peter and Alida, Heather MacNeil and Rowan Scott whose patience and support were always greatly appreciated even on those days when I forgot to say so. Finally, I would like to acknowledge the kind assistance of my graduate student colleagues in the Fluids Group: Paul Choboter, Matt Reszka and Kathleen Dohan.

Graduate financial support for this study was generously provided by the following organizations: NSERC, Alberta's iCORE Program, the Faculties of Science and Graduate Studies and Research, the Department of Mathematical and Statistical Sciences and the Institute for Geophysical Research.

Table of Contents

List of Figures vii

List of Tables viii

1 Introduction and Motivation 1

1.1 Internal Gravity Wave Excitation in the Atmosphere 1

1.2 Internal Gravity Wave Excitation in the Ocean 5

1.3 Laboratory Experiments 6

1.4 Thesis Overview 10

2 Theory 12

2.1 Bottom-Propagating Gravity Currents 12

2.2 Fluid Intrusions 14

2.3 Holyer and Huppert's Equations Under the Boussinesq Approximation 18

2.4 Asymptotic Approximation to Holyer and Huppert's Equations 20

3 Experimental Set-Up 26

3.1 Experimental Procedure 26

3.2 Synthetic Schlieren - Determination of Δz 31

3.3 Synthetic Schlieren - Determination of ΔN^2 and N_i^2 34

3.4 Signal Strength 37

4 Qualitative Observations and Results 38

4.1 Fluid Intrusions 38

4.2 Internal Gravity Waves 42

5 Quantitative Results **50**

5.1 Fluid Intrusions 50

5.2 Internal Gravity Waves - Excitation 55

5.3 Internal Gravity Waves - Stability 64

5.4 Internal Gravity Waves - Momentum Flux 66

6 Application of the Experimental Results to Geophysical Flows **68**

6.1 Fluid Intrusions in the Atmosphere 68

6.2 Fluid Intrusions in the Ocean 70

7 Discussion and Conclusions **74**

A Benjamin's Analysis of Gravity Currents **77**

A.1 Deep Gravity Currents 77

A.2 Shallow Gravity Currents 80

B Asymptotic Approximation **83**

C Experimental Parameters **85**

D Fluid Intrusions in a Uniformly Stratified Ambient **88**

E Dispersion Relation for Internal Gravity Waves **91**

E.1 Problem Formulation 91

E.2 Wave Solution 92

E.3 Group and Phase Velocities 94

F Wave Momentum Flux of Storm-Induced Oceanic Internal Gravity Waves **95**

F.1 Application of Holyer & Huppert's Analysis 95

F.2 Justification of the Momentum Flux Calculation 99

Bibliography **101**

List of Tables

5.1 Characteristic angle of wave propagation in six studies involving the dynamic generation of internal gravity waves. 60

7.1 Wave momentum fluxes associated with internal gravity wave generation from fluid intrusions in the atmosphere and ocean. 76

C.1 Experimental parameters (weak stratification). 86

C.2 Experimental parameters (strong stratification). 87

List of Figures

1.1 The ascent and lateral spreading of an anvil cloud. 4

1.2 Comparison between the mechanism of internal gravity wave excitation in the studies of (a) Wu [99], Amen & Maxworthy [3] and Maxworthy *et al.* [57] and (b) the present study. 9

2.1 The propagation of a fluid intrusion of density ρ_i between uniform layers of densities ρ_+ (above) and ρ_- (below). 16

2.2 (a) h_+, h_- and h_i (normalized by H_+) versus ζ for $H_+/H_- = 1/2$. (b) h_+ and h_i (normalized by H_+) versus ζ for $H_+/H_- = 1$. In the intervals over which HH80 predicts non-unique solutions, the physically anticipated solution is denoted by the thick solid line. First order asymptotic approximations about $\zeta = -1/2$ are indicated by the long dashed lines. 22

2.3 Normalized intrusion velocity as a function of ζ. Line labels are explained in the text. 25

3.1 (a) Front view of the tank. For the purposes of our subsequent analysis, we place the origin of an (x, z) coordinate system at the point denoted by O. A schematic representation of the density profile is also shown. (b) Side view of the tank showing the relative positions of the grid of black and white lines, the tank and the CCD camera. (Figures not to scale.) 27

3.2 Measured density profiles corresponding to the experiment for which $N^2 = 1.15\,\mathrm{s}^{-2}$ and $\sigma_* = 0.0102$. The heavy solid line indicates the initial profile, whereas the thin solid line shows the profile following the release of the third intrusion. The intrusion height, h_i, for this particular run is indicated by the vertical line. 30

3.3 Snapshot images (a) prior to oscillation and (b) immediately following two oscillations. Subtracting (a) from (b) yields the qualitative synthetic schlieren image depicted in (c). The corresponding Δz field is shown in (d). 33

4.1 Image of the intrusion head for the experiment in which $N^2 = 0.67\,\mathrm{s}^{-2}$, $\sigma_* = 0.0038$ and $\sigma_i = 0.0006$. The top of the $\sim 1\,\mathrm{cm}$ thick interfacial layer corresponds to the line $z = 0\,\mathrm{cm}$. The distances h_+, h_- and l_i are as indicated. 40

4.2 Composite time series along the vertical slice $x/L_l = 0.99$ corresponding to the experiment for which $N^2 = 1.17\,\mathrm{s}^{-2}$, $\sigma_* = 0.0037$ and $\sigma_i = 0.0020$. The equivalent horizontal scale is indicated by the top axis. 43

4.3 (a) Vertical time series of the N_t^2 field (see also Figure 4.2). (b) The average power spectrum. (c) The ω profile corresponding to (b). The dashed-and-dotted line denotes the unsmoothed profile whereas the solid line denotes the smoothed profile. In both (b) and (c), the N value ($N = 1.08\,\mathrm{s}^{-1}$) for this particular experimental run is indicated by the vertical dashed line. . . . 44

4.4 (a) Time series of the N_t^2 field along the horizontal slice $z/h_- = -2.0$ for the experimental run described in Figures 4.2 and 4.3. (b) The power spectrum corresponding to (a). (c) The k_x profiles as derived from (b). Line types are as indicated in Figure 4.3c. 45

4.5 Variation in $A_{N_i^2}$ with x for three different experimental runs. Data point types are as follows - open squares: $N^2 = 0.69\,\mathrm{s}^{-2}$, $\sigma_* = 0.0024$, $\sigma_i = 0.0019$; stars: $N^2 = 0.92\,\mathrm{s}^{-2}$, $\sigma_* = 0.0027$, $\sigma_i = 0.0018$; solid triangles: $N^2 = 1.15\,\mathrm{s}^{-2}$, $\sigma_* = 0.0102$, $\sigma_i = 0.0020$. The dotted line indicates the distance one lock-length from the gate, which is situated at $x = 0\,\mathrm{cm}$. The error bar denotes the typical measurement uncertainty. 49

5.1 Normalized depth of penetration into the (a) upper and (b) lower layers. Data point types are as follows - closed hexagons: $N^2 = 0.37\,\mathrm{s}^{-2}$; open squares: $N^2 \simeq 0.67\,\mathrm{s}^{-2}$; stars: $N^2 = 0.92\,\mathrm{s}^{-2}$; closed triangles: $N^2 \simeq 1.17\,\mathrm{s}^{-2}$. The solid and dotted lines indicate the solutions predicted by HH80 and their first order asymptotic approximations, respectively. The error bars denote the typical measurement uncertainty. 53

5.2 (a) Normalized intrusion velocity as a function of ζ_*. Data point and line types are as indicated in Figure 5.1. The error bar denotes the typical measurement uncertainty. (b) Log-log plot of the normalized intrusion velocity as a function of $\zeta_* + 1/2$ plotted for those experiments with $\zeta_* \leq 0.25$. The slope of the (vertically offset) best-fit line is indicated. 54

5.3 (a) Normalized amplitude of the vertical displacement field as a function of ζ_*. Data point types are as follows - open squares: $N^2 \simeq 0.67\,\mathrm{s}^{-2}$; stars: $N^2 = 0.92\,\mathrm{s}^{-2}$; closed trinagles: $N^2 \simeq 1.17\,\mathrm{s}^{-2}$. The error bar denotes the typical uncertainty in the measurement of A_ξ/λ_x. (b) Log-log plot of the normalized amplitude as a function of $\zeta_* + 1/2$ plotted for those experiments with $\zeta_* \leq 0.25$. The slope of the (vertically offset) best-fit line is indicated. 56

5.4 (a) Normalized horizontal wavenumber of the internal gravity waves versus the normalized inverse horizontal extent of the intrusion head. (b) Internal gravity wave frequency as a function of the frequency of the forcing imparted by the head of the intrusion. In both cases, data point types are as indicated in Figure 5.3; the error bars denote the typical measurement uncertainty. 57

5.5 A_ξ/λ_x versus Θ. Data point types are as indicated in Figure 5.3. The error bar denotes the typical uncertainty in the measurement of A_ξ/λ_x. 59

5.6 Normalized frequency of the internal gravity waves, ω, as a function of the normalized undulation frequency, ω_u. Data point types are as indicated in Figure 5.3. The error bars denote the typical measurement uncertainty. 63

5.7 Internal gravity wave stability diagram. The curves labeled "SA" and "OT" denote the critical amplitudes at which self-accelerating and overturning instabilities are anticipated, respectively. 65

6.1 Log-log plot of the normalized momentum flux as a function of the normalized intrusion velocity for $-1/2 \leq \zeta_* \leq 0.25$. The slope of the (vertically offset) best-fit line is indicated. 73

A.1 The propation of a deep, energy-conserving gravity current through a uniform ambient of depth H. The $x-z$ coordinate system is as indicated. 79

A.2 The propagation of a dissipative gravity current through a uniform ambient of infinite depth. The $x-z$ coordinate system is as indicated. 82

D.1 The propagation of a symmetric fluid intrusion in stratified surroundings. The density profile is indicated by the thick solid line. 90

F.1 (a) Temperature and (b) N^2 profiles of the eastern north Pacific Ocean prior to the mixing induced by Hurriance Norbert. (Adapted from Figure 10(c) of Price, Sanford & Forristall [70].) The long dashed line indicates the intrusion's level of neutral buoyancy. 97

Chapter 1

Introduction and Motivation

1.1 Internal Gravity Wave Excitation in the Atmosphere

Gravity currents (also known as density currents or buoyancy currents) and internal gravity waves are ubiquitous phenomena in the atmosphere and ocean. The former arise when fluid of one density propagates horizontally into fluid of another density. Atmospheric manifestations of this phenomenon include thunderstorm outflows and sea breeze fronts (Turner [95], Simpson [81], [82]). Most experimental and theoretical studies of gravity currents have examined the propagation of dense fluid along a rigid boundary beneath a uniform ambient (Keulegan [41], Benjamin [6], Simpson [79], [80], Britter & Simpson [9], Simpson & Britter [83], Huppert & Simpson [40], D'Alessio *et al.* [13], Hallworth *et al.* [34], Härtel *et al.* [35], Shin, Dalziel & Linden [78]). A gravity current that propagates along an interface within a stratified fluid we refer to as a fluid intrusion. These have been studied theoretically and experimentally by Holyer & Huppert [36], Britter & Simpson [10], D'Alessio *et al.* [14], de Rooij [20], de Rooij, Linden & Dalziel [21], Sutherland [88] and Mehta, Sutherland & Kyba [59].

Internal gravity waves, which propagate within density stratified environments play an important role in atmospheric circulation. For example, it is

well known that breaking internal gravity waves impart a significant drag on the zonal winds (Lindzen [52], Kida [42], Gavrilov & Roble [30] and Becker & Schmitz [5]). Although the largest proportion of momentum transport by internal gravity waves is associated with those generated by topographic forcing (Fritts & Nastrom [29]), other dynamic excitation mechanisms can also result in significant momentum fluxes.

In particular, convective forcing may represent the most important source of atmospheric internal gravity waves in the Southern Hemisphere and the tropics (Alexander, Holton & Durran [1]). Beres, Alexander & Holton [7] have identified three means by which convective motion may excite waves (see also Mason & Sykes [56], Clark, Hauf & Kuettner [11] and Fovell, Durran & Holton [28]). "Quasi-stationary forcing" describes the generation of internal gravity waves by perturbations to the mean flow caused by the pressure field of a rising convective element. Because the element thereby acts as a "fluidic" (*i.e.* non-rigid) obstacle, this mechanism is also known as the "obstacle effect." In the absence of a background mean flow, waves may be generated through the oscillatory deflection to the boundary of a stratified layer due to the successive rising and falling of convective eddies. This scenario is similar to the experiments of Plumb & McEwan [68] in which boundary deflections were established using mechanical means. The mechanism is therefore referred to as the "mechanical oscillator effect" (McIntyre [58]). The third means for wave excitation through deep convection is the "deep heating effect" which describes the generation of internal gravity waves due to the thermal forcing associated with latent heat release within a convective storm. Internal gravity wave generation is thus due to fluid expansion; the wave's vertical wavelength is approximately twice that of the vertical extent through which heating occurs (Salby & Garcia [74]).

Whereas Clark, Hauf & Kuettner [11] determined that a strong wind shear was required for the generation of strong internal gravity waves, Fovell, Durran & Holton [28] found that this was not the case when considering the deep convection associated with mesoscale convective storms, even though their

analysis did not explicitly consider the "deep heating effect."

In addition to topographic and convective forcing, atmospheric internal gravity waves may also be generated by the vortices produced in an unstable parallel shear flow, a mechanism referred to as "shear generation" (Lindzen [51], Sutherland, Caulfield & Peltier [89], Sutherland [86] and Sutherland & Linden [94]). Qualitatively, internal gravity waves are anticipated when the stratification of the strongly-sheared region is low compared to that of the surrounding strongly stratified ambient as characterised by Richardson numbers less than and greater than 1/4, respectively.[1]

Here, we initiate an idealised experimental study examining a novel variation of the convective and shear mechanisms for wave generation in which stratospheric internal gravity waves are excited by the propagation of a storm-generated fluid intrusion along the tropopause, the boundary separating the weakly stratified troposphere (below) from the strongly stratified stratosphere (above). Examples of such flows include the tops of tall anvil clouds, high-level rope clouds that form by detaching from the leading edge of anvil clouds (Simpson [82]; see Figure 1.1) and laterally spreading volcanic clouds (Rose *et al.* [72]).

[1] In the present context, the Richardson number is defined by $\mathrm{Ri} = N^2/(dU/dz)^2$ where $N^2 = -(g/\rho_{00})d\bar{\rho}/dz$ is the square of the buoyancy frequency (see Chapter 3) and dU/dz is the vertical velocity gradient. Broadly speaking, Ri is a measure of the stabilizing effects of density stratification to the destabilizing effects of velocity shear. (See Miles [62] for details.)

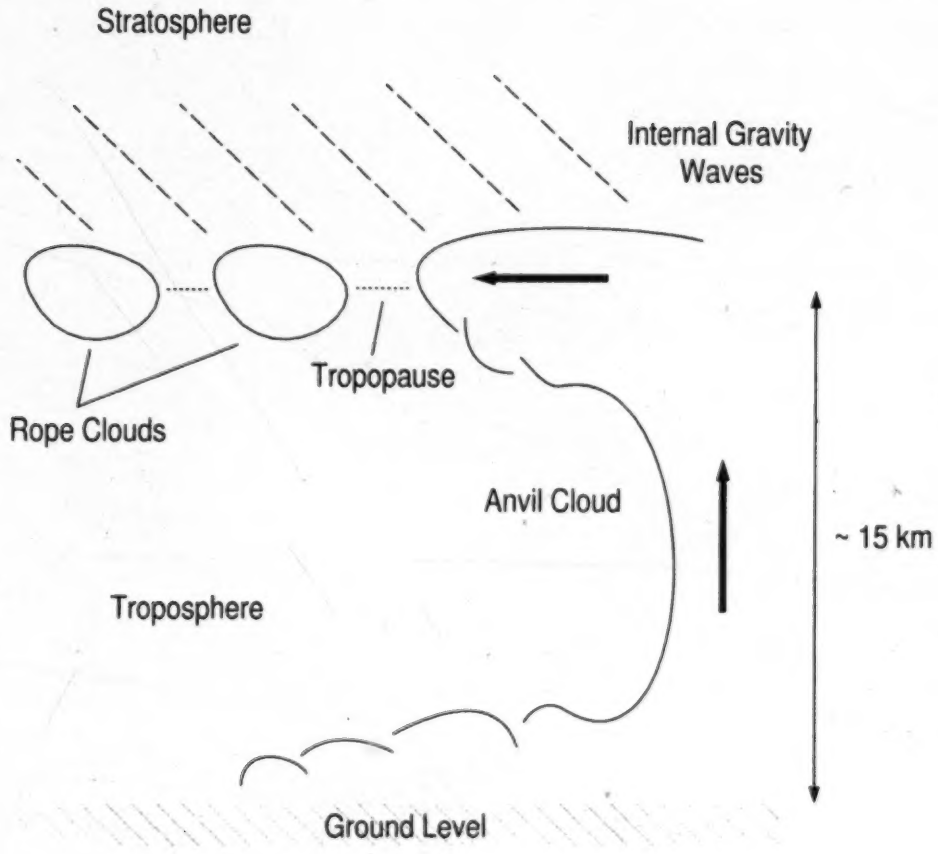

Figure 1.1: The ascent and lateral spreading of an anvil cloud.

1.2 Internal Gravity Wave Excitation in the Ocean

An analogous and dynamically equivalent mechanism for internal gravity wave generation may exist in an oceanographic context. Before describing this mechanism in detail, however, let us first consider some preliminaries. Just as in the atmosphere, internal gravity waves play a non-trivial role in the general circulation of the world's oceans. In particular, it has been suggested by Ledwell *et al.* [46] (see also Polzin *et al.* [69] and Marshall [55]) that the turbulent mixing induced by internal gravity wave breaking is responsible for reducing the density of deep ocean waters. As a result, this fluid rises to the surface in roughly equal proportion to the volume of water that is vertically advected into the deep ocean through deep water formation at high latitudes.

Whereas, the study of Fritts & Nastrom [29] identified topographic forcing as the most important source of atmospheric internal gravity waves, flow over rough terrain is also important in the context of wave generation in the ocean. This was recently demonstrated by an observational team from the Woods Hole Oceanographic Institute (see *e.g.* Ledwell *et al.* [46] and the references therein) who injected sulfur hexafluoride approximately 500 m above the mid-Atlantic ridge and tracked the evolution of this dye streak over a period of approximately 14 months. The observed spreading of sulfur hexafluoride was attributed primarily to the enhanced mixing due to internal gravity wave breaking. Wave excitation resulted from barotropic tidal flow over the rough bathymetry that constitutes the mid-Atlantic ridge. Characteristic mixing diffusivities for the water mass directly above this ridge were estimated as being two orders of magnitude larger than the value of $0.1\,\mathrm{cm}^2/\mathrm{s}$ reported in areas devoid of topography (Marshall [55]).[2]

Near-surface oceanic internal gravity waves may be excited by the forcing imparted by the surface mixed layer. As described in Skyllingstad & Denbo [84] wave generation is typically due to either a local Kelvin-Helmholtz insta-

[2]By contrast, the molecular kinematic viscosity for water has a value $\nu \simeq 0.01\,\mathrm{cm}^2/\mathrm{s}$.

bility or to the "obstacle effect" wherein deflections to the base of the mixed layer are due to transient convective plumes.

Although the ocean provides numerous other mechanisms for wave generation, let us return to the flow scenario depicted in Figure 1.1 by which internal gravity waves are excited by the forcing imparted by a fluid intrusion. Such flows could potentially develop during strong tropical or mid-latitude storms wherein storm-induced vertical mixing and air-sea exchanges result in a relatively rapid cooling of surface waters (Cornillon, Stramma & Price [12]). If the storm is sufficiently fierce, significant mixing with the stratified fluid below the level of the thermocline may also occur yielding a local deepening of the surface mixed layer. Within the broader ocean, this homogeneous parcel of fluid may go baroclinically unstable and form a fluid intrusion that propagates just below the thermocline.

Unfortunately, observational studies examining the response of the ocean to strong storms is limited. To the extent that this response has been characterized at all, most oceanographers have focused on the large-scale inertial flows that evolve over long time scales such that Coriolis forces become important (see *e.g.* Price, Sanford & Forristall [70], D'Asaro [17], [18], D'Asaro, Eriksen & Levine [19], Large & Crawford [45], Levine & Zervakis [47], Niiler & Paduan [64], Qi *et al.* [71] and Zervakis & Levine [100]). To our knowledge, no direct observations of storm-induced, horizontally propagating oceanic fluid intrusions exist in the literature. As such, our analysis of these events and their ability to excite internal gravity waves in the stratified fluid below the thermocline (limited as it is to a single geophysical event described in Price, Sanford & Forristall [70]) is speculative in nature.

1.3 Laboratory Experiments

Previous investigations into the generation of internal gravity waves in a uniformly stratified fluid by density driven currents fall under two principal categories: those in which wave excitation is due to a bottom-propagating gravity

current (Maxworthy *et al.* [57] and Ungarish & Huppert [96]) and those in which the current propagates at some intermediate depth (Schooley [75], Wu [99], Schooley & Hughes [76], Manins [54] Amen & Maxworthy [3], Britter & Simpson [10], Faust & Plate [25], de Rooij [20]). In the experiments of Maxworthy *et al.* [57], the gravity current was released using a standard lock-release apparatus. Direct excitation of internal gravity waves occurred when the current's velocity was below that of the linear, mode-one long wave in the wave guide, a condition referred to by Maxworthy *et al.* [57] as "subcritical" (see also Long [53]). At this point, "first-mode waves were formed which interacted with the head of the advancing gravity current to destroy the original front and to cause a succession of gravity-current heads" (Simpson [81]). In other words, a rhythmic coupling was established that alternately accelerated and decelerated the gravity current head. By contrast, no such behaviour has been observed in studies involving the propagation of a gravity current through a non-stratified ambient for which the speed of propagation is constant during the slumping phase of motion.

Experiments that consider the gravitational collapse of a homogeneous mixed region within a stratified fluid typically ignore boundary effects. Wu [99] divided the horizontal propagation of the mixed region into three distinct stages: the "initial" stage, during which the rate of collapse is constant, the "principal" stage during which the collapse rate begins to decrease and the "final" stage in which the mixed region becomes wedge-shaped and propagates so slowly that viscous effects become significant. Internal gravity waves are generated both above and below the collapsing mixed layer.

Whereas Wu [99] did not observe a resonant interaction between the intrusion and the internal gravity waves, such behaviour was noted in the related study of Amen & Maxworthy [3], for whom the initial height of the mixed region relative to the depth of the stratified ambient was notably larger. As in the experiments of Maxworthy *et al.* [57], this interaction resulted in the irregular advance of the intrusion head.

For both classes of experiment described above, internal gravity wave gen-

eration is due to two factors: direct excitation by the gravity current and indirect excitation associated with the return flow of stratified fluid that flows into the lock once the gate is released so as to replenish the fluid that comprises the collapsing gravity current (see Figure 1.2a).

Experiments performed in the present study are different from those described above in two fundamental respects. They consider the behaviour of a fluid intrusion in a two-layer system in which the lower layer is uniformly stratified and the top layer is uniform in density. As in the investigations of Wu [99], Amen & Maxworthy [3] and Maxworthy *et al.* [57], flow is established using a simple lock-release apparatus. In the present case, however, the lock fluid initially spans only the height of the uniform layer and the collapse of this fluid therefore occurs strictly within non-stratified surroundings. Consequently, this collapse does not induce a return flow in the (lower) stratified layer. As indicated in Figure 1.2b, internal gravity wave generation is due solely to the direct mechanism: forcing by the fluid intrusion.

Whereas the vertical density profile of the atmosphere and oceans is more complicated than that considered in the present study, the experiments bear strong similarity to the interfacial flow phenomenon depicted in Figure 1.1 and provide an important starting point for assessing the importance of either thunderstorm outflows or storm-induced fluid intrusions within the ocean as sources of internal gravity waves. Although the experiments capture only Boussinesq dynamics, by which density differences are neglected except for their impact on buoyancy forces[3], they are nonetheless relevant from an atmospheric perspective. In particular, for the flow depicted in Figure 1.1, the vertical extent over which wave forcing occurs ($\lesssim 100\,\mathrm{m}$) is small relative to the local scale height, H_s. Explicitly, using equation (3.5.13) of Gill [31], we find that $H_s = RT/g \simeq 6.4\,\mathrm{km}$ where $R = 287.04\,\mathrm{J/kg/K}$ is the gas constant for air, $g = 9.8\,/\mathrm{s}^2$ is the acceleration due to gravity and $T \simeq 220\,\mathrm{K}$ is the approximate temperature at the tropopause (see Figure 3.3 of Gill [31]).

[3]Generally speaking, this simplification is appropriate when density variations are at least an order of magnitude smaller than the characteristic density.

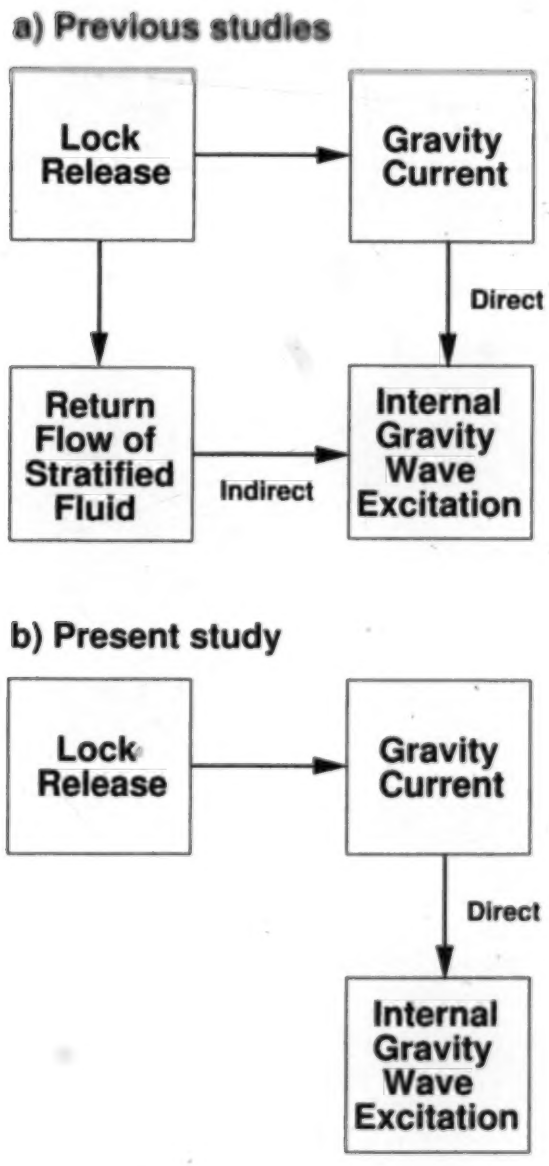

Figure 1.2: Comparison between the mechanism of internal gravity wave excitation in the studies of (a) Wu [99], Amen & Maxworthy [3] and Maxworthy *et al.* [57] and (b) the present study.

1.4 Thesis Overview

The thesis is organized as follows:[4] Chapter 2 provides an overview of the analytic theory of Holyer & Huppert [36] (hereafter HH80) which describes the propagation of a fluid intrusion between two uniform layers. Under the Boussinesq approximation, an asymptotic approximation to their original equations is derived about a particular point in density space. In addition, the theory of de Rooij, Linden & Dalziel [21], which considers the behaviour of a fluid intrusion in a two-layer system under more restrictive conditions is discussed. The experimental set-up is summarized in Chapter 3. Qualitative observations of the experiments are described in Chapter 4. In addition, methods for determining the intrusion's speed of propagation and depth of penetration into the upper and lower layers as well as the amplitude, frequency and horizontal wavenumber of the internal gravity waves are considered. Quantitative comparisons between the observed properties of the fluid intrusions and those predicted by HH80 are made in Chapter 5. The behaviour of the internal gravity waves is also analyzed. In Chapter 6, we consider the applicability of the present investigation to geophysical flows. Finally, a series of conclusions is provided in Chapter 7.

Many of the detailed calculations are presented in the appendices. Explicitly, Appendix A provides a derivation of Benjamin's [6] results for energy-conserving and dissipative gravity currents propagating in uniform surroundings. HH80 employ aspects of this theory when considering the more complicated two-layer case. Appendix B shows a detailed derivation of the asymptotic approximation to HH80's equations. The raw experimental data is presented in Appendix C. Appendix D considers the behaviour of a fluid intrusion in uniformly stratified surroundings. A derivation of the dispersion relation for propagating internal gravity waves is presented in Appendix E. Finally, Appendix F provides details of the wave momentum flux calculations as applied

[4] Aspects of this material have been submitted for publication; see Flynn & Sutherland [27] and Sutherland, Flynn & Dohan [91].

to oceanic internal gravity wave forcing by storm-induced fluid intrusions.

Chapter 2

Theory

2.1 Bottom-Propagating Gravity Currents

The behaviour of an inviscid gravity current propagating in a uniform ambient of depth H was considered theoretically by Benjamin [6]. He showed that for energy-conserving flows in which surface tension and viscosity can be neglected, the dominant force balance is between horizontal momentum and hydrostatic effects. As demonstrated in Appendix A, the corresponding relations for the current depth, h, and horizontal speed of propagation, v_{gc} are, respectively,

$$h = \frac{H}{2}, \tag{2.1}$$

and

$$v_{gc} = \frac{1}{\sqrt{2}}\sqrt{g'h}. \tag{2.2}$$

In the above equations, $g' = g(\rho_{gc} - \rho_+)/\rho_{00}$ in which g is the acceleration due to gravity, ρ_{gc} is the gravity current density, ρ_+ is the density of the ambient fluid and ρ_{00} is a characteristic reference density.

Although Benjamin's [6] theory for energy-conserving gravity currents shows relatively strong agreement with the early experimental studies of Keulegan [41] and Barr [4], it is not without limitations. For one, it considers only steady state flows and is therefore only applicable during the slumping phase

of motion.[1] In a finite volume scenario, however, the gravity current's motion must eventually become self-similar at which point the balance of forces is between buoyancy and inertia and the position of the front advances as $t^{2/3}$ (*i.e.* $v_{gc} \sim t^{-1/3}$) (Huppert [39]). As the gravity current continues to spread, its thickness may become small enough that viscous effects become important and the current may therefore be further decelerated. Huppert [38] demonstrated that $v_{gc} \sim t^{-4/5}$ in this regime. In a standard, full depth lock-release experiment, the assumption of steady motion ceases to be valid once the forward-propagating rear bore catches up to the gravity current head. Typically, this occurs after the gravity current has traveled a distance of approximately 10 lock-lengths (Rottman & Simpson [73], Simpson [82]).

More fundamentally, Benjamin's [6] theory strictly applies only when the density difference between the ambient fluid and the gravity current is small *i.e.* the fluids are Boussinesq. In situations where this approximation is invalid, v_{gc} becomes dependent on non-parallel motions within the gravity current. The experiments of Gröbelbauer, Fanneløp & Britter [32] confirm that equations (2.1) and (2.2) do not provide accurate predictions of observed behaviour in the non-Boussinesq case (see also Hacker [33]).

Furthermore, when $h < H/2$, Benjamin [6] suggests that the gravity current must dissipate energy (see Appendix A). However, his analysis precludes the possibility that energy and momentum can be transfered between the current head and the backward-propagating disturbance that is generated by releasing the lock. Shin, Dalziel & Linden [78] show that this represents a "significant omission" when $h_{t=0}$, the initial height of the gravity current (immediately following the release of the lock, say) is less than $0.76H$.

In view of the constraints imposed by Benjamin's [6] theory, concurrent attempts at describing the behaviour of a bottom-propagating gravity current

[1] Although Klemp, Rotunno & Skamarock [43] note that "the propagation of gravity currents may be constrained by factors that cannot be determined solely from steady-state analyses", a detailed consideration of their arguments is beyond the scope of the present study.

using shallow water (hydraulic) theory have been made, beginning with the study of Hoult [37]. Subsequently, a series of "hybrid" models were developed by Rottman & Simpson [73] and Klemp, Rotunno & Skamarock [43] in which the shallow water equations were applied using Benjamin's [6] result as a frontal boundary condition. Unfortunately, this approach was not entirely successful in explaining observed behaviour. For example, in describing the study of Rottman & Simpson [73], Moodie [63] noted that when $h_{t=0} > H/2$ "there is little resemblance between their numerical simulations and the experimentally observed transition of the flow to the self-similar phase." Furthermore, the model derived by Klemp, Rotunno & Skamarock [43] yields estimates for v_{gc} that are in excess of measured propagation speeds.

More recent applications of shallow water theory have enjoyed greater success. For example, Shin, Dalziel & Linden [78] employed a modified front condition based on their extension of Benjamin's [6] analysis and found good agreement between measured and predicted propagation speeds (see Figure 11 of their study and Figure 3.11 of Shin [77]). Moreover, D'Alessio *et al.* [13] developed a shallow water model that accurately captures the transition to the self-similar phase. For details, see §1 of Moodie [63].

2.2 Fluid Intrusions

By comparison with bottom-propagating gravity currents, the theory describing fluid intrusions is not as well developed. Although shallow water theory has been applied with some success in this regard (see *e.g.* D'Alessio *et al.* [14]), here, we shall focus our attention on the extension of Benjamin's [6] theory derived by HH80.

Figure 2.1 shows the propagation of a fluid intrusion of density ρ_i and total height h_i between two layers of uniform density. The upper layer has density ρ_+ and depth H_+ whereas the lower layer has density ρ_- and depth H_-. The thickness of the interface separating these layers is assumed negligibly small. As with the analysis of Benjamin [6], HH80 assume that the intrusion's

speed of propagation, v_i, is a constant. Therefore, we proceed by considering a frame of reference in which the intrusion is stationary with respect to a moving ambient. Upstream of the stagnation point O (at point A, say), the ambient travels at a speed v_i whereas downstream of the stagnation point (points B and C, say), the velocity of the ambient in the upper and lower layers is v_+ and v_-, respectively. Consistent with Benjamin [6], HH80 take the pressure at the stagnation point to be zero, *i.e.* $p_O = 0$.

Line segments OA, OB and OC represent streamlines of the flow. Therefore, by imposing the boundary conditions of no normal velocity along OA, OB and OC and by requiring pressure continuity across these streamlines, it can be shown that $\delta = 120^o$ where δ denotes the angle between line segments OB and OC at the stagnation point O (see Figure 2.1).

Because the intrusion is energy-conserving, its motion must satisfy Bernoulli's equation. Applying this relation between points O and A just above and below the interface yields, respectively,

$$p_A + \frac{1}{2}\rho_+ v_i^2 = \rho_+ g(L - H_-), \tag{2.3}$$

and

$$p_A + \frac{1}{2}\rho_- v_i^2 = \rho_- g(L - H_-). \tag{2.4}$$

In the above equations, L is the height of the tip of the fluid intrusion, which for now we assume is different from H_-. Furthermore, p_A is the upstream pressure along the interface.

By assumption, $\rho_- > \rho_+$. Equations (2.3) and (2.4) therefore imply that $p_A = 0$ from which it follows that

$$L - H_- = \frac{1}{2} \cdot \frac{v_i^2}{g} > 0. \tag{2.5}$$

Conservation of energy therefore requires that the intrusion tip be raised relative to the interface by $1/2 \cdot v_i^2/g$. In most experiments involving fluid intrusions (including those considered in the present study), $v_i^2/g \sim \mathcal{O}(0.001)\,\mathrm{cm}$ to $\mathcal{O}(0.01)\,\mathrm{cm}$ *i.e.* the amount by which the intrusion tip is raised above the interface is too small to be detected with the naked eye.

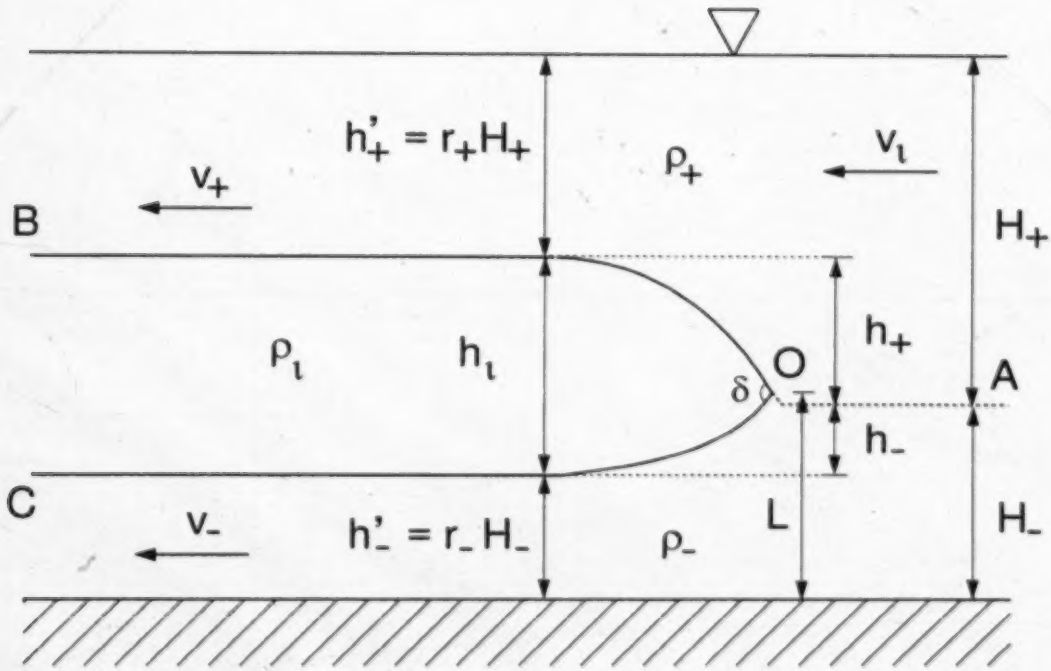

Figure 2.1: The propagation of a fluid intrusion of density ρ_i between uniform layers of densities ρ_+ (above) and ρ_- (below).

We now proceed to derive the equations for the intrusion's speed of propagation and depth of penetration into the upper (h_+) and lower (h_-) layers. Applying the principle of mass conservation above and below the fluid intrusion yields, repectively,

$$v_i H_+ = v_+ h'_+, \tag{2.6}$$

and

$$v_i H_- = v_- h'_-, \tag{2.7}$$

where $h'_+ = H_+ - h_+$ and $h'_- = H_- - h_-$ represent the distances from the top and bottom of the intrusion to the free and solid boundaries, respectively (see Figure 2.1). Furthermore, by applying Bernoulli's equation along a path immediately above the segment OB, it can be shown that

$$v_+^2 \left(1 + \frac{\alpha_+ (h'_+)^2}{H_+^2}\right) = 2\alpha_+ g h_+. \tag{2.8}$$

In the above equation,

$$\alpha_+ = \frac{\rho_i - \rho_+}{\rho_+}.$$

Similarly, conservation of energy between points O and C requires that

$$v_-^2 \left(1 - \frac{\alpha_- (h'_-)^2}{H_-^2}\right) = 2\alpha_- g h_-, \tag{2.9}$$

where

$$\alpha_- = \frac{\rho_- - \rho_i}{\rho_-}.$$

Combining these results with equations (2.6) and (2.7), the following mathematical expression for mass conservation can be derived

$$\frac{\alpha_+ h_+ (h'_+)^2}{H_+^2 + \alpha_+ (h'_+)^2} = \frac{\alpha_- h_- (h'_-)^2}{H_-^2 - \alpha_- (h'_-)^2}. \tag{2.10}$$

Equations (2.6) through (2.9) represent four equations in five unknowns: h'_+, h'_-, v_i, v_+ and v_-. To close the system, we require that momentum be conserved over the region depicted in Figure 2.1. Hence,

$$\begin{aligned} -\frac{\rho_- v_-^2 h'_- h_-}{H_-} - \frac{\rho_+ v_+^2 h'_+ h_+}{H_+} = \\ -\frac{1}{2}\rho_i g (H_- + H_+)(H_- + H_+ - 2L) + \frac{1}{2}\rho_- g (h'_-)^2 - \frac{1}{2}\rho_+ g (h'_+)^2 \\ -\frac{1}{2}\rho_- g H_-^2 + \frac{1}{2}\rho_+ g H_+^2 - \frac{1}{2}\rho_i g (h'_-)^2 + \frac{1}{2}\rho_i g (h'_+)^2. \end{aligned} \tag{2.11}$$

As before, equations (2.8) and (2.9) can be used to simplify the above expression. Some algebra shows that

$$2\alpha_- \frac{1+\alpha_+}{1-\alpha_-} h'_- h_- \frac{2-h'_- - \alpha_- h'_-}{1-\alpha_-(h'_-)^2} H_- + \frac{2\alpha_+ h'_+ h_+ (2H_+ - h'_+ + \alpha_+ h'_+)}{H_+^2 + \alpha_+ (h'_+)^2} H_+ = \alpha_- \frac{1+\alpha_+}{1-\alpha_-}[H_- - (h'_-)^2] + \alpha_+ [H_+^2 - (h'_+)^2]. \quad (2.12)$$

Equations (2.10) and (2.12) represent a coupled system of cubic polynomial equations for h'_+ and h'_- in terms of the upper and lower layer depths, H_+ and H_-, respectively, and the densities of the upper (ρ_+) and lower (ρ_-) layers relative to that of the intrusion (ρ_i). For fixed values of H_+ and H_-, they predict non-unique solutions for h'_+ and h'_- for a limited range of density parameters. In this range, it is argued that the physically anticipated solution is that for which the intrusion's volume inflow (or total height, $h_i = h_+ + h_-$) is a maximum. Although this assumption has been criticized by Faust & Plate [25], consideration of their arguments is beyond the scope of the present study.

Finally, estimates for the intrusion's speed of propagation, v_i, can be derived by solving equations (2.10) and (2.12) then applying equation (2.6) or (2.7).

2.3 Holyer and Huppert's Equations Under the Boussinesq Approximation

Although it is relatively straight-forward to solve equations (2.10) and (2.12) numerically (*e.g.* using Maple), analysis of these equations is facilitated by applying the Boussinesq approximation whereby density differences are neglected except in the buoyancy term. As demonstrated by Sutherland, Kyba & Flynn [93], the corresponding expressions for mass and momentum conservation are, respectively,

$$\left(\zeta + \frac{1}{2}\right) H_+ r_+^2 (1 - r_+) = \left(\frac{1}{2} - \zeta\right) H_- r_-^2 (1 - r_-), \quad (2.13)$$

and,

$$\left(\zeta+\frac{1}{2}\right)H_+^2(1-r_+)^2(1-2r_+)+\left(\frac{1}{2}-\zeta\right)H_-^2(1-r_-)^2(1-2r_-)=0, \quad (2.14)$$

where $r_+ = h'_+/H_+$, $r_- = h'_-/H_-$ and

$$\zeta = \frac{\rho_i - \bar{\rho}}{\rho_- - \rho_+}. \quad (2.15)$$

In the above equation, $\bar{\rho} = (\rho_- + \rho_+)/2$. The parameter ζ was first introduced by de Rooij, Linden & Dalziel [21] and has the property that $\zeta = -1/2$ when $\rho_i = \rho_+$ and $\zeta = 1/2$ when $\rho_i = \rho_-$. In a separate set of analyses of intrusions in two-layer fluids, Sutherland, Kyba & Flynn [93] introduced the depth-weighted parameter, ϵ, by

$$\epsilon = \frac{\rho_i - \bar{\rho}'}{\rho_- - \rho_+},$$

where

$$\bar{\rho}' = \frac{H_-\rho_- + H_+\rho_+}{H},$$

in which $H = H_- + H_+$. The parameters ζ and ϵ are related as follows

$$\epsilon + \frac{H_-}{H} = \zeta + \frac{1}{2}.$$

Thus ζ and ϵ are equivalent when $H_- = H_+ = H/2$. Here, we represent our results in terms of ζ instead of ϵ because the former does not depend explicitly upon the lower layer depth, which may not be a significant quantity if the lower layer is stratified.

The intrusion speed, v_i, is determined from v_+, the relative velocity of the return flow along the intrusion's upper flank. Explicitly:

$$v_i = r_+ v_+, \quad (2.16)$$

where

$$v_+ = \sqrt{2\left(\zeta+\frac{1}{2}\right)\sigma' g H_+(1-r_+)}. \quad (2.17)$$

In the above equation, $\sigma' = (\rho_- - \rho_+)/\rho_{00}$. Equivalently,

$$v_i = r_- v_-, \quad (2.18)$$

where

$$v_- = \sqrt{2\left(\frac{1}{2} - \zeta\right)\sigma' g H_-(1 - r_-)}, \tag{2.19}$$

in which v_- represents the relative velocity of the return flow along the lower flank of the intrusion.

2.4 Asymptotic Approximation to Holyer and Huppert's Equations

An asymptotic approximation to equations (2.13) and (2.14) about the point $\epsilon = 0$ has been derived by Sutherland, Kyba & Flynn [93]. Many of the experiments described in Chapter 3 are performed in the limit $\zeta \to -(1/2)^+$, however. Physically, this corresponds to an intrusion that penetrates negligibly into the lower layer. We therefore set $\Gamma = \zeta + 1/2$, $r_+ = 1/2 + Y$ and $r_- = 1 - X$ in which Y and X represent small correction factors. Substituting these expressions into equations (2.13) and (2.14), it can be shown that

$$\Gamma H_+(1 + 2Y)^2(1 - 2Y) = 8H_- X(1 - \Gamma)(1 - X)^2, \tag{2.20}$$

and,

$$Y(H_+)^2\Gamma(1 - 2Y)^2 = 2X^2(H_-)^2(1 - \Gamma)(2X - 1). \tag{2.21}$$

First-order asymptotic approximations about $\zeta = -1/2$ are obtained by expressing X and Y as first-order perturbation expansions in Γ:

$$X = \Gamma X_1 + \mathcal{O}(\Gamma^2),$$

and,

$$Y = \Gamma Y_1 + \mathcal{O}(\Gamma^2).$$

Combining the above expressions for X and Y with equations (2.20) and (2.21), and solving for X_1 and Y_1 by matching like powers of Γ, it can be shown that

$$\frac{h_+}{H_+} = \frac{1}{2} + \frac{1}{32}\Gamma + \mathcal{O}(\Gamma^2), \tag{2.22}$$

and,

$$\frac{h_-}{H_+} = \frac{1}{8}\Gamma + \mathcal{O}(\Gamma^2). \tag{2.23}$$

(Details of the above calculation are presented in Appendix B.) To first-order therefore, h_+/H_+ and h_-/H_+ are independent of H_+/H_-.

Figures 2.2a and b present comparisons between the exact results of HH80 (*i.e.* equations (2.10) and (2.12)) and the first-order asymptotic approximations given by equations (2.22) and (2.23). The former shows $h_+/H+$, h_-/H_+ and h_i/H_+ as functions of ζ for $H_+/H_- = 1/2$. HH80 yields non-unique solutions when $0.114 \leq \zeta \leq 0.241$; within this range, the physically anticipated solution is denoted by the thick solid line. First-order asymptotic approximations to h_+ and h_- about $\zeta = -1/2$ are indicated by the long dashed lines. For $-1/2 \leq \zeta \lesssim -0.30$, they show agreement within 0.2% and 21.9% of the full solutions of HH80 for h_+ and h_-, respectively.

The symmetric case of equal upper and lower layer depths ($H_+/H_- = 1$) is considered in Figure 2.2b. HH80 predict bifurcation points at $\zeta = \pm 0.069$. Due to symmetry, the curve corresponding to h_-/H_+ (not shown) is simply the reflection of h_+/H_+ about the line $\zeta = 0$. As with Figure 2.2a, Figure 2.2b indicates that the first-order asymptotic approximation provides a strong estimate of the behaviour predicted by the coupled equations of HH80 for $-1/2 \leq \zeta \lesssim -0.30$.

An asymptotic expansion for v_i about $\zeta = -1/2$ is obtained by combining equations (2.16), (2.17) and (2.22). Setting $\sigma = (\rho_- - \rho_+)/\rho_+$, we find (see Appendix B)

$$\frac{v_i}{\sqrt{\sigma g h_i}} = f\sqrt{\frac{\Gamma}{2}}, \tag{2.24}$$

where

$$f = \left(1 - \frac{3}{16}\Gamma + \mathcal{O}(\Gamma^2)\right). \tag{2.25}$$

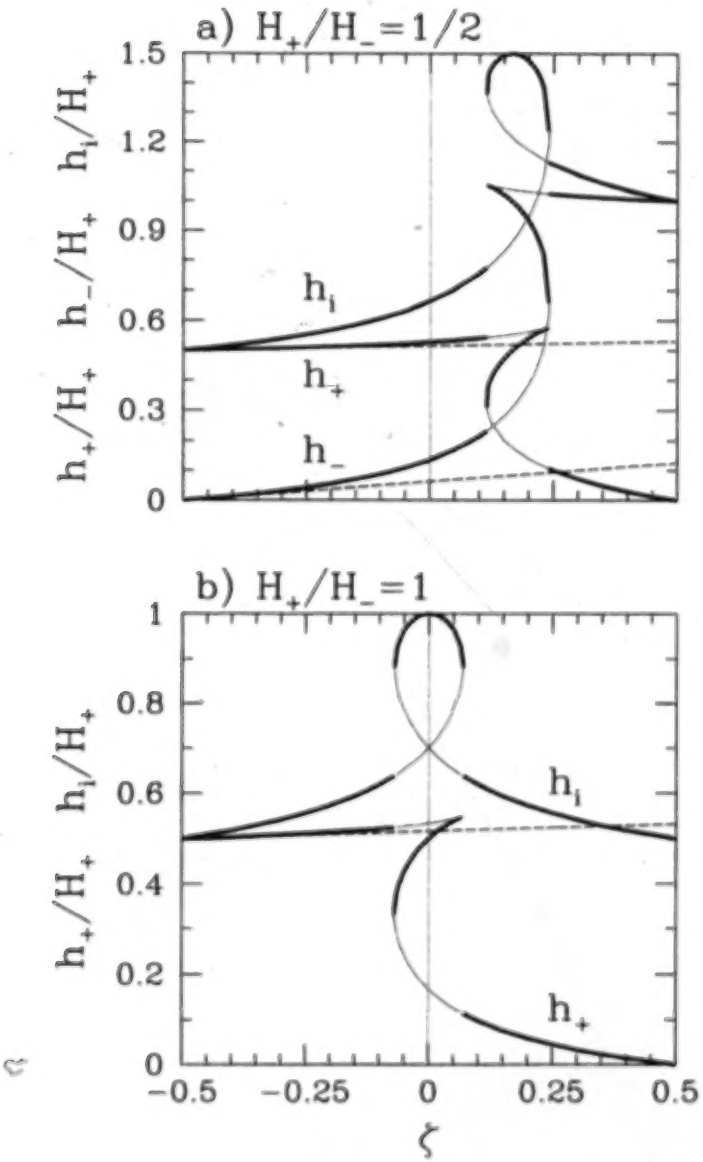

Figure 2.2: (a) h_+, h_- and h_i (normalized by H_+) versus ζ for $H_+/H_- = 1/2$. (b) h_+ and h_i (normalized by H_+) versus ζ for $H_+/H_- = 1$. In the intervals over which HH80 predicts non-unique solutions, the physically anticipated solution is denoted by the thick solid line. First order asymptotic approximations about $\zeta = -1/2$ are indicated by the long dashed lines.

When $\zeta \simeq -1/2$, $\Gamma \simeq 0$ and the driving force for fluid motion is due almost exclusively to the density difference between the intrusion and the top layer, $\rho_i - \rho_+$. In this case, $1 \gg 3/16 \cdot \Gamma$, and hence $f \simeq 1$. Therefore, consistent with equation (2.2),

$$\frac{v_i}{\sqrt{\sigma g h_i}} \simeq \sqrt{\frac{\Gamma}{2}}.$$

For $\zeta > -1/2$ ($\Gamma > 0$), the contribution of the lower layer to the dynamics of the flow becomes significant. The asymptotic approximation to HH80 about $\zeta = -1/2$ is equivalent to Benjamin's [6] result for a two-layer, non-dissipative system with additional higher order correction terms.

Figure 2.3 compares the results of equations (2.24) and (2.25) with the full solution of HH80's equations for $H_+/H_- = 1$ (bifurcation points at $\zeta = \pm 0.069$) and $H_+ \ll H_-$ (bifurcation points at $\zeta \to 1/2$). The first-order asymptotic approximation for v_i yields a prediction accurate to within 0.5% of the exact result for $-1/2 \leq \zeta \lesssim -0.30$ when $H_+/H_- \leq 1$.

Two additional curves are presented in Figure 2.3. That labeled 'B68' corresponds to Benjamin's [6] energy-conserving solution as given by equation (2.2). Consistent with the above analysis, Benjamin's [6] result shows good agreement with HH80 in a small neighborhood of $\zeta = -(1/2)^+$, but diverges from this solution more rapidly than the asymptotic approximation given by equations (2.24) and (2.25).

Also shown in Figure 2.3 is a curve due to the analytic theory of de Rooij, Linden & Dalziel [21]; it is denoted by 'dRLD99' Their model represents a simplification of HH80 in that they assume both layers are infinite in extent and hence effectively equal in depth. Their solution, which is applicable to both energy-conserving and dissipative currents, expresses v_i as an explicit function of ζ

$$\frac{v_i}{\sqrt{\sigma g h_i}} = \frac{\mathrm{Fr}}{2}\sqrt{\frac{\rho_+}{\rho_i}}\sqrt{1-4\zeta^2} \simeq \frac{\mathrm{Fr}}{2}\sqrt{1-4\zeta^2}. \qquad (2.26)$$

where the Froude number, Fr, is defined such that

$$\mathrm{Fr} \leq \mathrm{Fr}_{max} = \frac{2v_i|_{\zeta=0}}{\sqrt{\sigma \frac{\rho_+}{\rho_i} g h_i}}.$$

In the present case, Fr has been made explicit by requiring that the predicted solution approach that given by Benjamin [6] (and HH80) in the limit $\zeta \to -1/2$. Specifically, we set $\mathrm{Fr} = 1/\sqrt{2}$. As indicated by Figure 2.3, the solution of de Rooij, Linden & Dalziel [21] shows strong agreement with the theory of HH80 only for $1/2 \geq |\zeta| \gtrsim 0.4$.

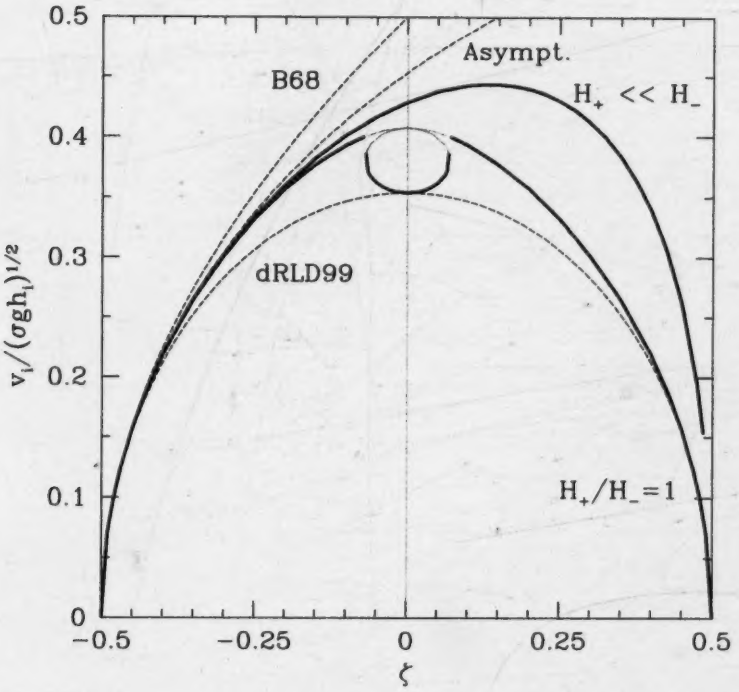

Figure 2.3: Normalized intrusion velocity as a function of ζ. Line labels are explained in the text.

Chapter 3

Experimental Set-Up

3.1 Experimental Procedure

Experiments were performed in a glass tank measuring $L_t = 197.1\,\text{cm}$ long by 48.5 cm tall by 19.9 cm wide (inside width, $L_g = 17.6\,\text{cm}$). A 30.0 cm tall, 19.6 cm long platform that spanned the width of the tank was installed at one end (see Figure 3.1). The non-uniform density profile was established using a two-step process. First, a 30.0 cm deep layer of uniformly salt stratified fluid was added to the tank using the "double bucket" technique (Oster [66]). Thus the top of the stratified fluid was at the level of the top of the platform. A 15.0 cm deep layer of fresh or slightly saline water was then layered on top of the stratified fluid by trickling it through a sponge float. A traversing conductivity probe (Fast Conductivity and Temperature Probe - Precision Measurement Engineering) was used to measure the resulting density profile. As a result of mixing, the interface between the uniform and stratified fluids was approximately 1 cm thick. Because the thickness of the fluid intrusion was typically five to 10 times larger than this value, the properties of the intrusion were not significantly influenced by the thickness of the interface.

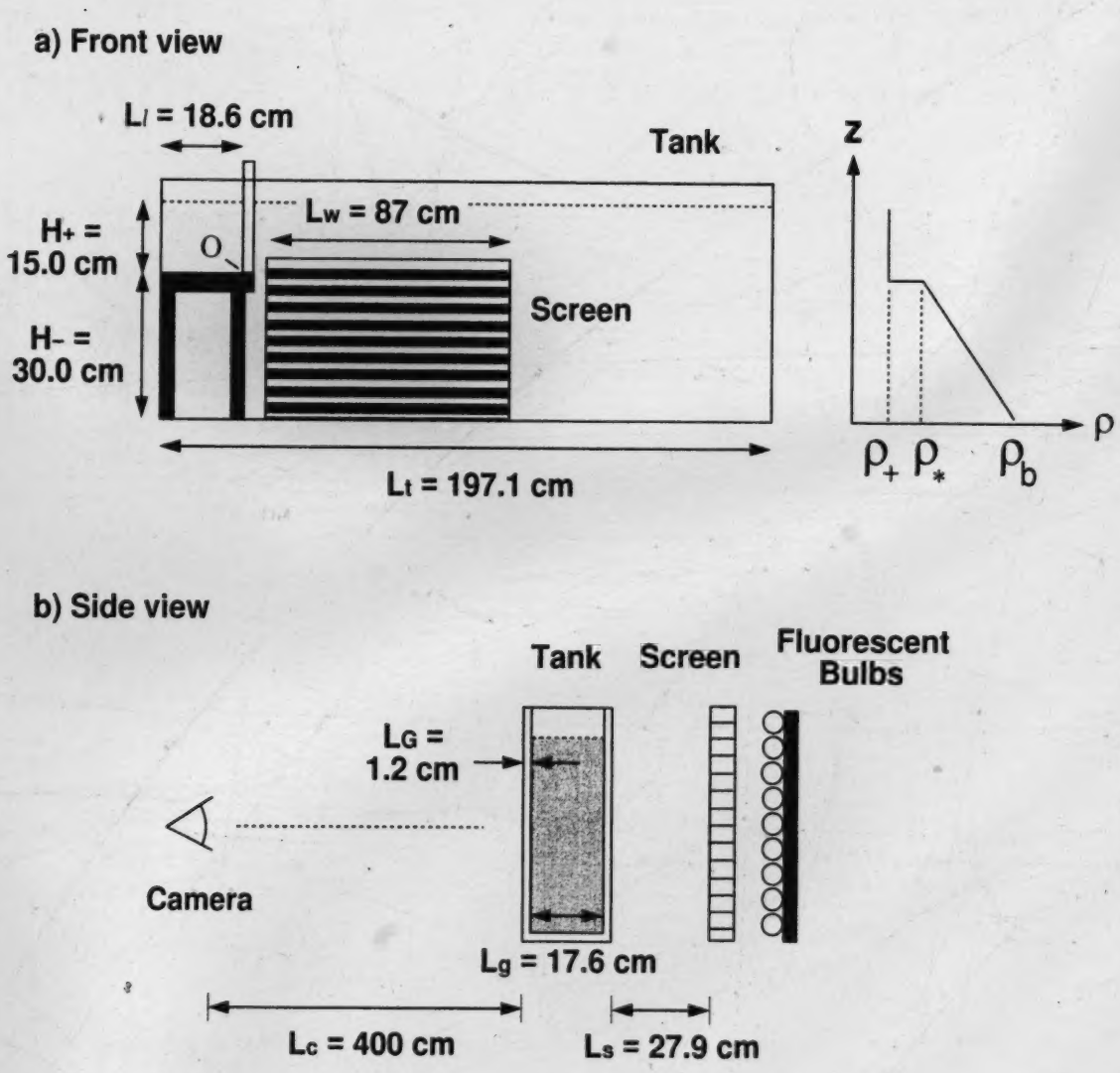

Figure 3.1: (a) Front view of the tank. For the purposes of our subsequent analysis, we place the origin of an (x, z) coordinate system at the point denoted by O. A schematic representation of the density profile is also shown. (b) Side view of the tank showing the relative positions of the grid of black and white lines, the tank and the CCD camera. (Figures not to scale.)

After filling the tank, a 0.4 cm thick gate was inserted between a pair of vertical glass guides to the level of the platform. NaCl and a small amount of food colouring were then added to the lock fluid after which it was made homogeneous by vigorous mixing for a period of approximately 15 s. The resulting fluid had a density ρ_i.

In total, 39 experimental runs were performed in which the following three parameters were varied: the strength of stratification of the lower layer, as measured in the Boussinesq approximation by the square of the buoyancy frequency, $N^2 = -(g/\rho_{00})d\bar{\rho}/dz$, where g is the acceleration due to gravity, ρ_{00}, a characteristic value of density[1], and $\bar{\rho}(z)$, the background density as a function of height; the magnitude of the density jump across the interface as measured by $\sigma_* = (\rho_* - \rho_+)/\rho_{00}$, where ρ_* is the density of the top-most isopycnal surface of the stratified layer and ρ_+ is the density of the (uniform) top layer; and the relative density of the intrusion as defined by $\sigma_i = (\rho_i - \rho_+)/\rho_{00}$ where ρ_i is the density of the lock fluid. Experiments were performed with N^2 ranging from $0.37\,\mathrm{s}^{-2}$ to $1.21\,\mathrm{s}^{-2}$ ($\pm 0.04\,\mathrm{s}^{-2}$), σ_* ranging from 0.0015 to 0.0102 (± 0.0001) and σ_i ranging from 0.0005 to 0.0023 (± 0.0001). In this preliminary study, our interest is in the response of the stratified layer to disturbances caused by intrusions for which h_- is relatively small. Hence, in the majority of experiments, the stratification is relatively strong ($N^2 > 0.65\,\mathrm{s}^{-2}$) and $\rho_i < (\rho_* + \rho_+)/2$.

Runs began by rapidly removing the gate from the tank. The lock fluid then collapsed to form an intrusion that propagated along (or in three extreme cases immediately below) the interfacial layer. The purpose of the platform was two-fold. It inhibited the vertical motion of the fluid intrusion during the initial collapse stage and thereby reduced the magnitude of the transient impulse delivered to the stratified layer. Furthermore, because the lock fluid extended only to the depth of the platform, and hence to the depth of the interface between the uniform and stratified fluid, no mean flow was induced as a result of stratified ambient fluid replenishing the collapsed lock fluid; only

[1]Typically, ρ_{00} is taken to be the density of fresh water.

the unstratified ambient above the interface developed such a return flow (see Figures 1.2 and 3.1). The height of the platform was determined so as to maximize the horizontal distance over which wave reflection off the bottom of the tank was negligible while concurrently satisfying $H_+ \simeq H_-$. The lock length, $L_l = 18.6\,\mathrm{cm}$, was not changed over the course of the study because this variable has been shown to have little impact on the properties of the fluid intrusion (Sutherland, Kyba & Flynn [93]).

The motions of the fluid intrusion and internal gravity waves were recorded to video tape using a CCD camera located $L_c = 400\,\mathrm{cm}$ in front of the tank. The zoom on the camera was set such that the field of view spanned a horizontal distance $L_w = 87\,\mathrm{cm}$ with the gate at the left extremity of the field of view. The camera was connected to a computer running DigImage (Dalziel [15]), a robust image processing program that, in particular, converts digital "snapshot" and time series images into 512×512 matrices of data in which matrix entry $a_{i,j}$ is proportional to the average intensity of light striking pixel (x_i, z_j). In a typical snapshot image, the physical dimension of an individual pixel is approximately $0.2\,\mathrm{cm} \times 0.2\,\mathrm{cm}$. Furthermore, in constructing time series images, temporal resolutions as small as $1/30\,\mathrm{s}$ can be obtained.

Experiments were run three-at-a-time. In other words, three intrusions, of progressively larger densities, were released in sequence where in each case, sufficient time ($\sim 10\,\mathrm{min}$) was allowed between runs to permit the decay of the internal gravity waves in the stratified fluid. Although mixing and deposition of lock fluid at the interface resulted in successively broader interfacial thicknesses between runs (see *e.g.* Figure 3.2), separate experiments showed that the depth of the mixed region was sufficiently smaller than the intrusion depth that this variation in the density profile had negligible effect.

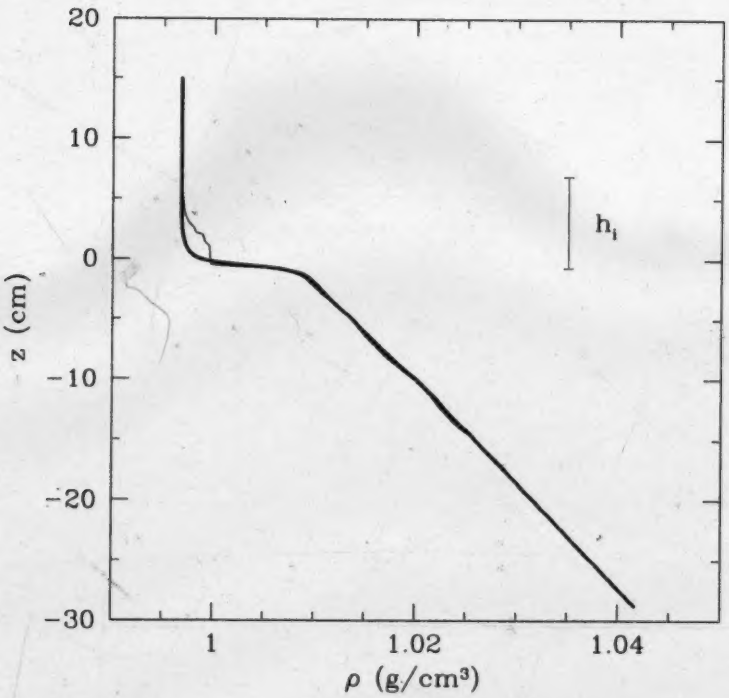

Figure 3.2: Measured density profiles corresponding to the experiment for which $N^2 = 1.15\,\mathrm{s}^{-2}$ and $\sigma_* = 0.0102$. The heavy solid line indicates the initial profile, whereas the thin solid line shows the profile following the release of the third intrusion. The intrusion height, h_i, for this particular run is indicated by the vertical line.

3.2 Synthetic Schlieren - Determination of Δz

The internal gravity waves that appeared in the (stratified) lower layer were visualised using "synthetic schlieren", a technique that is described in detail in Sutherland *et al.* [90] (see also Dalziel, Hughes & Sutherland [16]). It exploits variations in the index of refraction with density in order to visualize and measure the deflection of light rays as they travel through stratified fluid of spatially and temporally varying density gradient. More specifically, light rays are deflected upwards (downwards) when internal gravity waves compress (stretch) an isopycnal layer. By measuring the apparent vertical displacement (Δz) field of an object image placed behind the tank (*e.g.* a grid of 0.5 cm thick horizontal black and white lines), one can determine the amplitude of the waves continuously and non-intrusively.

Consider for example Figure 3.3 in which the excitation of internal gravity waves in a uniformly stratified fluid by a vertically oscillating sphere is depicted (Onu, Flynn & Sutherland [65]; see also Flynn, Onu & Sutherland [26] and Sutherland, Flynn & Onu [92]). Figures 3.3a and 3.3b show images of the tank immediately prior to the experiment and following two oscillation periods, respectively. To the naked eye, the images appear identical; no wave motion is apparent. By digitizing the images shown in Figures 3.3a and 3.3b and computing their difference, however, strong internal gravity wave radiation along the upper and lower flanks of the sphere is evident. This is shown by the qualitative synthetic schlieren image depicted in Figure 3.3c. The waves propagate upwards and to the right such that the lines of constant phase form an angle of $\Theta = \cos^{-1}(\omega/N) \simeq 60^o$ to the vertical.

The corresponding apparent vertical displacement (Δz) field of the object image is computed using a quadratic interpolation scheme. Suppose for example that the intensity of the pixel occupying coordinate (x_p, z_p) at time t_0 is $I(x_p, z_p)$. If, during a time interval Δt, deflections to the background density gradient result in an apparent vertical displacement Δz_p, the new pixel

intensity can be estimated from (Sutherland *et al.* [90])

$$I'(x_p, z_p) \simeq I(x_p, z_p - \Delta z_p). \tag{3.1}$$

The vertical displacement of the object image in Cartesian (as opposed to pixel) coordinates is then determined as follows

$$\Delta z = (z_{-1} - z_0)\frac{(I' - I_0)(I' - I_{+1})}{(I_{-1} - I_0)(I_{-1} - I_{+1})} + (z_{+1} - z_0)\frac{(I' - I_0)(I' - I_{-1})}{(I_{+1} - I_0)(I_{+1} - I_{-1})}. \tag{3.2}$$

In the above equation, $I_{\pm 1} = I(x_p, z_{\pm 1}) = I(x_p, z_p \pm 1)$ whereas $I_0 = I(x_p, z_p)$.

Equation 3.2 is applied at all points for which $I_{-1} < I_0 < I_{+1}$ or $I_{-1} > I_0 > I_{+1}$. In addition, adjacent pixels must satisfy the following threshold conditions: $|I_{-1} - I_0| > 10$ and $|I_{+1} - I_0| > 10$. In situations where the above conditions are not met (corresponding typically to pixels at the center of a black or white line), Δz is determined using a Gaussian-weighted interpolation scheme. Finally, fast and Fourier domain low-pass filters are applied to the data to remove high-frequency noise, which is due primarily to signal degradation associated with the conversion from a digital to an analog signal and temperature fluctuations in the air space between the camera and the tank.

The vertical displacement field corresponding to the qualitative synthetic schlieren image depicted in Figure 3.3c is shown in Figure 3.3d. As indicated by the color bar, the apparent vertical displacement of the grid of horizontal lines due to internal gravity wave motion is relatively small. This explains why the waves are difficult to visualise directly *e.g.* from Figure 3.3b.

Whereas in the study of Onu, Flynn & Sutherland [65] Δz is a function of the spatial coordinates x and z, here we compute the apparent vertical displacement field from vertical time series of the wave field at a fixed horizontal position, x. In the present study therefore, $\Delta z = \Delta z(t, z)$.

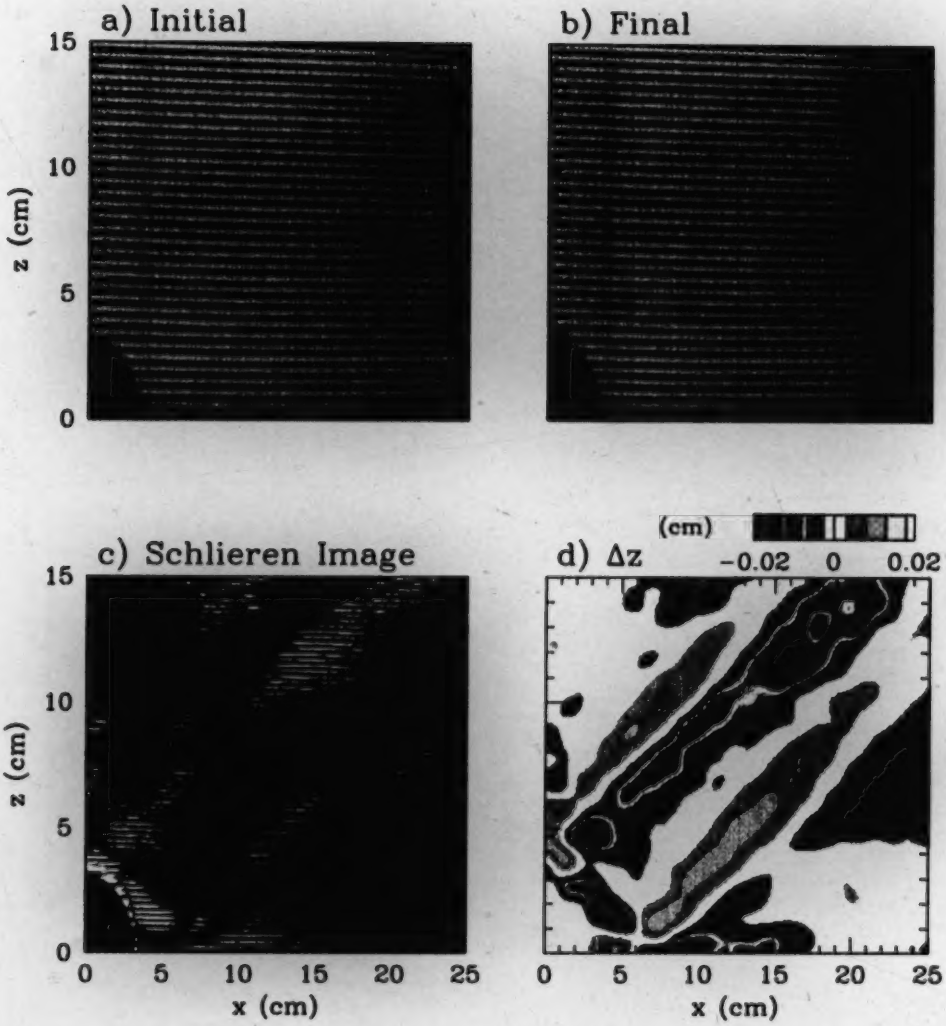

Figure 3.3: Snapshot images (a) prior to oscillation and (b) immediately following two oscillations. Subtracting (a) from (b) yields the qualitative synthetic schlieren image depicted in (c). The corresponding Δz field is shown in (d).

3.3 Synthetic Schlieren - Determination of ΔN^2 and N_t^2

This section describes how internal gravity wave amplitudes are determined from measurements of the apparent vertical displacement field, Δz. The equations presented herein are based on the results of Sutherland *et al.* [90] whose analysis guides the present discussion.

The path taken by a light ray as it travels through a stratified environment in which the index of refraction, n, is a function of density is given by Snell's Law

$$n \cos\phi = C, \tag{3.3}$$

where ϕ is the angle of incidence of the light with respect to surfaces of constant n, which are assumed parallel with the horizontal, and C is a constant. In the present context, $n = n(x, y, z)$ and $\phi = \phi(x, y, z)$ in which x, y and z represent along, spanwise and vertical coordinates, respectively. The analysis of equation (3.3) is facilitated by introducing the along-ray coordinate s for which

$$s = s_{\parallel} + s_{\perp}, \tag{3.4}$$

where $s_{\parallel}$ and $s_{\perp}$ are, respectively, coordinates parallel and perpendicular to surfaces of constant n. Differentiating equation (3.3) with respect to s, it can be shown that

$$\frac{\partial n}{\partial s}\cos\phi - n\sin\phi\frac{d\phi}{ds} = 0. \tag{3.5}$$

However,

$$\frac{ds_{\perp}}{ds} = \sin\phi,$$

and hence,

$$\frac{\partial n}{\partial s_{\perp}}\cos\phi\sin\phi - n\sin\phi\frac{d\phi}{ds} = 0. \tag{3.6}$$

Moreover,

$$\frac{d^2 s_{\perp}}{ds_{\parallel}^2} = \sec^3\phi\frac{d\phi}{ds}. \tag{3.7}$$

Combining equations (3.6) and (3.7), we find that

$$\frac{d^2 s_\perp}{ds_\parallel^2} = \frac{\sec^2 \phi}{n} \frac{\partial n}{\partial s_\perp}. \tag{3.8}$$

Because spanwise variations in the internal gravity wave field are presumed negligible, $s_\parallel$ corresponds to the spanwise coordinate, y. Furthermore, because it is also appropriate to assume that $|ds_\perp/ds_\parallel| \ll 1$, we may linearize equation (3.8) as follows

$$\frac{d^2 z}{dy^2} = \frac{\sec^2 \phi_{iz}}{n_i} \frac{\partial n}{\partial z}. \tag{3.9}$$

In the above equation, ϕ_{iz} is the angle of incidence to the y-axis in the z direction whereas n_i is the index of refraction at the point (x_i, y_i, z_i) where the ray first enters the tank. Equation (3.9) can be simplified by noting that

$$\frac{\partial n}{\partial z} = \frac{dn}{d\rho} \cdot \frac{\partial \rho}{\partial z} = -\left(\frac{1}{g} \frac{\rho_{00}}{n_{00}} \frac{dn}{d\rho}\right) n_{00} N^2 = -\gamma n_{00} N^2, \tag{3.10}$$

where n_{00} and ρ_{00} denote reference refractive indices and densities, respectively. Because the index of refraction of salt water varies approximately linearly with density (Weast [97]), γ is roughly constant. Specifically, $\gamma \simeq 1.878 \cdot 10^{-4}\,\mathrm{s}^2/\mathrm{cm}$. Integrating equation (3.9) under the assumption that $\sec^2 \phi_{iz} \simeq 1$, it can therefore be demonstrated that

$$z(y) = z_i + y \tan \phi_{iz} - \frac{1}{2} \gamma N^2 y^2. \tag{3.11}$$

Combining equations (3.3) and (3.11), the total vertical deflection of a light ray as it passes from the screen of horizontal black and white lines to the camera lens is given by

$$\begin{aligned} z(N^2, \phi_0) \simeq\ & L_c \phi_0 + L_G \left(\frac{n_a}{n_G}\right) \phi_0 + L_g \left(\frac{n_a}{n_w}\right) \phi_0 - \frac{1}{2} \gamma N^2 L_g^2 \\ & + L_G \left(\frac{n_a}{n_G}\right) \phi_0 - L_G \left(\frac{n_w}{n_G}\right) \gamma N^2 L_g + L_s \phi_0 - L_s \left(\frac{n_w}{n_a}\right) \gamma N^2 L_g, \end{aligned}$$

where ϕ_0 is the angle the light makes with the horizontal as it enters the CCD camera. Furthermore, $n_a = 1$, $n_w = 1.333$ and $n_G = 1.49$ are the refractive indices of air, water and glass, respectively. Finally, $L_c = 400\,\mathrm{cm}$ is

the distance from the front of the camera lens to the tank, $L_G = 1.2\,\text{cm}$ is the tank wall thickness, $L_g = 17.6\,\text{cm}$ is the inside tank width and $L_s = 27.9\,\text{cm}$ is the distance from the tank to the screen (see Figure 3.1b).

When the image of horizontal black and white lines is distorted due to the presence of internal gravity waves, the apparent vertical displacement of the lines, Δz, is determined from

$$\Delta z(\Delta N^2, \phi_0) \simeq -\frac{1}{2}\gamma \Delta N^2 L_g^2 - L_G\left(\frac{n_w}{n_G}\right)\gamma \Delta N^2 L_g - L_s\left(\frac{n_w}{n_a}\right)\gamma \Delta N^2 L_g, \tag{3.12}$$

where $\Delta N^2 = -(g/\rho_{00})\partial\rho/\partial z$ is the perturbation to the squared buoyancy frequency. Equation (3.12) can be re-arranged to give ΔN^2 as an explicit function of Δz

$$\Delta N^2 \simeq -\frac{\Delta z}{\gamma}\left[\frac{1}{2}L_g^2 + L_g n_w\left(\frac{L_G}{n_G} + \frac{L_s}{n_a}\right)\right]^{-1}, \tag{3.13}$$

or more simply,

$$\Delta N^2 \simeq -\alpha \Delta z. \tag{3.14}$$

In the present study, $\alpha = 6.4\,\text{cm}^{-1}\text{s}^{-2}$. Therefore, by measuring Δz from equation (3.2), an estimate of the perturbation to the squared buoyancy frequency due to the propagation of internal gravity waves can be derived.

In addition to measuring the apparent displacement of a point from its original position, one may also compute the displacement that occurs during a short time interval, Δt. Hence, it is possible to estimate the time derivative of the ΔN^2 field, N_t^2, using the following relation

$$N_t^2 \simeq -\alpha \Delta z/\Delta t. \tag{3.15}$$

The wave amplitude as measured in the N_t^2 field, $A_{N_t^2}$, may be related to the amplitude of the vertical displacement field, A_ξ. Explicitly, for Boussinesq linear plane waves propagating in a uniformly stratified fluid, it has been shown by Sutherland *et al.* [90] that

$$A_\xi = \frac{A_{N_t^2}}{k_z \omega N^2}, \tag{3.16}$$

where ω and k_z are the wave frequency and vertical wavenumber, respectively. The measurement of A_{N^2}, ω and k_z is described in Chapter 4.2.

Finally, we note that in situations for which the internal gravity wave field is not spanwise uniform, ΔN^2 is not linearly related to Δz. Rather, inverse tomographic techniques are required to determine ΔN^2 from the apparent vertical displacement of the object image. As described in detail in Onu, Flynn & Sutherland [65], this is an area of considerable complexity. Further discussion is beyond the scope of the present study.

3.4 Signal Strength

Internal gravity waves were observed in all cases except the three experiments with the weakest stratification for which $N^2 = 0.37\,\mathrm{s}^{-2}$. For these three experimental runs, the absence of observed waves is primarily an artifact of the synthetic schlieren technique: for a wave of fixed amplitude and spatial structure, the apparent vertical displacement of the horizontal lines, Δz, is proportional to N^3. Hence, the signal from internal gravity waves can be detected and enhanced above noise levels only if N is significantly large.

Chapter 4

Qualitative Observations and Results

4.1 Fluid Intrusions

Gravity currents propagating in stratified media are subject to interactions with internal gravity waves whenever v_i is approximately less than $v_{LW} = NH_s/\pi$, the velocity of the longest linear mode-one wave that can exist in a uniformly stratified fluid of depth H_s (Maxworthy *et al.* [57]). For symmetric fluid intrusions propagating horizontally through a uniformly stratified ambient, we demonstrate in Appendix D that

$$\frac{v_i}{v_{LW}} < \frac{\mathrm{Fr} \cdot \pi}{\sqrt{2}}, \tag{4.1}$$

where Fr represents a Froude Number whose magnitude depends on the steady state depth of the intrusion relative to that of the stratified ambient.

The above analysis is too rudimentary, however. First, it omits any consideration of the magnitude of the forcing imparted by the intrusion. This argument was employed by Amen & Maxworthy [3] in explaining differences between their experimental results and those of Wu [99]. More specifically, in Amen & Maxworthy's [3] study, the initial height of the intrusion immediately following the release of the gate $(h_i/H_s)_{t=0} \geq 0.40$ and a strong internal gravity

wave-intrusion interaction was observed. By contrast, no such interaction developed in the experiments of Wu [99] for whom $(h_i/H_s)_{t=0} = 0.25$. The recent experiments of de Rooij [20] (see also Faust & Plate [25]) suggest that the situation is still more complicated in that other factors may also be important in determining the magnitude of the internal gravity wave-intrusion interaction. Rather than speculate on the nature of these factors, we note that the present study considers fluid intrusions whose relative depth of penetration into the stratified layer, h_-/H_-, is typically small. This is demonstrated for example by Figure 4.1 which shows a representative image of the fluid intrusion head. Consistent with the analysis of Faust & Plate [25] and de Rooij [20], we find that no rhythmic coupling between the intrusion and the internal gravity waves develops and that over the domain of interest ($0 \leq x \leq L_w$), the intrusion behaves as a slumping gravity current; v_i and h_i are approximately constant. In all cases, experiments are terminated before the intrusion's motion becomes self-similar.

The image of the fluid intrusion shown in Figure 4.1 is similar to Figure 3(c) of Rottman & Simpson [73] who considered the behaviour of bottom-propagating gravity currents. In particular, we note that when the return flow of uniform ambient fluid of density ρ_+ reaches the tank wall, its reflection generates a forward-propagating rear bore that travels toward the intrusion head. By contrast, no rear bore is excited along the underside of the intrusion, which initially does not penetrate into the (lower) stratified layer. These observations are consistent with the empirical results of Rottman & Simpson [73] who found that forward-propagating rear bores can only develop when the initial height of the gravity current is greater than or equal to approximately 70% of the height of the ambient fluid. (For details, see also §1 of Moodie [63].)

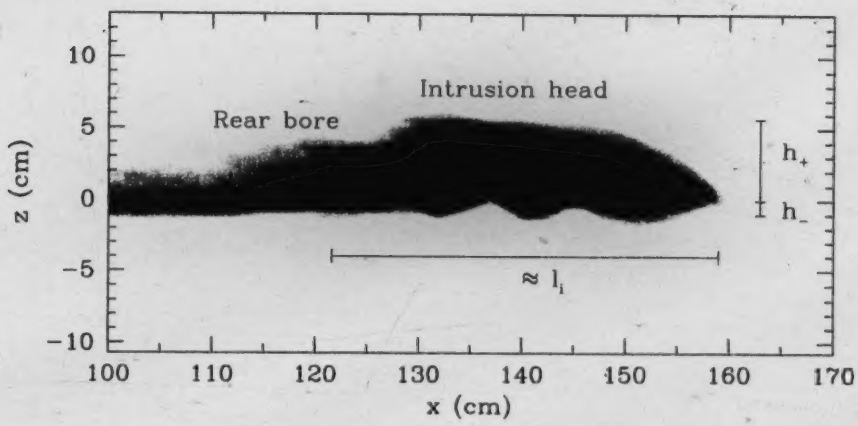

Figure 4.1: Image of the intrusion head for the experiment in which $N^2 = 0.67\,\mathrm{s}^{-2}$, $\sigma_* = 0.0038$ and $\sigma_i = 0.0006$. The top of the $\sim 1\,\mathrm{cm}$ thick interfacial layer corresponds to the line $z = 0\,\mathrm{cm}$. The distances h_+, h_- and l_i are as indicated.

Unlike the bottom-propagating gravity currents observed by Rottman & Simpson [73], Figure 4.1 shows the development of pronounced undulations along the underside of the intrusion head. These undular patterns were noted in 19 of the 39 trials and are believed to result from a weak Kelvin-Helmholtz instability. They were also noted in the studies of Sutherland, Kyba & Flynn [93], who considered the propagation of a fluid intrusion between uniform layers, and Dugan, Warn-Varnas & Piacsek [24], who developed a numerical model describing the gravitational collapse of a mixed region in a stratified ambient.

Generally speaking, the undulations were observed in runs for which σ_* was relatively small and σ_i was relatively large. Because v_i increases with ρ_i, the stress imparted by the intrusion on the fluid below the interface, and hence the undulation amplitude, A_u, are expected to increase with σ_i. Conversely, as $\sigma_* - \sigma_i$ increases, a larger amount of energy is required to lift fluid at or near the interfacial layer. Therefore, A_u is expected to decrease with increasing σ_*.

As described in Mehta, Sutherland & Kyba [59], v_i was determined from horizontal time series of the digitized experimental images. Values for h_+ and h_- were found from vertical time series constructed along a vertical slice at $x \simeq L_l = 18.6\,\mathrm{cm}$. Measurements were made roughly half-way between the leading and trailing edges of the intrusion head. In those experiments in which undulations were observed along the underside of the intrusion, h_- was measured halfway between an undular peak and an undular trough. For example, $h_+ = 5.7 \pm 0.2\,\mathrm{cm}$ and $h_- = 1.0 \pm 0.2\,\mathrm{cm}$ for the intrusion depicted in Figure 4.1.

Vertical time series along $x \simeq L_l = 18.6\,\mathrm{cm}$ were also employed to determine $T_i = 2\pi/\omega_i$, where T_i and ω_i denote, respectively, the characteristic period and frequency associated with the forcing imparted by the intrusion head. The head's horizontal extent, l_i, was then estimated from $l_i = v_i T_i$. More precisely, l_i corresponds to the distance between the intrusion's (typically sharp) tip and the projected location at which the height of the intrusion head is equal to the height of the trailing tail. For example, Figure 4.1 shows

an intrusion for which $l_i = 37.2 \pm 5.0\,\mathrm{cm}$. Errors associated with l_i are due to the development of the rear bore and billows along the top and back of the intrusion head both of which make it difficult to determine the precise location at which the trailing tail begins.

4.2 Internal Gravity Waves

Vertical time series of the N_t^2 field were constructed along 15 equally spaced columns ranging between $x \simeq 10\,\mathrm{cm}$ and $35\,\mathrm{cm}$ to the right of the gate. For $x \gtrsim 35\,\mathrm{cm}$, upward propagating internal gravity waves reflecting from the bottom of the tank significantly interfered with the downward propagating waves.

Figure 4.2 shows a composite vertical time series taken along the vertical slice $x = 18.4\,\mathrm{cm} \simeq L_l$ for a particular experimental run. It indicates that the shear forces exerted by the fluid intrusion generate a region of intense isopycnal distortion immediately below the intrusion head. Moreover, the internal gravity waves that appear below this region are relatively regular in spatio-temporal structure. The wave amplitude decreases with vertical distance from the wave source due to the combined effects of viscous attenuation and wave dispersion.

Because the intrusion speed is approximately constant, Figure 4.2 is roughly equivalent to a snapshot image with the horizontal dimension indicated. In performing the Galilean translation from t to x, we use the speed of propagation of the intrusion, $v_i = 2.2\,\mathrm{cm/s}$, not the horizontal internal gravity wave speed, $v_{igw} = \omega/k_x = 3.0\,\mathrm{cm/s}$, in which ω and k_x represent the characteristic internal gravity wave frequency and horizontal wavenumber, respectively. Because these speeds are not equal, Figure 4.2 cannot be regarded as a "true" snapshot image. Nonetheless, it suggests that there is a correlation between the horizontal length scale of the internal gravity waves and the head of the fluid intrusion. This idea is explored in more detail in Chapter 5.2.

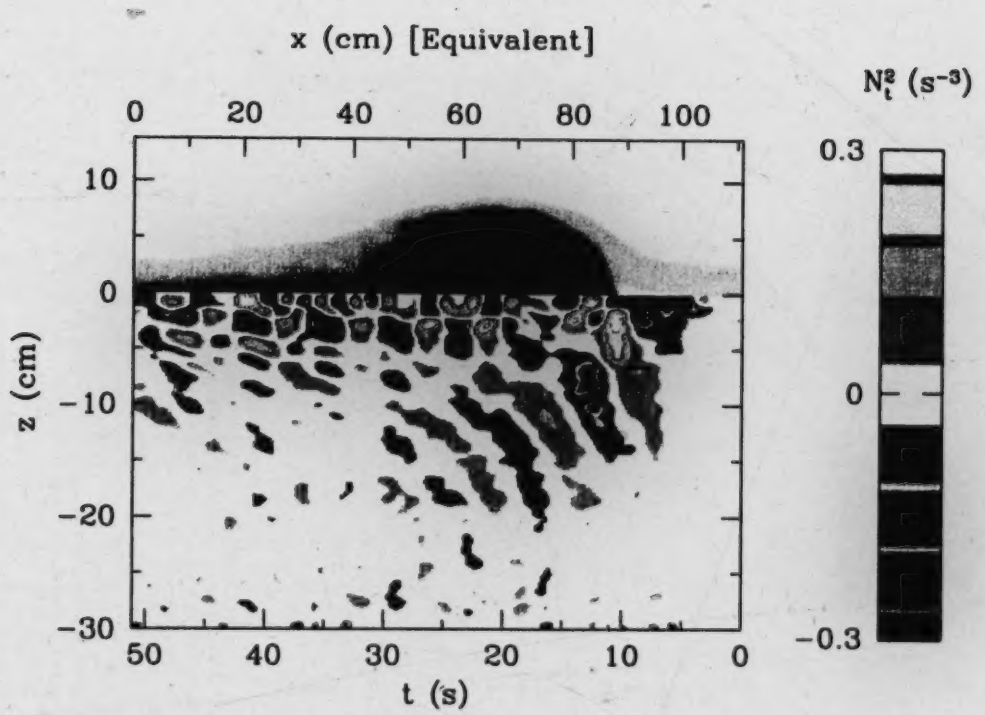

Figure 4.2: Composite time series along the vertical slice $x/L_l = 0.99$ corresponding to the experiment for which $N^2 = 1.17\,\mathrm{s}^{-2}$, $\sigma_* = 0.0037$ and $\sigma_i = 0.0020$. The equivalent horizontal scale is indicated by the top axis.

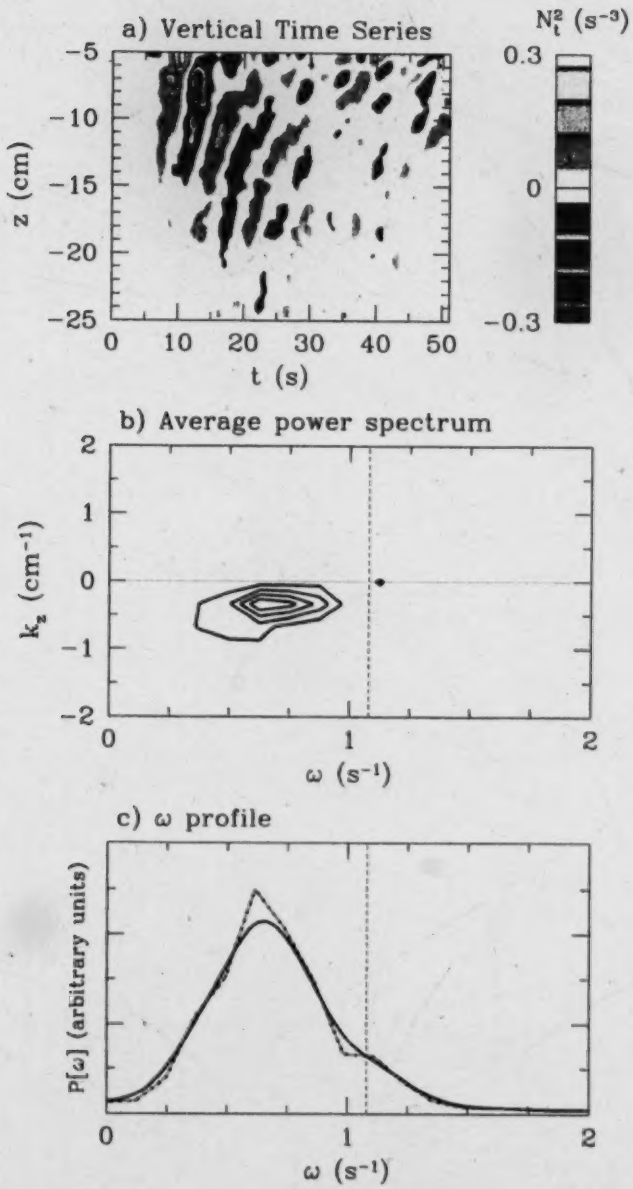

Figure 4.3: (a) Vertical time series of the N_t^2 field (see also Figure 4.2). (b) The average power spectrum. (c) The ω profile corresponding to (b). The dashed-and-dotted line denotes the unsmoothed profile whereas the solid line denotes the smoothed profile. In both (b) and (c), the N value ($N = 1.08\,\mathrm{s}^{-1}$) for this particular experimental run is indicated by the vertical dashed line.

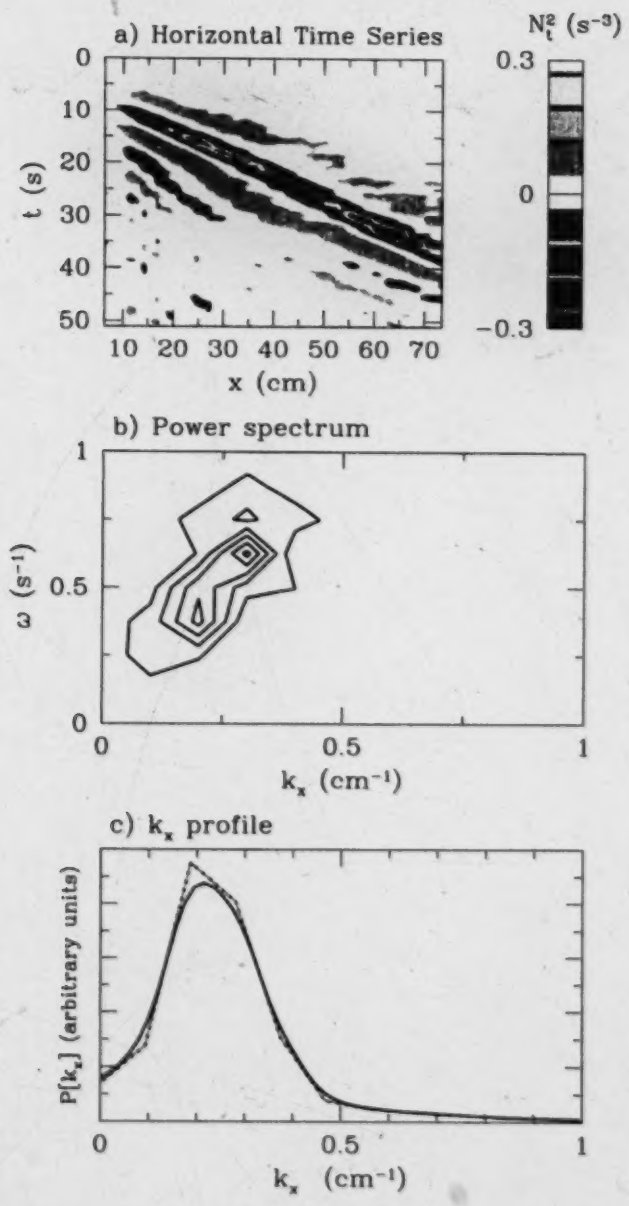

Figure 4.4: (a) Time series of the N_t^2 field along the horizontal slice $z/h_- = -2.0$ for the experimental run described in Figures 4.2 and 4.3. (b) The power spectrum corresponding to (a). (c) The k_x profiles as derived from (b). Line types are as indicated in Figure 4.3c.

Estimates of ω and k_x were obtained by applying an analysis similar to that described in §4(B) of Dohan & Sutherland [23]. Consider for example Figure 4.3a, in which the image from Figure 4.2 is reproduced over the truncated vertical range $-25 \leq z \leq -5\,\mathrm{cm}$. The spectrum (in $\omega - k_z$ space) corresponding to this image was computed using a two-dimensional Fourier transform. It was then averaged with the spectra from the 14 other vertical time series from which the arithmetic mean spectrum shown in Figure 4.3b was obtained. The ω profile depicted in Figure 4.3c was computed by summing over k_z in the average spectrum. This profile was subsequently smoothed using a Gaussian smoothing procedure that employed a bin size of $0.1\,\mathrm{s}^{-1}$. Although the smoothing routine changes the profile's peak value, it does not significantly alter the location of the maximum, which in the present case appears at $\omega \simeq 0.65\,\mathrm{s}^{-1}$. We consider this to be the characteristic value of ω for the generated internal gravity waves.

We did not compute values for k_z from Figure 4.3b because the vertical scale of the internal gravity waves was comparable with the vertical extent of the field of view. Instead, horizontal time series of the N_t^2 field were reconstructed by combining data from 27 equally spaced vertical time series ranging from $x \simeq 5\,\mathrm{cm}$ to $x \simeq 75\,\mathrm{cm}$. From these, estimates of k_x were derived by computing the associated power spectrum (in $k_x - \omega$ space) then averaging this spectrum over ω (see Figures 4.4a, b and c). The k_x profile was subsequently smoothed using a Gaussian smoothing procedure having a bin size of $0.05\,\mathrm{cm}^{-1}$. Although significant wave reflection off the bottom of the tank is observed for $x \gtrsim 35\,\mathrm{cm}$ this measurement technique is nonetheless robust because the horizontal wavenumber is unaltered by reflection.

Although characteristic values for ω could be determined from power spectra such as that shown in Figure 4.4b, these estimates would be less reliable than those derived directly from the vertical time series owing to the additional step associated with the reconstruction of the horizontal time series from the vertical time series. In addition, because the wave envelope is narrower in Figure 4.4a as compared to Figure 4.3a, the peaks in the corresponding power

spectrum are less pronounced.

Knowing N, ω and k_x, values for k_z and $\Theta = \cos^{-1}(\omega/N)$ were determined using the dispersion relation for internal gravity waves (see Appendix E). Consistent with the study of Wu [99], we observe some evolution of the internal gravity wave field over the course of a particular experiment as characterized by an increase in Θ with x. Because we are primarily interested in the behaviour of the internal gravity waves in the relatively brief period immediately following the initial, transient collapse of the lock fluid during which wave reflection off the bottom of the tank can be neglected, however, we consider the waves to be well represented by characteristic values for ω and k_x. In particular, the Fourier analysis technique described above is robust in that it is insensitive to the contribution of lingering transient internal gravity waves excited during the initial collapse stage. For example, if in Figure 4.3b the average power spectrum included only those vertical time series for which $x \simeq 19\,\text{cm}$ to $35\,\text{cm}$, we would find that $\omega \simeq 0.61\,\text{s}^{-1}$. This result is within 6% of the value determined from Figure 4.3c.

More caution is required, however, when considering the wave amplitude, $A_{N_t^2}$, which is determined from the vertical time series of the N_t^2 field. Explicitly, $A_{N_t^2}$ is measured by computing ΔI, the maximum difference in pixel intensity between an adjacent wave trough and wave crest. The wave amplitude is then computed as follows

$$A_{N_t^2} = \frac{\Delta I}{\Delta I_M} \cdot \widehat{A_{N_t^2}},$$

where $\Delta I_M = 512$ and $\widehat{A_{N_t^2}}$ represents the threshold amplitude. For example, in generating Figure 4.2, a threshold amplitude of $\widehat{A_{N_t^2}} = 0.3\,\text{s}^{-3}$ is employed. As demonstrated by Figure 4.5, which shows $A_{N_t^2}$ as a function of x, significant variability in $A_{N_t^2}$ exists near the lock-release point indicating that the measurement technique is sensitive to the forcing of the stratified layer during the initial collapse stage. Because the magnitude of the overshoot decreases as N^2 increases, the magnitude of the transient disturbance is larger when N^2 is relatively small. As the transient signature decays, however, $A_{N_t^2}$ obtains

a more or less constant value. Characteristic wave amplitudes were therefore determined from time series corresponding to $x \simeq L_l = 18.6\,\mathrm{cm}$. Because the wave amplitudes decrease as the wavepackets propagate downwards, $A_{N_l^2}$ was measured just below the region of intense isopycnal distortion where the amplitudes were close to their largest values.

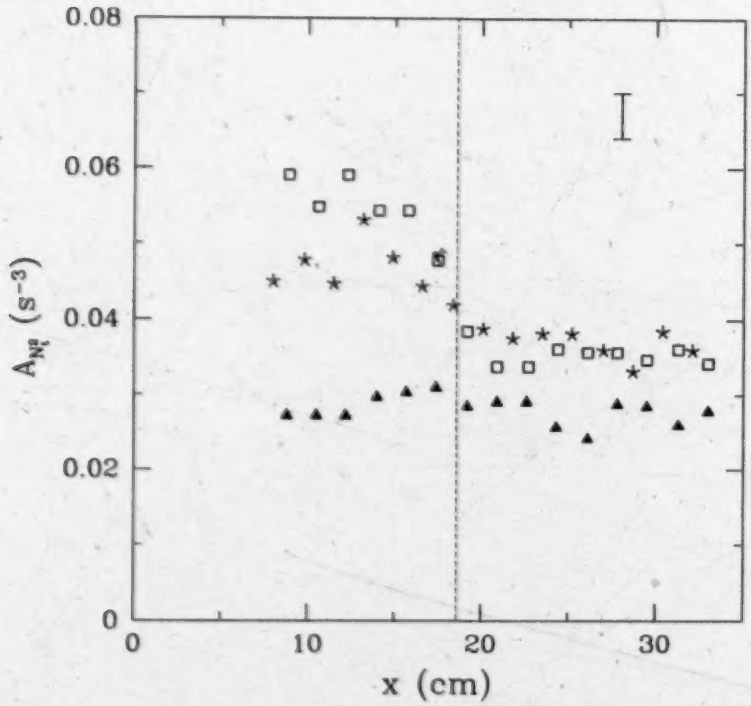

Figure 4.5: Variation in $A_{N_i^2}$ with x for three different experimental runs. Data point types are as follows - open squares: $N^2 = 0.69\,\mathrm{s}^{-2}$, $\sigma_* = 0.0024$, $\sigma_i = 0.0019$; stars: $N^2 = 0.92\,\mathrm{s}^{-2}$, $\sigma_* = 0.0027$, $\sigma_i = 0.0018$; solid triangles: $N^2 = 1.15\,\mathrm{s}^{-2}$, $\sigma_* = 0.0102$, $\sigma_i = 0.0020$. The dotted line indicates the distance one lock-length from the gate, which is situated at $x = 0\,\mathrm{cm}$. The error bar denotes the typical measurement uncertainty.

Chapter 5

Quantitative Results

5.1 Fluid Intrusions

Figure 5.1 shows measured values of h_+/H_+ and h_-/H_+ as a function of ζ_* in which

$$\zeta_* = \frac{\rho_i - \bar{\rho}_*}{\tilde{\rho} - \rho_+}, \tag{5.1}$$

where $\bar{\rho}_* = (\tilde{\rho} + \rho_+)/2$ and $\tilde{\rho} = \max(\rho_*, \rho_i)$.[1] For comparison, the figure also shows theoretical curves determined from HH80's coupled system of cubic polynomials for the case where $H_+ \ll H_-$. Also presented are the first-order asymptotic approximations to these relations given by equations (2.22) and (2.23).

Experimental values for h_+/H_+ are effectively independent of ζ_* and N^2. The theory of HH80 moderately overpredicts the observed data. Their model provides a reasonable, albeit generally depressed, estimate of the trend exhibited by the experimental data shown in Figure 5.1b for $-1/2 \leq \zeta_* \lesssim 0.25$. Theoretical values typically underpredict experimental values by 25 to 50%.

For relatively dense intrusions ($\zeta_* \gtrsim 0.25$), the depth of penetration, h_-, becomes dependent on the strength of stratification: strongly stratified layers

[1] In the vast majority of experiments (36 of 39), $\tilde{\rho} = \rho_*$ (see Appendix C). Therefore, ζ_* is equivalent to ζ as defined by equation (2.15) with ρ_- replaced by the density of the top-most isopycnal layer of the stratified fluid, ρ_*.

inhibit the vertical motion of the intrusion more effectively than those that are weakly stratified. This is demonstrated most clearly by considering the four points lying between $\zeta_* = 0.29$ and $\zeta_* = 0.36$ for which h_-/H_+ decreases as N^2 increases. These results suggest that, insofar as the bulk dynamics of the intrusion are concerned, the stratification of the lower layer is not particularly important when $\zeta_* \lesssim 0.25$. Thereafter, h_- becomes dependent on N^2 and the dynamics influencing the intrusion's motion are more complicated than those considered by HH80. This latter observation is consistent with the analysis of Faust & Plate [25] who considered the propagation of a fluid intrusion within a uniformly stratified ambient and concluded that "intrusions... behave very differently from theoretical calculations" based on a two-layer model.

The normalized velocity is shown as function of ζ_* in Figure 5.2a. Consistent with the results demonstrated in Figure 5.1b, the experimental data shows reasonably good agreement with HH80's theory for $-1/2 \leq \zeta_* \lesssim 0.25$. These findings are in general accordance with those of Sutherland, Kyba & Flynn [93] who considered the behaviour of a fluid intrusion in a two-layer system for which both layers were uniform in density. They found reasonable qualitative agreement between their experimental data and a second-order asymptotic approximation to HH80's equations about the point $\epsilon = 0$.

For $\zeta \gtrsim 0.25$, however, agreement between theory and experiment is poor. In particular, for two-layer systems in which neither layer is density stratified, HH80 predict that $v_i \to 0$ as $\zeta \to (1/2)^-$ (see Figures 2.3 and 5.2a). When the bottom layer is uniformly stratified, however, v_i may also depend on N^2. More specifically, since h_- decreases as N^2 increases for $\zeta_* \gtrsim 0.25$, $v_i/\sqrt{\sigma_* g h_i}$ increases with N^2 over this same range of density parameters. When $\rho_i \geq \rho_*$ ($\zeta_* = 1/2$), the intrusion propagates at or below the level of the interface. Its character is therefore similar to that of a gravity current propagating in uniformly stratified surroundings (see *e.g.* Amen & Maxworthy [3] and Maxworthy *et al.* [57]). As described above, HH80 is not expected to provide accurate estimates of h_i or v_i in this regime. When $\zeta_* \lesssim 0.25$, however, little variation in $v_i/\sqrt{\sigma_* g h_i}$ with N^2 is observed. Within experimental error, v_i is

a function of ζ_* alone. Explicitly, from Figure 5.2b, we find that

$$\frac{v_i}{\sqrt{\sigma_* g h_i}} \propto \left(\zeta_* + \frac{1}{2}\right)^{0.32 \pm 0.02}, \quad \zeta_* \leq 0.25. \tag{5.2}$$

Consistent with the first-order asymptotic approximation given by equations (2.24) and (2.25) (see also Figure 2.3), experimental values for $v_i/\sqrt{\sigma_* g h_i}$ increase less rapidly than $(\zeta_* + 1/2)^{1/2}$.

Furthermore, the strength of the agreement between the experiments and the two-layer model of HH80 over a broad range of density parameters suggests that the excitation of internal gravity waves does not extract a significant portion of the intrusion's kinetic energy. This result complements the analysis of Ungarish & Huppert [96] who, in numerically modeling the slumping stage of Maxworthy *et al.*'s [57] experiments, surmised that "the energy imparted to the internal [gravity] waves is considerably less than the potential energy transferred into the gravity current." Interestingly, Maxworthy *et al.*'s [57] study considered the behaviour of a bottom-propagating gravity current from a full depth lock release and is therefore similar to that of de Rooij [20] (§5.5.1) wherein a fluid intrusion was released into stratified surroundings at mid-depth. de Rooij [20] noted, however, that "the internal [gravity] waves must play a significant role in reducing the propagation velocity." A quantitative comparison between the results of the present study and those of de Rooij [20] is considered in Chapter 5.4.

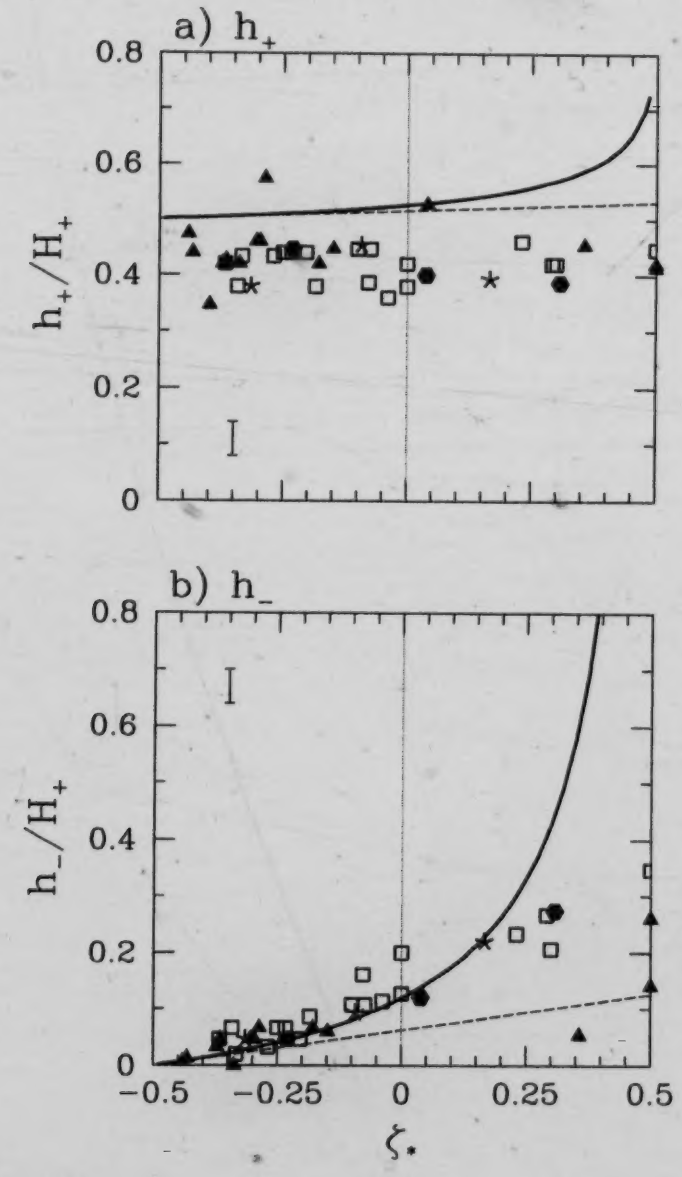

Figure 5.1: Normalized depth of penetration into the (a) upper and (b) lower layers. Data point types are as follows - closed hexagons: $N^2 = 0.37\,\mathrm{s}^{-2}$; open squares: $N^2 \simeq 0.67\,\mathrm{s}^{-2}$; stars: $N^2 = 0.92\,\mathrm{s}^{-2}$; closed triangles: $N^2 \simeq 1.17\,\mathrm{s}^{-2}$. The solid and dotted lines indicate the solutions predicted by HH80 and their first order asymptotic approximations, respectively. The error bars denote the typical measurement uncertainty.

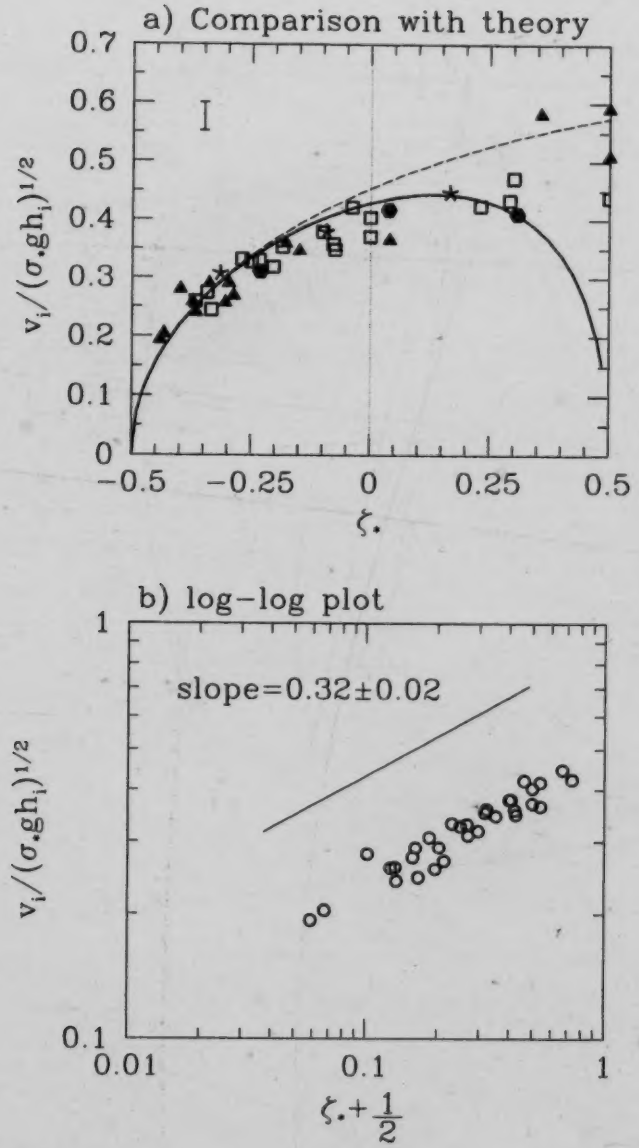

Figure 5.2: (a) Normalized intrusion velocity as a function of ζ_*. Data point and line types are as indicated in Figure 5.1. The error bar denotes the typical measurement uncertainty. (b) Log-log plot of the normalized intrusion velocity as a function of $\zeta_* + 1/2$ plotted for those experiments with $\zeta_* \leq 0.25$. The slope of the (vertically offset) best-fit line is indicated.

5.2 Internal Gravity Waves - Excitation

As described in Chapter 4.2, the generation of internal gravity waves is due primarily to two factors: the initial collapse of the lock fluid and the forcing imparted by the head of the fluid intrusion as it propagates along the interface. Here, focus is directed only to the latter, which represents the dominant mechanism of wave generation beyond $x \simeq L_l$ (see Figure 4.5).

Figure 5.3a shows the variation of A_ξ/λ_x with ζ_*. There exists a relatively large degree of error associated with the measurement of A_ξ. This is due primarily to the high degree of background noise in the wave field (see *e.g.* Figure 4.2). Although $A_{N_\ell^2}$ was determined consistently from one experiment to the next, Figure 4.5 indicates that even during the steady phase of the intrusion's motion, measurement errors of almost 20% are nonetheless possible.

Consistent with the results of Figure 5.1b, however, a positive correlation between A_ξ/λ_x and ζ_* is noted for $-1/2 \leq \zeta_* \lesssim 0.25$: heavier intrusions penetrate more deeply into the stratified layer and result in larger deflections to the isopycnal surfaces. This in turn yields larger amplitude internal gravity waves. Although the large degree of scatter makes it difficult to determine the precise relation between A_ξ/λ_x and ζ_*, Figure 5.2b suggests that

$$\frac{A_\xi}{\lambda_x} \propto \left(\zeta_* + \frac{1}{2}\right)^{0.37\pm0.06}, \qquad \zeta_* \leq 0.25. \tag{5.3}$$

When $\zeta_* \gtrsim 0.25$, A_ξ/λ_x is dependent on both ζ_* and N^2.

The variation of $k_x h_-$ with $(2\pi/l_i)h_-$ is shown in Figure 5.4a. Consistent with the interpretation of Figure 4.2 as a snapshot image, the collapse of the experimental data suggests that there is a direct correlation between the scale of the intrusion head and the wavelength of the internal gravity waves it excites. Explicitly,

$$k_x = C \cdot \frac{2\pi}{l_i}, \tag{5.4}$$

where $C = 1.32 \pm 0.07$.

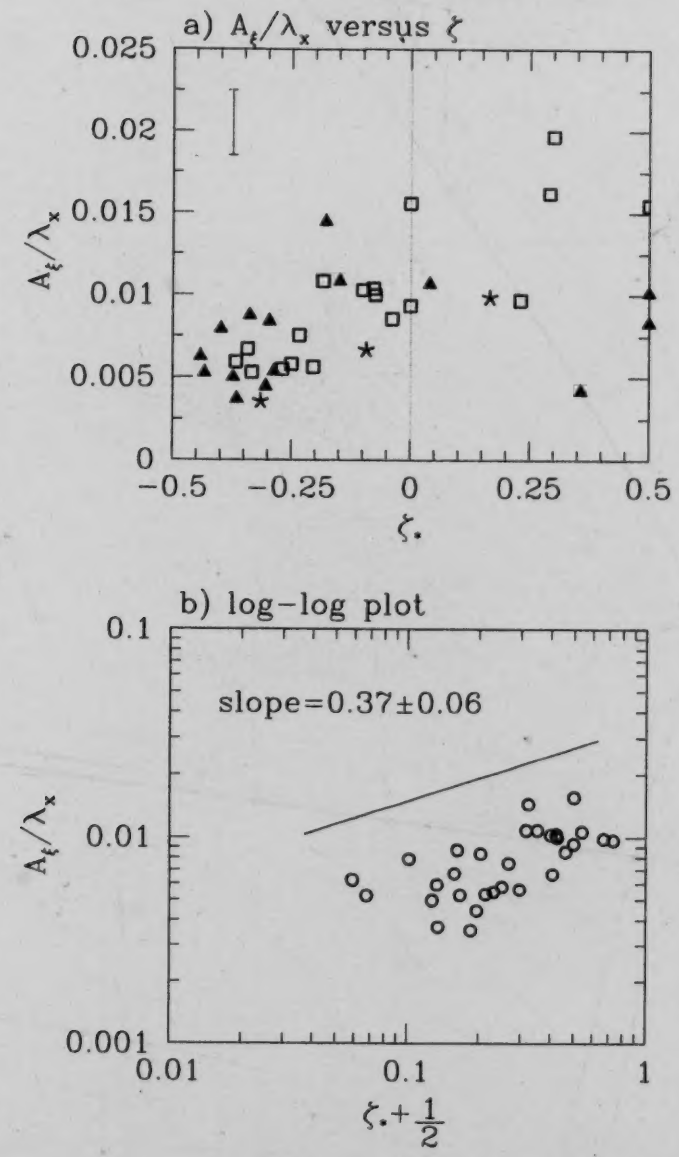

Figure 5.3: (a) Normalized amplitude of the vertical displacement field as a function of ζ_*. Data point types are as follows - open squares: $N^2 \simeq 0.67\,\mathrm{s}^{-2}$; stars: $N^2 = 0.92\,\mathrm{s}^{-2}$; closed trinagles: $N^2 \simeq 1.17\,\mathrm{s}^{-2}$. The error bar denotes the typical uncertainty in the measurement of A_ξ/λ_x. (b) Log-log plot of the normalized amplitude as a function of $\zeta_* + 1/2$ plotted for those experiments with $\zeta_* \leq 0.25$. The slope of the (vertically offset) best-fit line is indicated.

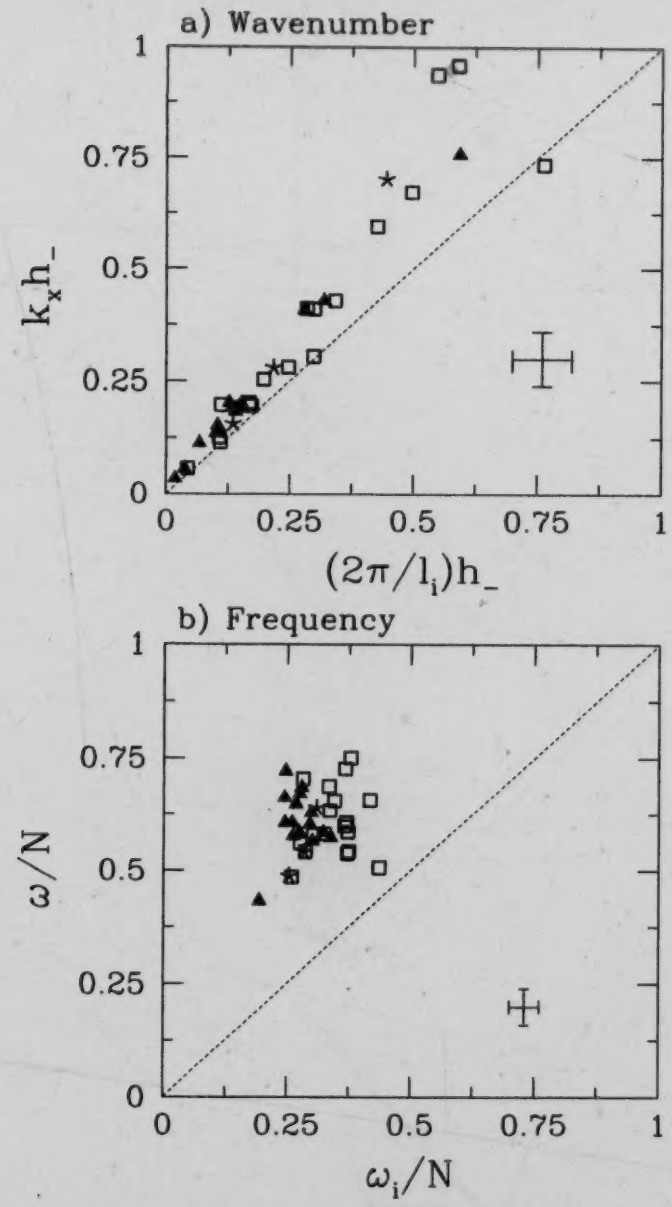

Figure 5.4: (a) Normalized horizontal wavenumber of the internal gravity waves versus the normalized inverse horizontal extent of the intrusion head. (b) Internal gravity wave frequency as a function of the frequency of the forcing imparted by the head of the intrusion. In both cases, data point types are as indicated in Figure 5.3; the error bars denote the typical measurement uncertainty.

No such relation exists between ω and $\omega_i = 2\pi(v_i/l_i)$, however. This is indicated by Figure 5.4b in which ω/N is plotted against ω_i/N: whereas the intrusion head forces the stratified layer at frequencies well below N, no systematic variation of ω with ω_i is observed. Nonetheless, Figure 5.5 shows that the frequency of wave propagation is not randomly determined. It shows A_ξ/λ_x as a function of Θ and indicates that the most pronounced internal gravity waves propagate within a relatively narrow band of angles to the vertical, Θ, ranging between 41^o and 64^o. Taken together, Figures 5.4 and 5.5 suggest that for internal gravity waves generated by the head of an intrusion, the horizontal wavelength is determined by the size of the intrusion head whereas the frequency of propagation is established relative to the buoyancy frequency such that $\Theta \simeq 53^o \pm 11^o$.

The results of Figure 5.5 show some discrepancy with those of Wu [99] who in studying wave excitation by the gravitational collapse of a mixed region in uniformly stratified surroundings found that the wave energy spectrum is sharply peaked about $\Theta \simeq 37^o$. Wu's [99] results are in good agreement with those of Linden [50] and Michaelian, Maxworthy & Redekopp [61] in which waves were generated, respectively, by a turbulent mixed layer and penetrative convection. In the former study, internal gravity waves were observed only within $0^o \leq \Theta \leq 35^o$. Furthermore, it was noted that "although it was impossible to determine the distribution of energy in the internal [gravity] wave field an impression was obtained that the major contribution occurred at the higher wave frequencies observed, as the dominant pattern appeared to be phase lines propagating at an angle of 35^o to the horizontal [*i.e.* $\Theta = 35^o$]." This value is moderately smaller than the range of angles ($42^o \leq \Theta \leq 55^o$) observed by Dohan & Sutherland [23], who also considered the excitation of internal gravity waves by a turbulent mixed layer. Wave propagation in this range was also noted by Sutherland & Linden [94] in their study of stratified flow over a thin barrier. A summary of the above results is presented in Table 5.1.

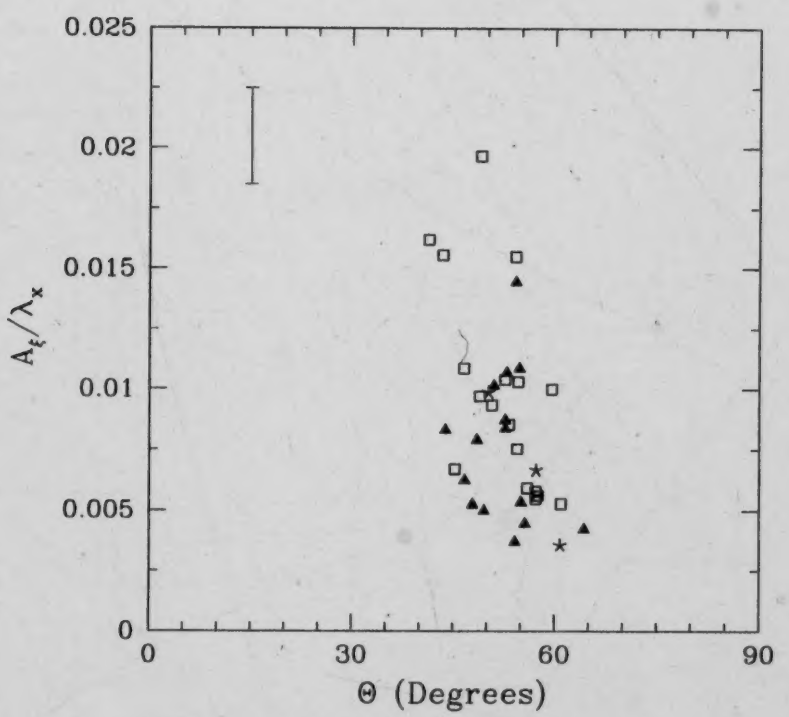

Figure 5.5: A_ξ/λ_x versus Θ. Data point types are as indicated in Figure 5.3. The error bar denotes the typical uncertainty in the measurement of A_ξ/λ_x.

Table 5.1: Characteristic angle of wave propagation in six studies involving the dynamic generation of internal gravity waves.

Study	Mechanism of internal gravity wave excitation	Θ
Wu [99]	Intrusive gravity current	$\simeq 37^o$
Linden [50]	Turbulence (no mean flow)	$\simeq 35^o$
Sutherland & Linden [94]	Turbulent shear flow	45.9^o to 59.9^o
Dohan & Sutherland [23]	Turbulence (no mean flow)	42^o to 55^o
Michaelian *et al.* [61]	Penetrative convection	30^o to 40^o
Present study	Intrusive gravity current	41^o to 64^o

In all of the above studies, it is appropriate to compare the experimentally observed values for Θ with those predicted by considering the vertical flux of either energy or horizontal momentum. Linear theory predicts that the period-averaged Reynolds stress per unit mass, $\langle u'w' \rangle$, imparted by the internal gravity waves is related to A_ξ by (Sutherland & Linden [94])

$$\langle u'w' \rangle = \frac{1}{4} N^2 A_\xi^2 \sin 2\Theta. \tag{5.5}$$

The maximum value of $\langle u'w' \rangle$ for waves of fixed amplitude occurs when $\Theta = 45^o$. Conversely, the angle at which the vertical energy flux per unit horizontal area, F_z, is maximized can be obtained from

$$F_z = \frac{1}{2} \frac{\rho_0 A_\xi^2 N^3}{k_x} \sin\Theta \cos^2\Theta. \tag{5.6}$$

For waves with fixed A_ξ and k_x, this is maximal when $\Theta = 35^o$.

In conjunction with equations (5.5) and (5.6), the narrow range of propagation angles observed by Dohan & Sutherland [23] was explained in terms of a weak, non-linear resonance between the internal gravity waves and their source. They noted that "since waves transport energy and momentum away from the turbulent region, waves with Θ in the range $35^o - 45^o$ may act most efficiently to modify the turbulence in a way that enhances their excitation." If this explanation applies to the dynamic mechanism of wave excitation considered here, it would necessarily require that the waves deform the head of the fluid intrusion. Although this coupling would have little impact on the bulk properties of the fluid intrusion (*e.g.* v_i, h_i), it could play an important dynamical role in a thin layer along the underside of the intrusion head. Specifically, the forcing imparted by the internal gravity waves would likely manifest itself as a series of small, interfacial distortions of amplitude $A_\xi \ll A_u$ where A_u denotes the amplitude of Kelvin-Helmholtz instabilities that may also appear (see *e.g.* Figure 4.1). Unfortunately, in a typical experiment, A_ξ is only twice the camera's vertical resolution. It is therefore impossible to determine whether the non-linear resonance postulated by Dohan & Sutherland [23] applies to the present case. Further study is required to fully explore this issue.

Figure 5.6 shows ω/N as a function of the normalized Kelvin-Helmholtz undulation frequency, ω_u/N. It indicates that in the vast majority of cases, the undulations forced the stratified fluid at frequencies in excess of N, the upper bound for ω. Furthermore, Figure 5.6 demonstrates that ω is not a multiple of ω_u. These observations suggest that although the forcing imparted by the intrusion onto the interfacial layer results in qualitatively significant flow features, these features are not primarily responsible for wave excitation. This result complements the conclusions of Wu [99] and Mei [60] who analyzed the gravitational collapse of a mixed region in a stratified fluid and found that "linear internal [gravity] waves [could] be generated quite effectively by the advancing nose of the mixed region alone" (Amen & Maxworthy [3]).

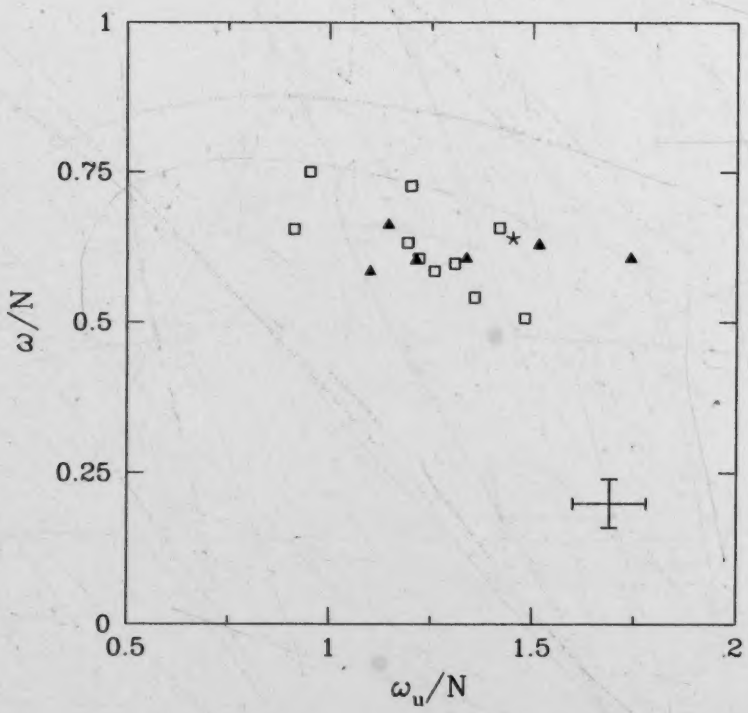

Figure 5.6: Normalized frequency of the internal gravity waves, ω, as a function of the normalized undulation frequency, ω_u. Data point types are as indicated in Figure 5.3. The error bars denote the typical measurement uncertainty.

5.3 Internal Gravity Waves - Stability

The data shown in Figure 5.5 are plotted on a different scale in Figure 5.7 in which the critical amplitudes for two types of wave instability are also presented. That labeled "OT" corresponds to an overturning instability which results when the internal gravity waves are of sufficient amplitude that they lift relatively dense fluid to the point where it lies above fluid of lesser density. As shown by Sutherland [87], this occurs when

$$\frac{A_\xi}{\lambda_x} > A_{OT} = \frac{1}{2\pi} \cot \Theta. \tag{5.7}$$

The curve labeled "SA" corresponds to an instability caused by the self-acceleration of the internal gravity waves. It is a consequence of a resonant interaction between the waves and the mean flow that they excite. A critical condition is obtained when

$$c_{g,x} = U_{max}, \tag{5.8}$$

where $c_{g,x}$ is the internal gravity waves' horizontal group velocity and U_{max} is the maximum horizontal velocity of the wave-induced mean flow. Practically speaking, instability is anticipated when

$$\frac{A_\xi}{\lambda_x} > A_{SA} = \frac{1}{2\pi\sqrt{2}} \sin 2\Theta. \tag{5.9}$$

As internal gravity waves increase in amplitude, Figure 5.7 indicates that the range of propagation angles for which wave breaking is anticipated also increases. For example, if $A_\xi/\lambda_x = 0.11$, only those waves for which $39^o < \Theta < 51^o$ are stable with respect to self-acceleration. The internal gravity waves observed in the present study are of much smaller amplitude than either A_{OT} or A_{SA}, however. Whereas large amplitude internal gravity waves can only exist within a narrow range of Θ, waves for which the angle of wave propagation falls within some small interval are necessarily large in amplitude.

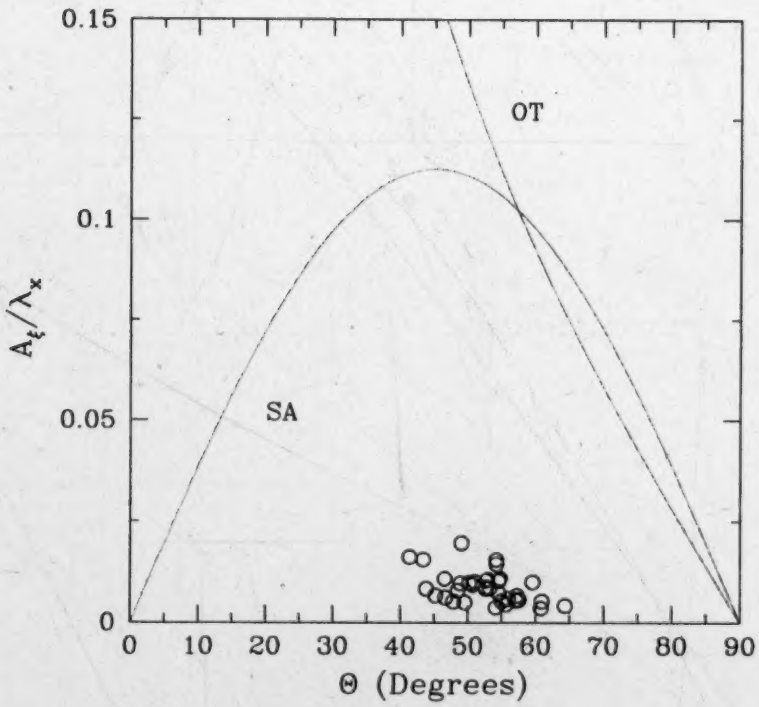

Figure 5.7: Internal gravity wave stability diagram. The curves labeled "SA" and "OT" denote the critical amplitudes at which self-accelerating and overturning instabilities are anticipated, respectively.

5.4 Internal Gravity Waves - Momentum Flux

Based on observations of intrusion speeds, we have found that the internal gravity waves extract a negligible quantity of the intrusion's energy. Here, we provide a quantitative estimate of the impact of wave generation on v_i, the intrusion's speed of propagation. Specifically, the change in v_i due to the extraction of momentum by the internal gravity waves is given by

$$\langle \Delta v_i \rangle \simeq \langle u'w' \rangle \frac{T}{L}, \tag{5.10}$$

where T and L represent characteristic time and length scales for the wavepacket duration and vertical extent of the generation region, respectively. In a typical experiment, three to four distinct internal gravity wave peaks are obsérved at any instant in time, thus we set $T = 4(2\pi/\omega)$, the time scale over which four wave crests are formed. Furthermore, because wave excitation is primarily due to the forcing imparted by the intrusion head, we set $L = h_i$. Combining equations (5.5) and (5.10), we find an average value for $|\langle \Delta v_i \rangle|/v_*$ of only 0.047 ± 0.039. Therefore, in a typical experiment, the effect of the internal gravity waves is to decrease the intrusion velocity by less than 5%.

As described in Chapter 5.1, this result shows notable discrepancies with the analysis of de Rooij [20] who studied symmetric saline intrusions that propagate within uniformly stratified surroundings. In a representative experiment, de Rooij [20] estimated that internal gravity wave excitation reduces v_i by approximately 71%.

In the present study, the intrusion's depth of penetration into the stratified layer is initially zero and remains small throughout the duration of the experiment. By contrast, the experimental set-up employed by de Rooij [20] was such that the intrusion's plane of propagation coincided with the level of mid-depth. Strong columnar modes (standing internal gravity waves of infinite horizontal wavelength and zero frequency) were therefore established once the lock was released. Compared with the present study in which these features were typically not observed, a higher fraction of energy was therefore

transfered from the intrusion to the internal gravity wave field. Because columnar modes are due to the flow of stratified fluid within a confined geometry wherein boundary reflections are significant, we feel that our study provides a more accurate representation of geophysical flows in which the domain size is effectively infinite. The explicit application of our results to such large-scale flows is discussed in the following chapter.

Chapter 6

Application of the Experimental Results to Geophysical Flows

6.1 Fluid Intrusions in the Atmosphere

This study is motivated in part by a desire to assess the ability of thunderstorm outflows that propagate along the tropopause (hereafter referred to as interfacial outflows) to excite internal gravity waves in the stratosphere. In the present set of experiments, the intrusion's plane of propagation lies above the stratified layer. The Boussinesq approximation suggests, however, that dynamically equivalent results would be obtained if, as in the atmosphere, the stratified layer were forced from below (Spiegel & Veronis [85]). Furthermore, although stratospheric internal gravity waves are characterised by anelastic amplitude growth, such effects can be neglected when considering wave excitation over a vertical distance that is small with respect to the local scale height.

Although the experiments described in Chapter 3 are therefore applicable to the atmospheric flow condition shown in Figure 1.1, it must be emphasized that the density profile of the real atmosphere is far more complicated than that depicted in Figure 3.2. Specifically, there does not exist an abrupt density step between the troposphere and stratosphere (see *e.g.* Figure 1(b) of Birner,

Dörnbrack & Schumann [8]) and the definition of σ_* is therefore ambiguous in an atmospheric context. Furthermore, because of the complexity of convective storm systems, the tops of which often overshoot their level of neutral buoyancy, interfacial outflows rarely have the appearance of a simple fluid intrusion. The precise definitions of l_i and h_i are therefore also ambiguous in many circumstances. Consequently, the results described below are intended only to provide crude estimates of the wave momentum flux associated with interfacial outflows. Further study is therefore required to confirm this analysis.

The characteristic period, T, of waves generated by interfacial outflows can be estimated by combining the results of Table 5.1 with the dispersion relation for internal gravity waves (see Appendix E). Explicitly, taking $N = 0.02\,\mathrm{s}^{-1}$ as a characteristic value for the stratification of the stratosphere (Birner, Dörnbrack & Schumann [8]), it can be shown that $T \simeq 9$ minutes. Although the internal gravity waves are therefore relatively high-frequency waves (see *e.g.* Dewan *et al.* [22]), it has been noted by Alexander & Pfister [2] that "high-frequency [internal gravity] waves carry a disproportionate share of the [internal] gravity wave momentum flux" and therefore play an especially important role in atmospheric circulation. To estimate the vertical flux of horizontal momentum associated with wave generation by interfacial outflows, we seek an equation that relates $\rho_{00}\,\langle u'w'\rangle$ to those properties of the intrusion that are directly measurable: v_i, h_i and l_i. Explicitly, for $-1/2 \leq \zeta_* \leq 0.25$, the collapse of the data shown in Figure 6.1 suggests that:

$$\frac{\rho_{00}\,\langle u'w'\rangle}{(Nl_i)^2} = 10^{-3.7\pm0.3}\rho_{00}\left(\frac{v_i}{\sqrt{\sigma_* g h_i}}\right)^{2.9\pm0.6}, \tag{6.1}$$

where $\rho_{00} = 1000\,\mathrm{kg/m^3}$ is a standard reference density for water. We assume that $l_i = 500\,\mathrm{m}$, a representative scale for the head of an interfacial outflow (*e.g.* as visualised by a high-level rope cloud). For the range of velocities corresponding to $-1/2 \leq \zeta_* \leq 0.25$ (see Figure 5.2), equation (6.1) predicts average values for $\rho_{00}\,\langle u'w'\rangle$ of between $0.2\,\mathrm{N/m^2}$ and $3\,\mathrm{N/m^2}$ depending on the values chosen for the empirical constants. By contrast, for topographically generated waves, average values for $\rho_{00}\,\langle u'w'\rangle$ typically range between $0.1\,\mathrm{N/m^2}$

and $1.0\,\mathrm{N/m^2}$ (see Table 1 of Palmer, Shutts & Swinbank [67]).

The fact that the wave momentum flux associated with interfacial outflows is comparable to that due to topographic forcing is somewhat surprising. Whereas flow over mountains provides a spatially broad and near-continuous source of internal gravity waves, however, large-scale convective events occur sporadically, particularly in the extra-tropics. Furthermore, not all convective storms are of sufficient height to reach the tropopause. Because the stratification of the troposphere is relatively weak, outflows that travel below the tropopause are likely less effective at exciting internal gravity waves in the stratosphere. Taken together, these results suggest that in comparison with topographic forcing, wave excitation by interfacial outflows results globally in a smaller total vertical flux of horizontal momentum in the stratosphere. Locally, however, these may constitute an important source of stratospheric internal gravity waves over the tropical oceans.

6.2 Fluid Intrusions in the Ocean

Equation (6.1) can also be applied to storm-induced fluid intrusions that propagate along or just below the level of the thermocline. Before proceeding, however, let us recall the limitations of the present study in that, as with the atmosphere, the ocean's vertical density gradient does not have the simple appearance of the profile shown in Figure 3.1. More importantly, fluid intrusions of this type have not been observed directly. Although their existence appears likely based on observations and simulations of storm-induced vertical mixing in the ocean (see Chapter 1), further observational data are required to confirm their existence and efficacy as sources of internal gravity waves.

For the atmospheric case considered previously, our results are easily generalized because multiple observational data are available. Here, we focus on one particular geophysical event: the passage of Hurricane Norbert over the eastern north Pacific Ocean during September and October of 1984. Figure 10(c) of Price, Sanford & Forristall [70] shows the anticipated sea surface

cooling and concurrent mixed layer deepening due to the storm-induced vertical mixing associated with this particular hurricane. Results are based on a numerical model initialized with actual storm conditions as measured using a series of AXCP sensors located between approximately 16^o and 22^o N and 106^o and 112^o W. Specifically, Price, Sanford & Forristall's [70] analysis predicts a deepening of the surface mixed layer from $z \simeq 50\,\mathrm{m}$ to $z \simeq 90\,\mathrm{m}$ and a corresponding mixed layer density increase of approximately $0.64\,\mathrm{kg/m^3}$.

Relative to the unperturbed ambient (the vertical density gradient of which is depicted in Figure F.1 of Appendix F), we speculate that this mixed parcel of fluid will ultimately collapse and propagate as a fluid intrusion just below the interface separating the uniform mixed layer from the deeper (and strongly stratified) ocean. Applying the first order asymptotic approximations to HH80's equations given by equations (2.22) and (2.23), we show in Appendix F that the predicted horizontal and vertical extents of the intrusion head are $h_i = 35.1\,\mathrm{m}$ and $l_i = 167\,\mathrm{m}$, respectively. Applying equation (6.1), characteristic values for $\rho_{00}\langle u'w'\rangle$ of between $0.2\,\mathrm{N/m^2}$ and $2\,\mathrm{N/m^2}$ are therefore predicted.

By comparison, for internal waves excited by either the "obstacle effect" or a Kelvin-Helmholtz instability, Lien, McPhaden & Gregg [48] found characteristic values for $\rho_{00}\langle uw\rangle$ of approximately $0.3\,\mathrm{N/m^2}$. Furthermore, during the 1984 Tropic Heat experiment, Wijesekera & Dillon [98] estimated that for narrow-band internal waves, $\rho_{00}\langle uw\rangle = 0.1\,\mathrm{N/m^2}$ to $0.6\,\mathrm{N/m^2}$. In both cases, the surface stress imparted by the wind was notably smaller than the Reynolds stress.

The above results suggest that the local influence of internal gravity waves excited by fluid intrusions is roughly comparable to those generated by other near-surface mechanisms. Consistent with the discussion of the previous section, however, the global significance of these waves is estimated to be small due to the intermittent nature of strong (*i.e.* hurricane-scale) storms. In particular, to generate a fluid intrusion of the type described above, storms must be of sufficient strength to result in substantial vertical mixing in the ocean

and/or a notable deepening of the surface mixed layer. By comparison, internal gravity wave generation by flow over rough bathymetry or turbulent forcing is expected on a near-continuous basis. Nonetheless, storm-induced fluid intrusions may represent an important local source of internal gravity waves over and above the contribution of the large-scale inertial flows that are more typically associated with the ocean's response to hurricane-scale storms.

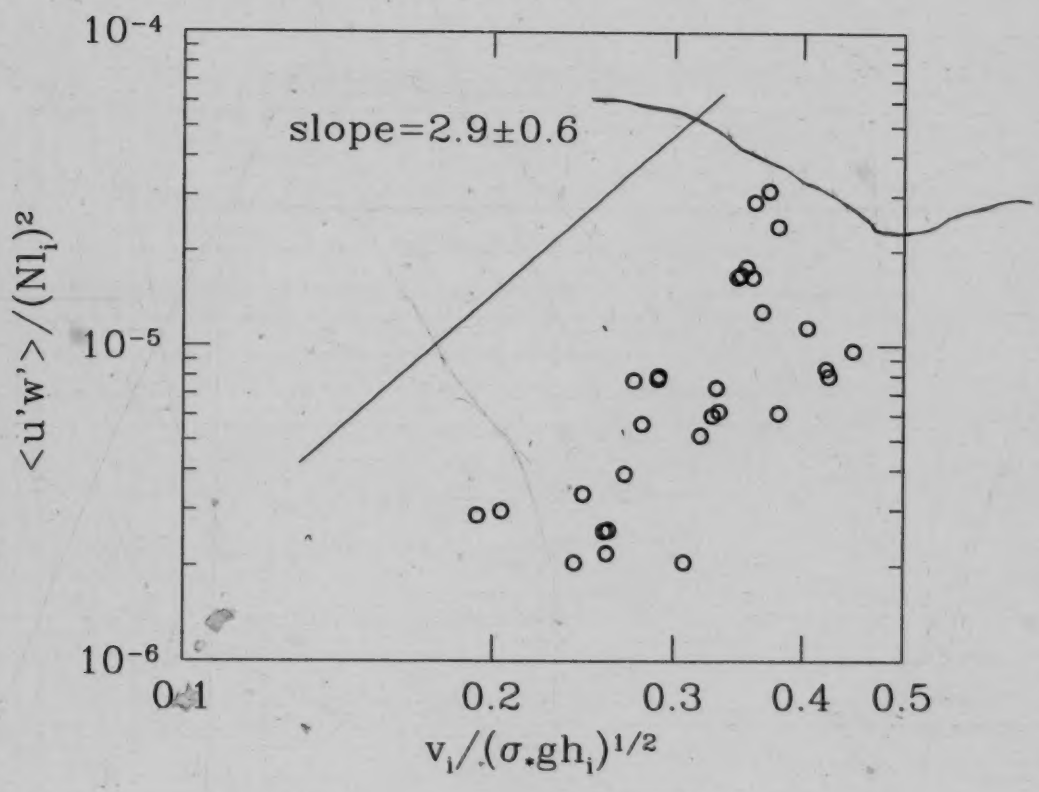

Figure 6.1: Log-log plot of the normalized momentum flux as a function of the normalized intrusion velocity for $-1/2 \leq \zeta_* \leq 0.25$. The slope of the (vertically offset) best-fit line is indicated.

Chapter 7

Discussion and Conclusions

Experiments have been performed in which a fluid intrusion is released along the interface between a uniform fluid (above) and a uniformly stratified fluid (below) using a simple lock release apparatus. Because no return flow of stratified fluid is established by releasing the lock fluid, the generation of internal gravity waves in the stratified fluid is due solely to bulk deflections caused by the fluid intrusion. Unlike the related studies of Amen & Maxworthy [3] and Maxworthy *et al.* [57] wherein currents propagate within a fully stratified ambient, the intrusion's speed of propagation is essentially constant. No rhythmic interaction is established between the intrusion and the internal gravity waves.

As indicated by Figures 5.1 and 5.2, the theory of HH80 provides estimates accurate to within 50% or better for h_+, h_- and v_i when $-1/2 \leq \zeta_* \lesssim 0.25$. Thereafter, the intrusion's depth of penetration into the stratified layer becomes strongly dependent on N^2 and the dynamics controlling the intrusion's behaviour become more complex than those considered in HH80's model.

The normalized wave amplitude, A_ξ/λ_x, is positively correlated with ζ_* for $-1/2 \leq \zeta_* \lesssim 0.25$. In all cases, $A_\xi/\lambda_x < 0.02$ and the internal gravity waves extract only a small fraction of the intrusion's momentum. Their horizontal wavelength, λ_x, is proportional to l_i whereas ω is such that the angle of wave propagation is approximately $53^o \pm 11^o$. Internal gravity wave propagation in this range was also observed by Sutherland & Linden [94] and Dohan &

Sutherland [23] who considered wave excitation by a turbulent shear flow and stationary turbulence, respectively.

Although this thesis is primarily a study in experimental fluid dynamics, we have discussed some rudimentary applications of these results to flows in the atmosphere and ocean. In particular, we have examined circumstances in which internal gravity waves are generated by the horizontal propagation of a mixed region that results from large-scale storms. Table 7.1 presents a summary of the predicted wave momentum fluxes due to wave excitation by two particular geophysical flows.

A comparison between our results for the atmosphere and those summarized in Table 1 of Palmer, Shutts & Swinbank [67] suggests that the momentum flux associated with wave generation by interfacial outflows is comparable to that due to flow over rough topography. Moreover, the momentum flux that results from storm-induced fluid intrusions in the ocean may be comparable to that of waves excited by either the "obstacle effect" or a local Kelvin-Helmholtz instability (Wijesekera & Dillon [98], Lien, McPhaden & Gregg [48]). Because of the sporadic nature of the large-scale storms that give rise to fluid intrusions of the types described in Table 7.1, however, the global impact of these flows as sources of internal gravity waves is estimated to be small in comparison with flow over rough topography/bathymetry. Nonetheless, in tropical settings they may represent an important local source of atmospheric and oceanic internal gravity waves.

Table 7.1: Wave momentum fluxes associated with internal gravity wave generation from fluid intrusions in the atmosphere and ocean.

Geophysical Flow	$\rho_{00} \langle u'w' \rangle$ (N/m^2)
Interfacial outflows (atmosphere)	0.2 to 3
Storm-induced fluid intrusions (ocean)	0.2 to 2

Appendix A

Benjamin's Analysis of Gravity Currents

A.1 Deep Gravity Currents

Figure A.1 shows the propagation of a bottom-propagating gravity current of density ρ_{gc} beneath a uniform ambient of density ρ_+ and height H. We assume that the flow profile is symmetric such that variations in the y-direction (into the page) can be neglected. We further neglect the effects of viscosity, mixing and surface tension. The gravity current can therefore be considered as energy-conserving. Shallow gravity currents, wherein the effects of mixing are not necessarily negligible are considered in the following section. Finally, it is assumed that the gravity current is in the slumping stage of its motion, *i.e.* its total height, h, and speed of propagation, v_{gc}, are constant. As described in Chapter 2, this assumption is valid until the gravity current has travelled a distance of approximately 10 lock-lengths, at which point the flow becomes self-similar and begins to decelerate. Because the current's motion is steady, we may choose a frame of reference in which the gravity current is stationary with respect to a moving ambient. At the point A (see Figure A.1), far upstream of the stagnation point O, the ambient travels at a speed v_{gc} whereas far downstream of the stagnation point (point B, say), it flows at speed v'.

Without loss of generality, we assume that the stagnation point denotes a point of zero pressure. As such, the pressure is also zero along the bottom interface of the gravity current. Upstream and downstream of the point O, the pressure varies hydrostatically with z. To simplify the subsequent analysis, we define a reduced pressure, $\tilde{p}$, such that it includes hydrostatic effects. Explicitly,

$$\tilde{p} = p + \rho_+ g z.$$

The pressure upstream and downstream of the stagnation point are therefore given by

$$p_U = p_A,$$

and

$$p_D = \begin{cases} -\rho_+ g' z & 0 \leq z \leq h \\ -\rho_+ g' h & z > h \end{cases},$$

respectively, where g' is the reduced gravity defined as $g' = g(\rho_{gc} - \rho_+)/\rho_+$ and, for notational convenience, we have dropped the tildes.

The gravity current's motion must satisfy conservation of mass, energy and momentum. We therefore require that

$$H v_{gc} = (H - h) v', \tag{A.1}$$

$$-\rho_+ g' h + \frac{1}{2}\rho_+ (v')^2 = 0, \tag{A.2}$$

and

$$\frac{H \rho_+ v_{gc}^2}{2} = (H - h)\rho_+ [(v')^2 - g' h] - \frac{\rho_+ g' h^2}{2}. \tag{A.3}$$

Equation (A.2) is derived by applying Bernoulli's equation along a curve immediately above the upper interface of the gravity current between points O and B. Bernoulli's equation is applicable in the present case since the current does not dissipate energy (see *e.g.* §4.15 of Kundu [44]).

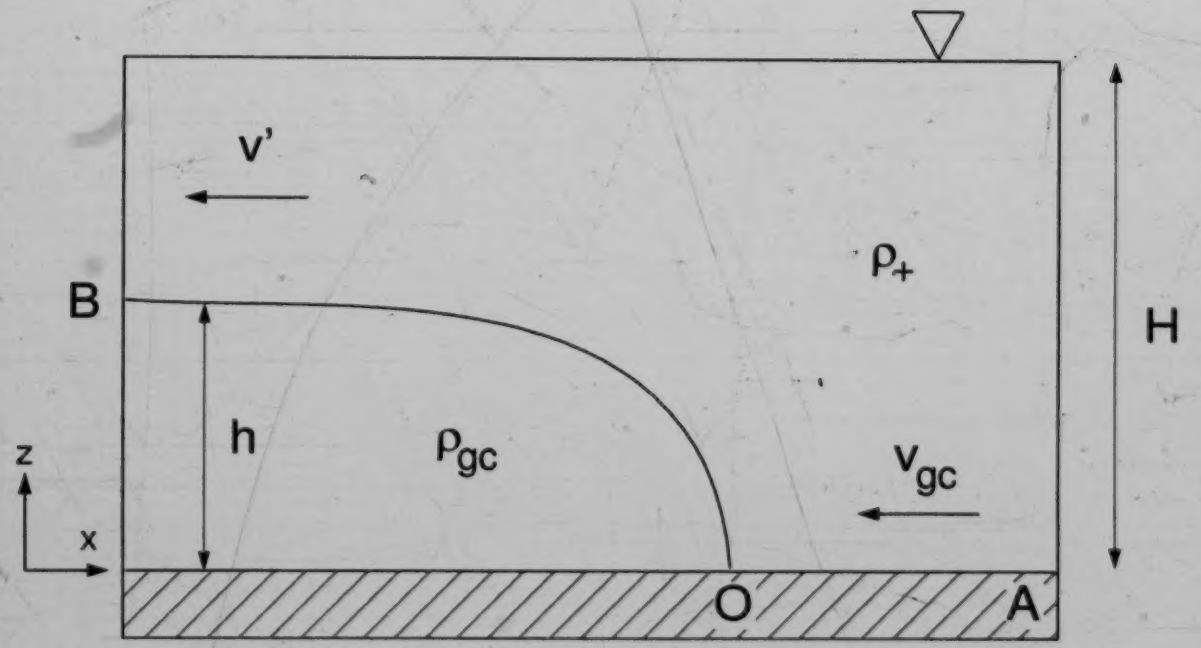

Figure A.1: The propation of a deep, energy-conserving gravity current through a uniform ambient of depth H. The $x - z$ coordinate system is as indicated.

Equations (A.1), (A.2) and (A.3) represent three equations in three unknowns, v_{gc}, v' and h. Combining equations (A.1) and (A.3), it can be shown that

$$(v')^2 = \frac{g'Hh(2H-h)}{H^2-h^2}. \tag{A.4}$$

Substituting this result into equation (A.2) yields a quadratic equation in h the solutions of which are $h = 0$ and $h = H/2$. Applying the non-trivial solution to equation (A.4), we find

$$v' = \sqrt{2}\sqrt{g'h},$$

from which it follows that

$$v_{gc} = \frac{1}{\sqrt{2}}\sqrt{g'h}. \tag{A.5}$$

A.2 Shallow Gravity Currents

When $h > H/2$, Benjamin [6] demonstrated that the gravity current is energetically unstable in that it cannot sustain itself in the absence of some external forcing. By contrast, flows for which $h < H/2$ can be maintained without energy input and are frequently observed in natural or industrial settings. In this case, however, the gravity current must either dissipate energy through mixing (Benjamin [6]) or extract energy and momentum from the backward-propagating disturbance that is generated by releasing the lock (Shin, Dalziel & Linden [78]). This transfer is affected by wave propagation along the interface.

Consider for example Figure A.2 which shows a dissipative gravity current of density ρ_{gc} propagating into infinitely deep surroundings of density ρ_+. As before, the current's motion is assumed steady such that we may choose a frame of reference in which the gravity current is stationary. Far upstream of the stagnation point O (at point A, say), the ambient has a velocity v_{gc} whereas far downstream (at points B and C, say), its velocity is v'. Far from the bottom boundary, however, the velocity is assumed to be independent of

both x and z. As such, the pressure difference between points A and C can be determined through hydrostatic balance

$$p_C - p_A = \rho_+ g' d, \tag{A.6}$$

where g' is defined as before and d is the height of the current sufficiently far behind the head. Consistent with our analysis of energy-conserving flows, we choose $p_O = 0$. Hence $p_C = 0$ and thus,

$$p_A = -\rho_+ g' d. \tag{A.7}$$

An alternate expression for p_A can be derived by applying Bernoulli's equation between points A and O. (Although Bernoulli's equation does not apply to dissipative gravity currents, it can be employed at points upstream of such flows.) Explicitly, we find

$$p_A = -\frac{\rho_+ v_{gc}^2}{2}. \tag{A.8}$$

Combining equations (A.7) and (A.8) it can be shown that

$$v_{gc} = \sqrt{2}\sqrt{g' d}. \tag{A.9}$$

As described above, Shin, Dalziel & Linden [78] consider the more realistic circumstance in which communication between the forward and backward-propagating disturbances is permitted through interfacial wave propagation. Although a detailed consideration of their arguments is beyond the scope of the present study, they find (see their equations (3.17), (3.21) and (8.1))

$$v_{gc} = \sqrt{g' d}, \tag{A.10}$$

i.e. Fr = 1 not Fr = $\sqrt{2}$ as predicted from Benjamin's analysis. For details, see also Shin [77].

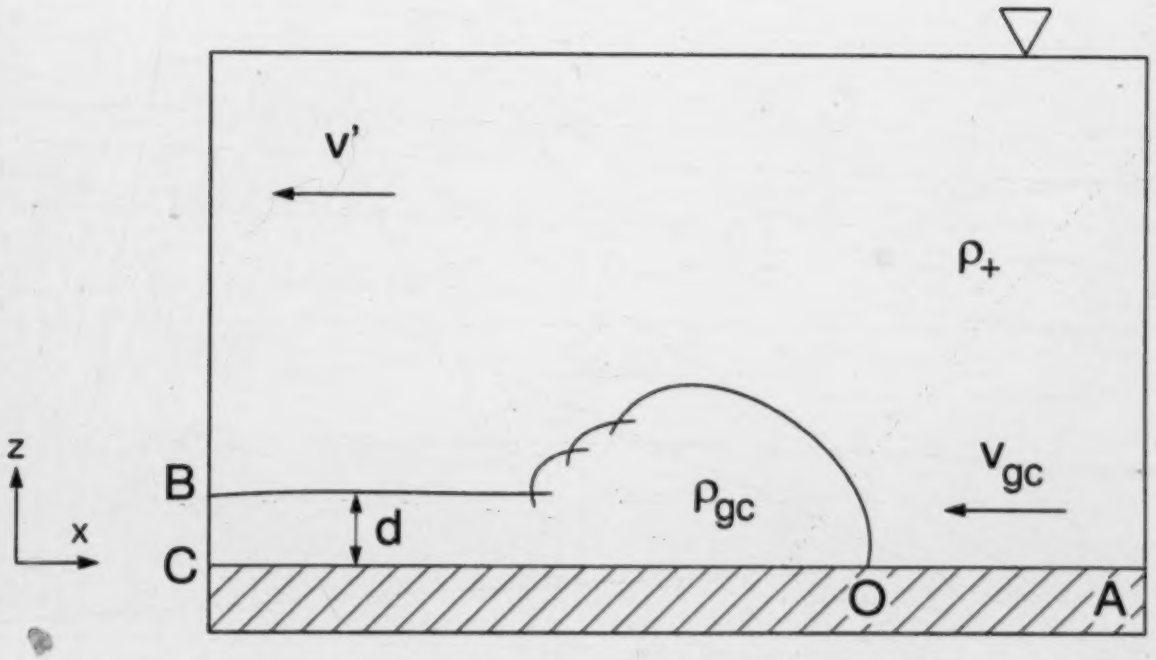

Figure A.2: The propagation of a dissipative gravity current through a uniform ambient of infinite depth. The $x - z$ coordinate system is as indicated.

Appendix B

Asymptotic Approximation

Equations (2.20) and (2.21) represent, respectively, expressions for mass and momentum conservation in terms of the non-dimensional parameters X and Y.[1] Writing X and Y as perturbation expansions in $\Gamma = \zeta + 1/2$ (*i.e.* $X = \Gamma X_1 + \mathcal{O}(\Gamma^2)$ and $Y = \Gamma Y_1 + \mathcal{O}(\Gamma^2)$), equations (2.20) and (2.21) reduce to

$$0 = \Gamma(H_+ - 8H_- X_1) + \mathcal{O}(\Gamma^2), \tag{B.1}$$

and

$$0 = \Gamma^2(H_+^2 Y_1 + 2H_-^2 X_1^2) + \mathcal{O}(\Gamma^3), \tag{B.2}$$

respectively. We therefore require that

$$X_1 = \frac{H_+}{8H_-}, \qquad Y_1 = -\frac{1}{32},$$

and hence, to first order,

$$r_- = 1 - \left(\frac{H_+}{8H_-}\right)\Gamma, \tag{B.3}$$

and

$$r_+ = \frac{1}{2} - \frac{\Gamma}{32}. \tag{B.4}$$

Equations (2.22) and (2.23) follow directly from the above results.

[1] These expressions assume implicitly that the fluid intrusion is energy-conserving.

Applying equations (B.3) and (B.4) to equations (2.16) and (2.17), it can be shown that

$$\frac{v_i}{\sqrt{\sigma g h_i}} = 2\sqrt{2}\sqrt{\frac{\Gamma}{16+5\Gamma}}\left(1-\frac{\Gamma}{16}\right)\sqrt{1+\frac{\Gamma}{16}}. \tag{B.5}$$

The above expression can be simplified by using the Binomial Theorem to give

$$\sqrt{1+\frac{\Gamma}{16}} = 1+\frac{\Gamma}{32}+\mathcal{O}(\Gamma^2), \tag{B.6}$$

and

$$\sqrt{\frac{1}{16+5\Gamma}} = \frac{1}{4}\left(1-\frac{5}{32}\Gamma+\mathcal{O}(\Gamma^2)\right). \tag{B.7}$$

Combining equations (B.5), (B.6) and (B.7) yields equations (2.24) and (2.25).

Appendix C

Experimental Parameters

Experimentally determined values for N^2, σ_* and σ_i are presented in Tables C.1 and C.2. Entries denoted by † indicate runs for which $\tilde{\rho} = \rho_i$. In all other cases, $\tilde{\rho} = \rho_*$.

Table C.1: Experimental parameters (weak stratification).

N^2 (s^{-2})	σ_s	σ_i
0.37	0.0026	0.0007
		0.0014
		0.0021
0.67	0.0054	0.0009
		0.0016
		0.0023
0.69	0.0045	0.0006
		0.0012
		0.0019
0.67	0.0038	0.0006
		0.0012
		0.0019
0.67	0.0026	0.0006
		0.0012
		0.0019
0.69	0.0024	0.0006
		0.0012
		0.0019
0.66	0.0015	0.0006
		0.0012
		0.0019 †

Table C.2: Experimental parameters (strong stratification).

N^2 (s^{-2})	σ_s	σ_i
0.92	0.0027	0.0005
		0.0011
		0.0018
1.15	0.0102	0.0006
		0.0013
		0.0020
1.14	0.0089	0.0006
		0.0012
		0.0019
1.21	0.0059	0.0006
		0.0012
		0.0019
1.17	0.0037	0.0006
		0.0013
		0.0020
1.19	0.0007	0.0006
		0.0011 †
		0.0018 †

Appendix D

Fluid Intrusions in a Uniformly Stratified Ambient

This appendix considers the derivation of equation (4.1) which relates v_i, the speed of propagation of a symmetric fluid intrusion traveling in a uniformly stratified ambient, to v_{LW}, the speed of the linear, mode-one long wave. Consider for example Figure D.1, which shows a fluid intrusion of fixed depth h_i and density ρ_i propagating into a stratified ambient of depth H_s. As discussed in Maxworthy *et al.* [57], the internal gravity waves that are excited by the intrusion can propagate no faster than v_{LW} the value of which depends on the background stratification and the total height of the ambient layer. Explicitly,

$$v_{LW} = \frac{NH_s}{\pi}. \tag{D.1}$$

By contrast, Benjamin's [6] analysis (see Appendix A) suggests that v_i ought to depend on h_i and $\Delta\rho$, where $\Delta\rho$ is the magnitude of the density jump across the top and bottom interfaces of the intrusion. More specifically,

$$v_i = \mathrm{Fr}\sqrt{\left(\frac{\Delta\rho}{\rho_{00}}\right) g h_i}, \tag{D.2}$$

where ρ_{00} is a standard reference density and Fr is a non-dimensional Froude number. Consistent with the one-layer case considered by Benjamin [6] (see *e.g.* equation (3.15) of de Rooij [20]), we assume that Fr=Fr(h_i/H_s).

As shown in Figure D.1, however, $\Delta\rho$ is also half of the total jump in the background density gradient across a vertical distance h_i

$$\Delta\rho = -\frac{1}{2}\left(\frac{d\bar{\rho}}{dz}\right) h_i, \tag{D.3}$$

and therefore,

$$v_i = \frac{\mathrm{Fr}}{\sqrt{2}}(Nh_i) < \frac{\mathrm{Fr}}{\sqrt{2}}(NH_s). \tag{D.4}$$

Equations (D.1) and (D.4) therefore imply that

$$\frac{v_i}{v_{LW}} < \frac{\mathrm{Fr}\cdot\pi}{\sqrt{2}}.$$

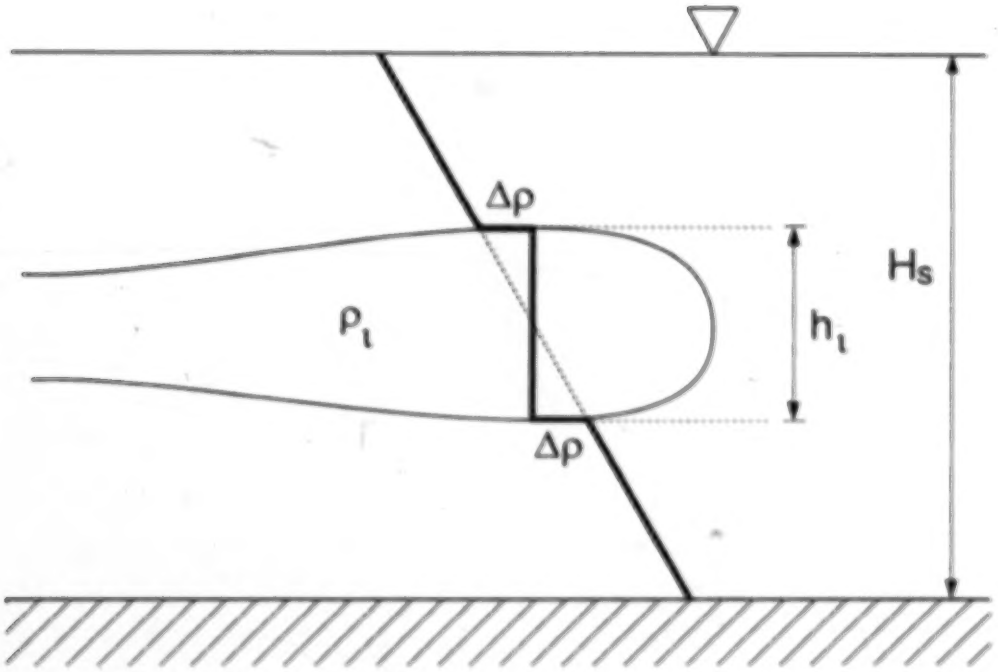

Figure D.1: The propagation of a symmetric fluid intrusion in stratified surroundings. The density profile is indicated by the thick solid line.

Appendix E

Dispersion Relation for Internal Gravity Waves

E.1 Problem Formulation

Wave motion in continuously stratified media is governed by the dispersion relation for internal gravity waves the derivation of which we consider in the present appendix. It is assumed that the domain in which fluid motion occurs is unbounded and that viscous and Coriolis forces can be neglected.

Under the Boussinesq approximation by which density variations are neglected except in the buoyancy term, the dynamics of the fluid are described by the following set of equations representing mass conservation, incompressibility and momentum conservation, respectively,

$$\nabla \cdot \mathbf{u} = 0, \tag{E.1}$$

$$\frac{D\rho}{Dt} = 0, \tag{E.2}$$

$$\frac{Du}{Dt} = -\frac{1}{\rho_{00}}\frac{\partial p}{\partial x}, \tag{E.3}$$

$$\frac{Dv}{Dt} = -\frac{1}{\rho_{00}}\frac{\partial p}{\partial y}, \tag{E.4}$$

$$\frac{Dw}{Dt} = -\frac{1}{\rho_{00}}\frac{\partial p}{\partial z} - \frac{\rho g}{\rho_{00}}, \tag{E.5}$$

where $\mathbf{u} = (u, v, w)$ and ρ_{00} represents a standard reference density. Consistent with the analysis of Kundu [44] (see also Lighthill [49] and de Rooij [20]), we assume the existence of a background mean state in which there is no fluid motion and the background density and pressure fields are hydrostatically balanced *i.e.* $d\bar{p}/dz = -\bar{\rho}g$. Our interest is in the dynamic response of the system to small perturbations. We therefore write

$$\rho(x, y, z, t) = \bar{\rho}(z) + \rho'(x, y, z, t),$$

and,

$$p(x, y, z, t) = \bar{p}(z) + p'(x, y, z, t),$$

in which ρ' and p' represent perturbation terms. We assume that the response of the fluid to small perturbations is two-dimensional *i.e.* $v = 0$ and $\mathbf{u} = (u, 0, w)$ where u and w denote small perturbations to the stationary mean state. Substituting these results into equations (E.1) through (E.5) yields

$$\frac{\partial u}{\partial x} + \frac{\partial w}{\partial z} = 0 \tag{E.6}$$

$$\frac{\partial \rho'}{\partial t} - \left(\frac{\rho_{00} N^2}{g}\right) w = 0; \tag{E.7}$$

$$\frac{\partial u}{\partial t} = -\frac{1}{\rho_{00}} \frac{\partial p'}{\partial x}, \tag{E.8}$$

$$\frac{\partial w}{\partial t} = -\frac{1}{\rho_{00}} \frac{\partial p'}{\partial z} - \frac{\rho' g}{\rho_{00}}, \tag{E.9}$$

where in all cases, higher order (non-linear) terms have been neglected. In equation (E.7), we introduced the square of the buoyancy frequency defined as

$$N^2 = -\frac{g}{\rho_{00}} \frac{\partial \bar{\rho}}{\partial z}.$$

E.2 Wave Solution

We now consider the solution to equations (E.6) to (E.9). In particular, note that equation (E.6) is satisfied exactly by introducing a streamfunction, ψ,

such that

$$u = -\frac{\partial \psi}{\partial z}, \qquad w = \frac{\partial \psi}{\partial x}. \tag{E.10}$$

Taking the difference between the z-derivative of equation (E.8) and the x-derivative of equation (E.9) and applying equation (E.10) yields

$$-\frac{\partial}{\partial t}\left(\frac{\partial^2 \psi}{\partial x^2} + \frac{\partial^2 \psi}{\partial z^2}\right) = \frac{g}{\rho_{00}}\frac{\partial \rho'}{\partial x}. \tag{E.11}$$

Moreover taking the time derivative of the above equation and combining it with a suitable multiple of the x-derivative of equation (E.7), it can be shown that

$$\frac{\partial^2}{\partial t^2}\left(\frac{\partial^2 \psi}{\partial x^2} + \frac{\partial^2 \psi}{\partial z^2}\right) + N^2\frac{\partial^2 \psi}{\partial x^2} = 0. \tag{E.12}$$

We assume a two-dimensional wave solution to equation (E.12) of the form

$$\psi(x, z, t) = \hat{\psi}\exp[\imath(k_x x + k_z z - \omega t)] + \text{c.c.},$$

where $\hat{\psi}$ is the perturbation amplitude, k_x and k_z represent the horizontal and vertical wavenumbers, respectively, and c.c. represents the complex conjugate. Substituting this result into equation (E.12), we find

$$\omega^2(k_x^2 + k_z^2)\hat{\psi} - N^2 k_x^2 \hat{\psi} = 0. \tag{E.13}$$

Therefore, non-trivial solutions to equation (E.12) must satisfy the following relation

$$\frac{\omega^2}{N^2} = \frac{k_x^2}{k_x^2 + k_z^2}. \tag{E.14}$$

Finally, defining

$$\Theta = \cos^{-1}\left(\frac{k_x}{\sqrt{k_x^2 + k_z^2}}\right)$$

it follows that

$$\omega = N\cos\Theta. \tag{E.15}$$

Physically, Θ represents the angle that lines of constant phase make with respect to the vertical. Equation (E.15) represents the dispersion relation for two-dimensional internal gravity waves in a continuously stratified, unbounded medium. It implies that for internal gravity waves, $0 \leq \omega \leq N$.

E.3 Group and Phase Velocities

Equation (E.15) has several important consequences. For example, let us consider the relation between the group and phase velocities, defined respectively as

$$\mathbf{c_g} = \left(\frac{\partial \omega}{\partial k_x}, \frac{\partial \omega}{\partial k_z} \right),$$

and

$$\mathbf{c_p} = \frac{\omega}{k} \cdot \frac{\mathbf{k}}{k},$$

where $k = \sqrt{k_x^2 + k_z^2}$. Explicitly, applying equation (E.14), it can be shown that

$$\mathbf{c_g} = \frac{N k_z}{k^3}(k_x, -k_z), \tag{E.16}$$

and

$$\mathbf{c_p} = \frac{\omega}{k^2}(k_x, k_z). \tag{E.17}$$

Hence,

$$\mathbf{c_g} \cdot \mathbf{c_p} = 0. \tag{E.18}$$

In contrast to surface waves for which $\mathbf{c_g}$ is aligned with $\mathbf{c_p}$, internal gravity waves propagate such that the group and phase velocities are perpendicular to one another. Practically speaking, equation (E.18) implies that the direction in which energy is transported is perpendicular to the direction in which lines of constant phase propagate. For this reason, internal gravity waves are also sometimes referred to as "shear waves."

Appendix F

Wave Momentum Flux of Storm-Induced Oceanic Internal Gravity Waves

F.1 Application of Holyer & Huppert's Analysis

Equation (6.1) relates the wave momentum flux to the physical dimensions of the wave source *i.e.* the head of the fluid intrusion. In particular, to predict $\rho_{00} \langle u'w' \rangle$, some estimate of the intrusion's horizontal extent, l_i, is required. For the atmospheric circumstance considered in Chapter 6.1, the characteristic value for l_i is based on the observed scale of a high-level rope cloud. Unfortunately, this approach cannot be employed when considering storm-induced fluid intrusions in the ocean. To the author's knowledge, no direct observations of these flows exist. Hence, for the geophysical flow considered in Chapter 6.2, we estimate l_i from h_i which is itself based on the results of HH80's analysis.

Consider for example Figure 10(c) of Price, Sanford & Forristall [70] which shows the eastern north Pacific Ocean's vertical temperature profile immediately prior to the arrival of Hurricane Norbert. As described in Chapter 6.2,

temperature values are based on numerical simulations initialized using data determined by direct observation of the storm. Without any significant loss of accuracy, we consider this ambient temperature gradient to be well represented by the piecewise linear profile depicted in Figure F.1.

During the storm, a deepening of the mixed layer from an initial depth of $z \simeq 50\,\mathrm{m}$ to a final depth of $z \simeq 90\,\mathrm{m}$ is predicted by Price, Sanford & Forristall's [70] numerical model. The change in density of the mixed layer can therefore be predicted using Figure F.1 and the thermal expansion coefficient of water, $\alpha = -0.32\,\mathrm{kg/m^3/^\circ C}$.[1] Explicitly,

$$\rho_i = \frac{\rho_1 z_1 + \int_{z_1}^{z_2} \rho(z) dz}{z_2},$$

and thus

$$\rho_i = \frac{\rho(27.5\,^\circ\mathrm{C}, s) z_1 + \rho(23\,^\circ\mathrm{C}, s)(z_2 - z_1)}{z_2},$$

where ρ_1 and ρ_i are, respectively, the densities of the mixed layer before and after vertical mixing and $z_1 \simeq 50\,\mathrm{m}$ and $z_2 \simeq 90\,\mathrm{m}$ are defined as in Figure F.1. The AXCP sensors employed by Price, Sanford & Forristall [70] were not able to measure salinity, s. For simplicity, we therefore choose a density scale such that $\rho(27.5\,^\circ\mathrm{C}, s) = 0\,\mathrm{kg/m^3}$. Hence

$$\rho_i = \left(\frac{90\,\mathrm{m} - 50\,\mathrm{m}}{90\,\mathrm{m}}\right)(-0.32\,\mathrm{kg/m^3/^\circ C})(23\,^\circ\mathrm{C} - 27.5\,^\circ\mathrm{C}) = 0.64\,\mathrm{kg/m^3}.$$

Assuming this parcel of locally mixed fluid collapses within the broader ambient and forms a horizontally propagating fluid intrusion, we anticipate the intrusion's level of neutral buoyancy to be $z_{NB} = 58.4\,\mathrm{m}$. The plane of propagation is therefore directly below the level $z = 50\,\mathrm{m}$, which denotes the bottom of the uniform mixed region (see Figure F.1).

[1] Price, Sanford & Forristall [70] neglect density variations due to salinity changes.

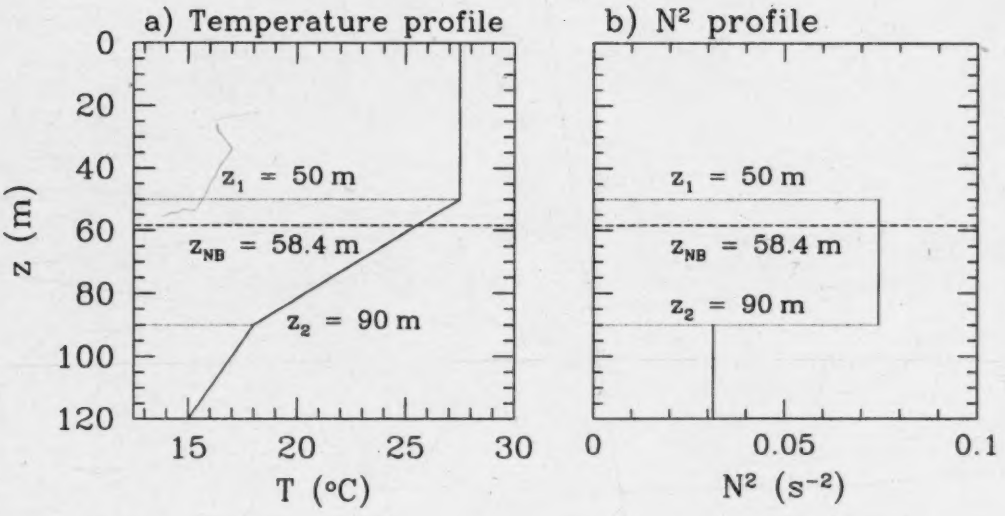

Figure F.1: (a) Temperature and (b) N^2 profiles of the eastern north Pacific Ocean prior to the mixing induced by Hurriance Norbert. (Adapted from Figure 10(c) of Price, Sanford & Forristall [70].) The long dashed line indicates the intrusion's level of neutral buoyancy.

In addition to ρ_i, we also require some estimate of $\rho_* - \rho_+$, the precise definition of which is ambiguous in an oceanographic context. The analysis of Appendix D indicates, however, that the propagation of a fluid intrusion through stratified surroundings results in abrupt "step" changes in the density profile (see *e.g.* Figure D.1). For the purposes of applying the results of Chapter 5 to the present analysis, we therefore define ρ_* such that

$$\beta h_i \left(-\frac{d\bar{\rho}}{dz} \right) = \rho_* - \rho_+, \tag{F.1}$$

where $\rho_+ = \rho_1 = 0\,\mathrm{kg/m^3}$, $-d\bar{\rho}/dz = 0.076\,\mathrm{kg/m^4}$ is the density gradient between $z = 50\,\mathrm{m}$ and $z = 90\,\mathrm{m}$ and h_i is the total height of the intrusion head. Furthermore, β is defined such that

$$\beta = \min \left[\frac{(z_{NB} - z_1) + h_-}{h_+ + h_-},\ 1 \right], \tag{F.2}$$

where h_- and h_+ represent the depths of penetration of the intrusion head above and below z_{NB}, respectively. This parameter accounts for the fact that the intrusion may be of sufficient height that the level of the top of the intrusion head lies above $z = 50\,\mathrm{m}$. Although the definition of $\rho_* - \rho_+$ given by equations (F.1) and (F.2) differs somewhat from the definition provided in Chapter 3.1, the results of the present study and the numerical simulations of Sutherland, Flynn & Dohan [91] indicate that h_i is only weakly dependent on the magnitude of the density step for a broad range of density parameters.

To solve equations (F.1) and (F.2), we desire an explicit formula that relates h_i and ρ_*. Such a relation is provided by the first-order asymptotic approximations to HH80's equations as derived in Chapter 2.4. Explicitly, combining equations (2.22) and (2.23), it can be shown that

$$\frac{h_i}{H_+} = \frac{1}{2} + \frac{5}{32} \left(\frac{\rho_i - \rho_+}{\rho_* - \rho_+} \right), \tag{F.3}$$

where, in the present context, $H_+ = z_{NB} = 58.4\,\mathrm{m}$. Solving equations (F.1) through (F.3) using a simple iterative routine, we find a value for ρ_* of approximately $1.00\,\mathrm{kg/m^3}$. Hence, from equation (2.15), $\zeta = 0.143$ and $\Gamma =$

$\zeta + 1/2 = 0.643$. For this value of ζ, the full equations of HH80 are not particularly well represented by a first-order asymptotic approximation about the point $\zeta = -1/2$. It will be shown in the following section, however, that this approach can nonetheless provide estimates for $\rho_{00} \langle u'w' \rangle$ that are accurate to within an order of magnitude.

Applying the above results to equations (2.22), (2.23), (2.24) and (2.25), the following estimates for the intrusion's total height and normalized velocity can be derived: $h_i = 35.1\,\mathrm{m}$ and $v_i/\sqrt{\sigma g h_i} = 0.499$. Furthermore, combining the results of Figures 5.1 and 5.4(a), it can be shown that for the experiments considered in the present study, $l_i \simeq 4.74 \cdot h_i$ on average. Therefore, in the context of the geophysical problem, $l_i \simeq 4.74 \cdot 35.1\,\mathrm{m} = 167\,\mathrm{m}$. Finally, applying equation (6.1), we estimate that the wave momentum flux associated with internal gravity waves generated by a storm-induced fluid intrusion is between $0.2\,\mathrm{N/m^2}$ and $2\,\mathrm{N/m^2}$ depending on the values chosen for the empirical constants.

F.2 Justification of the Momentum Flux Calculation

The analysis of the previous section employs a first-order asymptotic approximation to HH80's equations about $\zeta = -1/2$ when computing the magnitude of the density jump induced by the fluid intrusion (see equations (F.1) through (F.3)). In this particular case, however, ρ_+, ρ_i and ρ_* are such that $\zeta = 0.143$. Although this is beyond the range of ζ values for which there is strong agreement between the full equations of HH80 and the first order asymptotic approximations thereto, Figures 5.1 and 5.2 indicate that the asymptotic approximations nonetheless provide estimates for h_+, h_- and v_i that are within approximately 50% of the values determined directly from HH80's theory. An analysis of equation (6.1) shows that the resulting estimates for $\rho_{00} \langle u'w' \rangle$ are therefore order-of-magnitude accurate.

As a complement to this result, let us also consider the behaviour of equation (6.1) in the range wherein HH80's equations are well represented by the first-order asymptotic approximations about $\zeta = -1/2$. Combining equation (6.1) with the estimates for h_+, h_- and $v_i/\sqrt{\sigma g h_i}$ provided, respectively, by equations (2.22), (2.23) and (2.24) and recalling that $l_i \simeq 4.74 \cdot h_i$, it can be shown that

$$\rho_{00} \langle u'w' \rangle = 10^{-3.7 \pm 0.3} \rho_{00} (4.74 \cdot NH_+)^2 \left(\frac{1}{2} + \frac{5}{32}\Gamma \right)^2 \left(1 - \frac{3}{16}\Gamma \right)^\gamma \left(\frac{\Gamma}{2} \right)^{\gamma/2}, \tag{F.4}$$

where $\gamma = 2.9 \pm 0.6$. Hence, using the Binomial Theorem and defining

$$\chi := 10^{-3.7 \pm 0.3} \rho_{00} (4.74 \cdot NH_+)^2 \cdot 2^{-2-\gamma/2},$$

we find that

$$\rho_{00} \langle u'w' \rangle \simeq \chi \left(1 + \frac{5}{8}\Gamma \right) \left(1 - \frac{3\gamma}{16}\Gamma \right) \Gamma^{\gamma/2}. \tag{F.5}$$

To leading order therefore, $\rho_{00} \langle u'w' \rangle$ grows only as $\Gamma^{\gamma/2} \sim \Gamma^{3/2}$.

Bibliography

[1] ALEXANDER, M. J., HOLTON, J. R. & DURRAN, D. R. 1995 The gravity wave response above deep convection in a squall line simulation. *J. Atmos. Sci.* **52**, 2212–2226.

[2] ALEXANDER, M. J. & PFISTER, L. 1995 Gravity wave momentum flux in the lower stratosphere over convection. *Geophys. Res. Lett.* **22**, 2029–2032.

[3] AMEN, R. & MAXWORTHY, T. 1980 The gravitational collapse of a mixed region into a linearly stratified solution. *J. Fluid Mech.* **96**, 65–80.

[4] BARR, D. I. H. 1967 Densimetric exchange flow in rectangular channels III: Large scale experiments. *Houille-Blanche* **6**, 619–631.

[5] BECKER, E. & SCHMITZ, G. 2002 Energy deposition and turbulent dissipation owing to gravity waves in the mesosphere. *J. Atmos. Sci.* **59**, 54–68.

[6] BENJAMIN, T. B. 1968 Gravity currents and related phenomena. *J. Fluid Mech.* **31**, 209–248.

[7] BERES, J. H., ALEXANDER, M. J. & HOLTON, J. R. 2002 Effects of tropospheric wind shear on the spectrum of convectively generated gravity waves. *J. Atmos. Sci.* **59**, 1805–1824.

[8] BIRNER, T., DÖRNBRACK, A. & SCHUMANN, U. 2002 How sharp is the tropopause at midlatitudes? *Geophys. Res. Lett.* **29**, 10.1029/2002GL015,142.

[9] BRITTER, R. E. & SIMPSON, J. E. 1978 Experiments on the dynamics of a gravity current head. *J. Fluid Mech.* **88**, 223–240.

[10] BRITTER, R. E. & SIMPSON, J. E. 1981 A note on the structure of the head of an intrusive gravity current. *J. Fluid Mech.* **112**, 459–466.

[11] CLARK, T. L., HAUF, T. & KUETTNER, J. P. 1986 Convectively forced internal gravity waves: Results from two-dimensional numerical experiments. *Quart. J. R. Met. Soc.* **112**, 899–925.

[12] CORNILLON, P., STRAMMA, L. & PRICE, J. F. 1987 Satellite measurements of sea surface cooling during hurricane Gloria. *Nature* **326**, 373–375.

[13] D'ALESSIO, S. J. D., MOODIE, T. B., PASCAL, J. P. & SWATERS, G. E. 1996 Gravity currents produced by sudden release of a fixed volume of heavy fluid. *Stud. Appl. Math.* **96**, 359–385.

[14] D'ALESSIO, S. J. D., MOODIE, T. B., PASCAL, J. P. & SWATERS, G. E. 1997 Intrusive gravity currents. *Stud. Appl. Math.* **98**, 19–46.

[15] DALZIEL, S. B. 1992 Decay of rotating turbulence: Some particle tracking experiments. *Appl. Sci. Res.* **49**, 217–244.

[16] DALZIEL, S. B., HUGHES, G. O. & SUTHERLAND, B. R. 2000 Whole field density measurements. *Experiments in Fluids* **28**, 322–335.

[17] D'ASARO, E. A. 1995 Upper-ocean inertial currents forced by a strong storm. 2. Modeling. *J. Phys. Oceanogr.* **25**, 2937–2952.

[18] D'ASARO, E. A. 1995 Upper-ocean inertial currents forced by a strong storm. 3. Interaction of inertial currents and mesoscale eddies. *J. Phys. Oceanogr.* **25**, 2953–2958.

[19] D'Asaro, E. A., Eriksen, C. C. & Levine, M. D. 1995 Upper-ocean inertial currents forced by a strong storm. 1. Data and comparisons with linear theory. *J. Phys. Oceanogr.* **25**, 2909–2936.

[20] de Rooij, F. 1999 Sedimenting particle-laden flows in confined geometries. Ph.D. thesis, Univ. of Cambridge.

[21] de Rooij, F., Linden, P. F. & Dalziel, S. B. 1999 Saline and particle-driven interfacial intrusions. *J. Fluid Mech.* **389**, 303–334.

[22] Dewan, E. M., Piccard, R. H., O'Neil, R. R., Gardiner, H. A., Gibson, J., Mill, J. D., Richards, E., Kendra, M. & Gallery, W. O. 1998 MSX satellite observations of thunderstorm-generated gravity waves in mid-wave infrared images of the upper stratosphere. *Geophys. Res. Lett.* **25**, 939–942.

[23] Dohan, K. & Sutherland, B. R. 2002 Internal waves generated from a turbulent mixed region. *Phys. Fluids* in press.

[24] Dugan, J. P., Warn-Varnas, A. C., & Piacsek, S. A. 1976 Numerical results for laminar mixed region collapse in a density stratified fluid. *Comp. Fluids* **4**, 109–121.

[25] Faust, K. M. & Plate, E. J. 1984 Experimental investigation of intrusive gravity currents entering stably stratified fluids. *J. Hydraul. Res.* **22**, 315–325.

[26] Flynn, M. R., Onu, K., & Sutherland, B. R. 2002 Internal wave excitation by a vertically oscillating sphere. *J. Fluid Mech.* in press.

[27] Flynn, M. R. & Sutherland, B. R. 2003 Intrusive gravity currents and internal gravity wave generation in stratified fluid. *J. Fluid Mech.* submitted.

[28] FOVELL, R., DURRAN, D., & HOLTON, J. R. 1992 Numerical simulations of convectively generated stratospheric gravity waves. *J. Atmos. Sci.* **49**, 1427–1442.

[29] FRITTS, D. C. & NASTROM, G. D. 1992 Sources of mesoscale variability of gravity waves. Part II: Frontal, convective and jet stream excitation. *J. Atmos. Sci.* **49**, 111–127.

[30] GAVRILOV, N. M. & ROBLE, R. G. 1994 The effect of gravity-waves on the global mean temperature and composition structure of the upper-atmosphere. *J. Geophys. Res.* **99**, 25773–25780.

[31] GILL, A. E. 1982 *Atmosphere-Ocean Dynamics.* Academic Press, San Diego, USA.

[32] GRÖBELBAUER, H. P., FANNELØP, T. K., & BRITTER, R. E. 1993 The propagation of intrusion fronts of high density ratios. *J. Fluid Mech.* **250**, 669–687.

[33] HACKER, J. 1996 Gravity currents in rotating channels. Ph.D. thesis, Univ. of Cambridge.

[34] HALLWORTH, M. A., HUPPERT, H. E., PHILLIPS, J. C., & SPARKS, R. S. J. 1996 Entrainment into two-dimensional and axisymmetric turbulent gravity currents. *J. Fluid Mech.* **308**, 289–311.

[35] HÄRTEL, C., KLEISER, L., MICHAUD, M., & STEIN, C. F. 1997 A direct numerical simulation approach to the study of intrusion fronts. *J. Eng. Math.* **32**, 103–120.

[36] HOLYER, J. Y. & HUPPERT, H. E. 1980 Gravity currents entering a two-layer fluid. *J. Fluid Mech.* **100**, 739–767.

[37] HOULT, D. P. 1972 Oil spreading on the sea. *Ann. Rev. Fluid Mech.* **4**, 341–368.

[38] HUPPERT, H. E. 1982 The propagation of two-dimensional and axisymmetric viscous gravity currents over a rigid horizontal surface. *J. Fluid Mech.* **121**, 43–58.

[39] HUPPERT, H. E. 2002 Gravity currents and lava domes. *NERC DAMTP Geophysical and Environmental Fluid Dynamics Summer School - Notes.* Univ. of Cambridge.

[40] HUPPERT, H. E. & SIMPSON, J. E. 1980 The slumping of gravity currents. *J. Fluid Mech.* **99**, 785–799.

[41] KEULEGAN, G. H. 1957 An experimental study of the motion of saline water from locks into fresh water channels. Technical Report 5168 *Nat. Bur. Stand. Rept.*

[42] KIDA, H. A. 1984 A numerical experiment on the general circulation of the middle atmosphere with a three-dimensional model explicitly representing internal gravity waves and their breaking. *Pure Appl. Geophys.* **122**, 731–746.

[43] KLEMP, J. B., ROTUNNO, R. & SKAMAROCK, W. C. 1994 On the dynamics of gravity currents in a channel. *J. Fluid Mech.* **269**, 169–198.

[44] KUNDU, P. K. 1990 *Fluid Mechanics.* Academic Press, San Diego, USA.

[45] LARGE, W. G. & CRAWFORD, G. B. 1995 Observations and simulations of upper-ocean response to wind events during the ocean storms experiment. *J. Phys. Oceanogr.* **25**, 2831–2852.

[46] LEDWELL, J. R., MONTGOMERY, E., POLZIN, K., ST. LAURENT, L., SCHMIDT, R. & TOOLE, J. 2000 Evidence for enhanced mixing over rough topography in the abyssal ocean. *Nature* **403**, 179–182.

[47] LEVINE, M. D. & ZERVAKIS, V. 1995 Near-inertial wave-propagation into the pycnocline during ocean storms - Observations and model comparison. *J. Phys. Oceanogr.* **25**, 2890–2908.

[48] LIEN, R.-C., MCPHADEN, M. J. & GREGG, M. C. 1996 High-frequency internal waves at 0°, 140° W and their possible relationship to deep-cycle turbulence. *J. Phys. Oceanogr.* **26**, 581–600.

[49] LIGHTHILL, M. J. 1978 *Waves in Fluids.* Cambridge University Press, Cambridge, England.

[50] LINDEN, P. F. 1975 The deepening of a mixed layer in a stratified fluid. *J. Fluid Mech.* **71**, 385–405.

[51] LINDZEN, R. S. 1974 Stability of a Helmholtz velocity profile in a continuously stratified infinite Boussinesq fluid – Applications to clear air turbulence. *J. Atmos. Sci.* **31**, 1507–1514.

[52] LINDZEN, R. S. 1981 Turbulence and stress owing to gravity wave and tidal breakdown. *J. Geophys. Res.* **86**, 9707–9714.

[53] LONG, R. R. 1955 Some aspects of the flow of stratified fluids. III Continuous density gradients. *Tellus* **7**, 341–357.

[54] MANINS, P. C. 1976 Intrusion into a stratified fluid. *J. Fluid Mech.* **74**, 547–560.

[55] MARSHALL, D. 2002 Thermohaline circulation. *NERC DAMTP Geophysical and Environmental Fluid Dynamics Summer School - Notes.* Univ. of Cambridge.

[56] MASON, P. J. & SYKES, R. I. 1982 A two-dimensional numerical study of horizontal roll vortices in an inversion capped boundary layer. *Quart. J. R. Met. Soc.* **108**, 801–823.

[57] MAXWORTHY, T., LEILICH, J., SIMPSON, J., & MEIBURG, E. H. 2002 The propagation of a gravity current in a linearly stratified fluid. *J. Fluid Mech.* **453**, 371–394.

[58] MCINTYRE, M. E. 2002 Advection-diffusion. *NERC DAMTP Geophysical and Environmental Fluid Dynamics Summer School - Notes.* Univ. of Cambridge.

[59] MEHTA, A., SUTHERLAND, B. R., & KYBA, P. J. 2002 Interfacial gravity currents: Part II - Wave excitation. *Phys. Fluids* **14**, 3558–3569.

[60] MEI, C. C. 1969 Collapse of a homogeneous fluid in a stratified fluid. *Proc. of the 12th Int. Cong. Appl. Mech.* (ed. M. Hetenyi & W. G. Vincenti). Springer, New York, USA.

[61] MICHAELIAN, M. E., MAXWORTHY, T., & REDEKOPP, L. G. 2002 The coupling between turbulent, penetrative convection and internal waves. *Eur. J. Mech. B/Fluids* **21**, 1–28.

[62] MILES, J. W. 1961 On the stability of heterogeneous shear flows. *J. Fluid Mech.* **10**, 496–508.

[63] MOODIE, T. B. 2002 Gravity currents. *J. Comput. Appl. Math.* **144**, 49–83.

[64] NIILER, P. P. & PADUAN, J. D. 1995 Wind driven motions in the northeast Pacific as measured by Langrangian drifters. *J. Phys. Oceanogr.* **25**, 2819–2830.

[65] ONU, K., FLYNN, M. R., & SUTHERLAND, B. R. 2002 Schlieren measurement of axisymmetric internal wave amplitudes. *Experiments in Fluids* in press.

[66] OSTER, G. 1965 Density gradients. *Sci. Am.* **213**, 70.

[67] PALMER, T. N., SHUTTS, G. J. & SWINBANK, R. 1986 Alleviation of a symmetric westerly bias in general circulation and numerical weather prediction models through an orographic gravity drag parametrization. *Quart. J. R. Met. Soc.* **112**, 1001–1039.

[68] PLUMB, R. A. & MCEWAN, A. D. 1978 The instability of a forced standing wave in a viscous, stratified fluid: A laboratory analogue of the Quasi-Biennial Oscillation. *J. Atmos. Sci.* **35**, 1827–1839.

[69] POLZIN, K. L., TOOLE, J. M., LEDWELL, J. R. & SCHMIDT, R. W. 1997 Spatial variability of turbulent mixing in the abyssal ocean. *Science* **276**, 93–96.

[70] PRICE, J. F., SANFORD, T. B. & FORRISTALL, G. Z. 1994 Forced stage response to a moving hurricane. *J. Phys. Oceanogr.* **24**, 233–260.

[71] QI, H. B., DESZOEKE, R. A., PAULSON, C. A. & ERIKSEN, C. C. 1995 The structure of near-inertial waves during ocean storms. *J. Phys. Oceanogr.* **25**, 2853–2871.

[72] ROSE, W. I., BLUTH, G. J. S., SCHNEIDER, D. J., ERNST, G. G. J., RILEY, C. M., HENDERSON, L. J. & MCGIMSEY, R. G. 2001 Observations of volcanic clouds in their first few days of atmospheric residence: The 1992 eruptions of Crater Peak, Mount Spurr Volcano, Alaska. *J. Geol.* **109**, 677–694.

[73] ROTTMAN, J. W. & SIMPSON, J. E. 1983 Gravity currents produced by instantaneous releases of a heavy fluid in a rectangular channel. *J. Fluid Mech.* **135**, 95–110.

[74] SALBY, M. L. & GARCIA, R. R. 1987 Transient response to localized episodic heating in the tropics. Part I: Excitation and short-time near-field behavior. *J. Atmos. Sci.* **44**, 458–498.

[75] SCHOOLEY, A. H. 1967 Wake collapse in a stratified fluid. *Science* **157**, 421–423.

[76] SCHOOLEY, A. H. & HUGHES, B. A. 1972 An experimental and theoretical study of internal waves generated by the collapse of a two-dimensional mixed region in a density gradient. *J. Fluid Mech.* **51**, 159–175.

[77] SHIN, J. O. 2001 Colliding gravity currents. Ph.D. thesis, Univ. of Cambridge.

[78] SHIN, J. O., DALZIEL, S. B. & LINDEN, P. F. 2003 Gravity currents produced by lock exchange. *J. Fluid Mech.* in press.

[79] SIMPSON, J. E. 1969 A comparison between laboratory and atmospheric density currents. *Quart. J. R. Met. Soc.* **95**, 758–765.

[80] SIMPSON, J. E. 1972 Effects of the lower boundary on the head of a gravity current. *J. Fluid Mech.* **53**, 759–768.

[81] SIMPSON, J. E. 1982 Gravity currents in the laboratory, atmosphere, and ocean. *Ann. Rev. Fluid Mech.* **14**, 213–234.

[82] SIMPSON, J. E. 1997 *Gravity Currents in the Environment and the Laboratory*, 2nd Edn. Cambridge University Press, Cambridge, England.

[83] SIMPSON, J. E. & BRITTER, R. E. 1979 The dynamics of the head of a gravity current advancing over a horizontal surface. *J. Fluid Mech.* **94**, 477–495.

[84] SKYLLINGSTAD, E. D. & DENBO, D. W. 1994 The role of internal gravity waves in the equatorial current system. *J. Phys. Oceanogr.* **24**, 2093–2110.

[85] SPIEGEL, E. A. & VERONIS, G. 1960 On the Boussinesq approximation for a compressible fluid. *Astrophys. J.* **131**, 442–447.

[86] SUTHERLAND, B. R. 1996 The dynamic excitation of internal gravity waves in the equatorial oceans. *J. Phys. Oceanogr.* **26**, 3214–3235.

[87] SUTHERLAND, B. R. 2000 Finite-amplitude internal wavepacket dispersion and breaking. *J. Fluid Mech.* **429**, 343–380.

[88] SUTHERLAND, B. R. 2002 Interfacial gravity currents. I. Mixing and entrainment. *Phys. Fluids* **14**, 2244–2254.

[89] SUTHERLAND, B. R., CAULFIELD, C. P. & PELTIER, W. R. 1994 Internal wave generation and hydrodynamic instability. *J. Atmos. Sci.* **51**, 3261–3280.

[90] SUTHERLAND, B. R., DALZIEL, S. B., HUGHES, G. O. & LINDEN, P. F. 1999 Visualisation and measurement of internal waves by "synthetic schlieren". Part 1: Vertically oscillating cylinder. *J. Fluid Mech.* **390**, 93–126.

[91] SUTHERLAND, B. R., FLYNN, M. R. & DOHAN, K. 2003 Internal wave excitation from a collapsing mixed region. *Deep Sea Res. II* in preparation.

[92] SUTHERLAND, B. R., FLYNN, M. R. & ONU, K. 2003 Schlieren visualisation and measurement of axisymmetric disturbances. *Nonlin. Proc. Geophys.* **10**, 303–309.

[93] SUTHERLAND, B. R., KYBA, P. J. & FLYNN, M. R. 2003 Gravity currents and waves in a two-layer fluid. *J. Fluid Mech.* submitted.

[94] SUTHERLAND, B. R. & LINDEN, P. F. 1998 Internal wave generation by flow over a thin barrier. *J. Fluid Mech.* **377**, 223–252.

[95] TURNER, J. S. 1973 *Buoyancy Effects in Fluids.* Cambridge University Press, Cambridge, England.

[96] UNGARISH, M. & HUPPERT, H. E. 2002 On gravity currents propagating at the base of a stratified fluid. *J. Fluid Mech.* **458**, 283–301.

[97] WEAST, R. C. 1981 *Handbook of Chemistry and Physics*, 62nd Edn. C. R. C. Press, Boca Raton, USA.

[98] WIJESEKERA, H. W. & DILLON, T. M. 1991 Internal waves and mixing in the upper equatorial Pacific ocean. *J. Geophys. Res.* **96**, 7115–7126.

[99] WU, J. 1969 Mixed region collapse with internal wave generation in a density stratified medium. *J. Fluid Mech.* **35**, 531–544.

[100] ZERVAKIS, V. & LEVINE, M. D. 1995 Near-inertial energy propagation from the mixed layer - Theoretical considerations. *J. Phys. Oceanogr.* **25**, 2872–2889.